

Parallel Transmission in MRI: Electromagnetic Considerations and Advances in Signal Chain Hardware

Dissertation

zur Erlangung des akademischen Grades

**doctor rerum naturalium
(Dr. rer. nat.)**

genehmigt durch die Fakultät für Naturwissenschaften
der Otto-von-Guericke-Universität Magdeburg

von: Dipl.-Phys. André Kühne
geb. am 04.08.1981 in Greifswald

Gutachter: Prof. Dr. rer. nat. habil. Oliver Speck
Prof. Dr. rer. nat. habil. Harald Möller

eingereicht am: 10.06.2016
verteidigt am: 16.12.2016

Betreuer:

Dr. rer. nat. habil. Bernd Ittermann Physikalisch-Technische Bundesanstalt, Berlin
Prof. Dr. rer. nat. habil. Oliver Speck Otto-von-Guericke-Universität, Magdeburg

Contents

Kurzfassung	vii
Abstract	xi
Nomenclature	xiii
1 Introduction	1
1.1 State of the art and motivation	1
1.2 Aims and structure of this thesis	3
2 Principles of Magnetic Resonance Imaging	5
2.1 Bloch equations	5
2.2 Excitation, reception and reciprocity	6
2.3 k-space	7
2.4 Spatially selective excitation	8
2.5 Electromagnetics of MRI coils	9
2.5.1 Vector potential, magnetic induction and electric fields	10
2.5.2 Wave impedance	10
2.5.3 Tuning and Matching	12
2.5.4 Efficiency and Q-factor	13
2.5.5 High frequency effects	14
2.5.6 Coil arrays	16
2.5.7 Numerical techniques	20
2.6 Parallel transmission	22
2.6.1 B_1 -shimming	22
2.6.2 Time-interleaved Acquisition of Modes	23
2.6.3 Transmit SENSE	23
2.7 Signal synthetization	23
3 Design and application of a scalable multi-channel RF signal generator	25
3.1 Hardware design	25
3.1.1 Concept	25
3.1.2 Digital signal hardware	27
3.1.3 Digital/Analog conversion	29
3.1.4 Scanner interfacing and synchronization	33
3.1.5 Pulse and sequence programming	36
3.1.6 Assembled setup	37

3.2	Measurements	38
3.2.1	Pulse output fidelity	38
3.2.2	8-channel measurements	39
3.2.3	(Almost) 12-channel measurements	42
3.3	Discussion	44
3.4	Conclusion	45
4	The electromagnetic power balance of an RF transmit coil array	47
4.1	Introduction	48
4.2	Poynting's Theorem	50
4.3	Source power	50
4.4	Dissipative losses	51
4.5	Radiative losses	52
4.6	Power balance	53
4.7	Coupling effects	54
5	Numerical characterization of the 12-channel octahedral coil array	57
5.1	Coil Setup	59
5.1.1	Current sheet antennas	59
5.1.2	Array design	59
5.2	Coil Analysis Methodology	61
5.2.1	Electromagnetic simulations	61
5.2.2	Maximum B_1 and Receive SNR analysis	64
5.2.3	Parallel transmission	65
5.3	Results	67
5.3.1	Single element characterization	67
5.3.2	Decoupling mechanism analysis	70
5.3.3	Full array analysis	71
5.4	Discussion	86
5.5	Conclusion	89
6	Summary and Outlook	91
	Bibliography	95
	Acknowledgments	105
	Curriculum vitae	107
	List of own publications	109
	Selbständigkeitserklärung	113

Kurzfassung

Die Magnetresonanztomographie (MRT) basiert auf dem Kernspinresonanzeffekt und ist ein Verfahren zur diagnostischen Bildgebung im menschlichen Körper mit einer Vielzahl von möglichen Kontrastparametern. Dabei wird durch ein hohes statisches Magnetfeld, genannt B_0 , eine makroskopische Magnetisierung im menschlichen Körper erzeugt, welche durch zusätzliche Applikation hochfrequenter Magnetfelder, B_1 , manipuliert und aus ihrer Gleichgewichtsausrichtung ausgelenkt werden kann. Diese Felder sind orthogonal zu B_0 und werden durch dedizierte Hochfrequenzspulen erzeugt. Idealerweise sind sie homogen über den zu untersuchenden Körperbereich, damit beobachtete Kontrastvariationen auf die lokale Anatomie oder Pathologien, nicht aber auf das B_1 Feld zurückzuführen sind. Bei der Rückkehr der Magnetisierung in ihre Gleichgewichtsausrichtung induziert diese in externen Empfangsspulen wiederum ein Hochfrequenzsignal, aus dem örtlich aufgelöste Bilder des menschlichen Körpers errechnet werden können.

Eine Erhöhung der statischen Magnetfeldstärke führt zu einem Anstieg des erreichbaren Signal-zu-Rausch Verhältnisses, was für viele Anwendungen zu einer signifikanten Verbesserung der diagnostischen Bildqualität führt. Andererseits führt der Feldstärkenanstieg zu einer proportionalen Frequenzerhöhung bzw. Wellenlängenverkürzung der für die Messung erforderlichen Hochfrequenzmagnetfelder. Dies hat zur Folge, dass die B_1 Feldverteilungen durch dielektrische Interaktionen mit dem menschlichen Gewebe räumlich inhomogen werden, was eine ungewünschte räumliche Kontrastmodulation nach sich zieht. Um von den zu erwartenden Signal-zu-Rausch Verbesserungen hoher (≥ 3 T) und ultrahoher (≥ 7 T) B_0 -Feldstärken zu profitieren, müssen diese Inhomogenitäten kompensiert werden.

Das parallele Senden, also der Einsatz mehrerer interferierender Hochfrequenzquellen für die B_1 -Erzeugung, stellt einen vielversprechenden Ansatz zur Lösung dieses Problems dar. Seit der Einführung durch Zhu und Katscher im Jahr 2004 wurde eine Vielzahl von Techniken vorgestellt, die sich die zusätzlichen Freiheitsgrade mehrerer Sendespulen in einem Spulenarray zunutze machen. Eine Gemeinsamkeit dieser Ansätze ist, dass ihre Effektivität für die Kompensation der B_1 -Inhomogenitäten mit einer größeren Anzahl unabhängiger Sendekanäle zunimmt. Während in aktuellen Publikationen Hochfrequenzspulen mit bis zu 32 Sendekanälen vorgestellt wurden, besitzen die meisten kommerziell erhältlichen MRT Scanner im Forschungsbereich lediglich bis zu acht unabhängige Signalgeneratoren, mit denen die Mehrkanalspulen angesteuert werden können. Eine einfache Erweiterung dieser Kanäle ist dem

Anwender im Allgemeinen nicht möglich, da die benötigte Hardware einerseits sehr komplex und andererseits tief im System verwurzelt ist.

Die Entwicklung eines erweiterbaren mehrkanaligen Signalgenerators war daher ein zentraler Punkt dieser Arbeit. Basierend auf digitaler Signalerzeugung und anschließender Digital/Analog-Wandlung, wird unter Umgehung herkömmlicher analoger Modulation ein Hochfrequenzsignal mit den gewünschten Amplituden-, Phasen-, und Frequenzverläufen generiert. Das aufgebaute System weist zwölf unabhängige Kanäle auf, ist mit einfachen Mitteln auf noch höhere Kanalzahlen erweiterbar und mit wenig Platz- und Kostenbedarf realisierbar. Es weist eine hervorragende Frequenz- und Phasenstabilität auf und kann damit auch für anspruchsvolle Mehrkanalanwendungen eingesetzt werden. Da lediglich ein vom Tomographen generierter Referenztakt und ein Triggersignal benötigt wird, ist der Aufbau prinzipiell in jedem kommerziell erhältlichen Scanner möglich. Nach einer detaillierten Beschreibung des realisierten Aufbaus wird die Anwendung für Mehrkanalmessungen mit einer oktahedralen 12-Kanal Spule in einem 3T MRT demonstriert, was signifikant über die kommerziell erhältlichen Möglichkeiten hinausgeht. Damit ist das beschriebene System eine Basis für die Entwicklung fortschrittlicher, hochgradig paralleler Anregungssysteme, die für den erfolgreichen Einsatz moderner paralleler Sendetechniken notwendig sind.

Aufgrund der durch die Maxwell-Gleichungen bestimmten Kopplung von elektrischen und magnetischen Feldern erzeugen die Hochfrequenzspulen nicht nur magnetische, sondern auch elektrische Felder. Diese führen zu einer Energiedeposition in leitfähigen biologischen Geweben, aber auch in umliegenden verlustbehafteten Materialien wie dem Spulengehäuse. Hinzu kommen Verluste in den in der Spule verbauten Komponenten, wie z.B. Kapazitäten oder Induktivitäten. Schließlich können elektrische und magnetische Feldkomponenten gemeinsam zu einer Abstrahlung der zugeführten Energie führen. Die Energiedeposition im Patienten ist dabei unvermeidbar, da das erwünschte B_1 -Feld direkt mit den verantwortlichen elektrischen Feldern einhergeht. Alle weiteren Verluste sind idealerweise so gering wie möglich, denn sie führen zu einer zusätzlichen Verringerung des Stromes in der Spule für eine gegebene Eingangsleistung und beeinträchtigen damit die erreichbare B_1 -Feldstärke. Während die relativen Anteile dieser Verluste für Einkanalspulen lediglich eine Abhängigkeit von ihrer dielektrischen Beladung durch den Patienten aufweisen, zeigen mehrkanalige Hochfrequenzspulen ein wesentlich komplexeres Verhalten. Die Energiedeposition hängt dabei zusätzlich von den Spannungsamplituden- und phasen ab, mit denen die einzelnen Elemente gespeist werden. Dabei kann es zu Situationen kommen, in der eine spezifische Superposition der Einzelkanalfelder durch übermäßige Verluste beeinträchtigt wird, während andere Überlagerungen dieses Problem nicht aufweisen. Es ist im Interesse eines Hochfrequenzspulentechnikers, solche Szenarien vor der Konstruktion einer Spule zu erkennen, und durch geeignete Designmodifikationen zu kompensieren.

Der zweite zentrale Punkt dieser Arbeit lag daher auf der Herleitung eines theoretischen Gerüsts für eine Leistungsbilanzanalyse von Sendespulenarrays basierend auf elektromagnetischen Simulationsdaten. Das Poyntingtheorem für zeitharmoni-

sche Felder wurde dabei in eine Matrixgleichung überführt, die das Verhalten interagierender Sendespulen über quadratische Formen beschreibt. Jedem Verlustmechanismus wird dabei eine hermitesche Matrix zugewiesen, deren Eigenwerte und Eigenvektoren Informationen über das Verhalten der jeweiligen Verluste enthalten. So sind z.B. die maximal und minimal möglichen Verlustanteile durch den größten bzw. kleinsten Eigenwert der jeweiligen Matrix gegeben. Zusätzlich erlaubt die Matrixformulierung eine elegante Analyse der Zusammenhänge zwischen Spulenkopplungsverhalten und Verlusten und kann dabei Grenzen für maximal erreichbare Entkopplungen aufzeigen.

Um die Anwendung des Formalismus zu demonstrieren, wurde er im Rahmen einer numerischen Spulencharakterisierung auf elektromagnetische Simulationsdaten der zuvor experimentell verwendeten 12-Kanal-Spule angewandt. Es konnte gezeigt werden, dass der kapazitive Entkopplungsmechanismus zur Erzeugung parasitärer Stromschleifen zwischen den einzelnen Elementen führt, was zwar die Kompensation induktiver Interaktionen erlaubt, im Gegenzug aber signifikante resistive Kopplungen erzeugt. Damit sind Kopplungsverluste beim Betrieb der Spule dominierend, direkt gefolgt von Verlusten in den Tuning-Kondensatoren. Eine detaillierte eigenmoden-basierte Analyse erlaubt es, Regionen mit signifikant eingeschränkter Sendeeffizienz zu identifizieren. Verglichen über alle Schichtorientierungen zeigt die Spule konsistent eine bessere Sensitivität in der transversalen Ebene. Die Erweiterung der Bilanzanalyse auf den Empfangsfall wurde zur Erstellung von räumlich aufgelösten Signal-zu-Rausch und Rauschquellkarten verwendet, wodurch lokale Sensitivitätsminima direkt mit ihren Ursachen verknüpft werden. Die numerische Untersuchung zeigt damit einerseits auf, wie zukünftige Iterationen der Spule modifiziert werden sollten, um eine höhere Sensitivität zu erreichen und dient andererseits als umfassende Demonstration der Leistungsbilanzanalyse in numerischen Spulenevaluationen.

Abstract

Going to higher static magnetic fields in magnetic resonance imaging promises an increased signal-to-noise ratio. However, high and ultra-high field MRI suffer from a spatial inhomogeneity of the applied radiofrequency magnetic fields *in vivo*, which significantly impacts the achievable image quality. In order to translate the SNR increase into images of superior diagnostic quality, the inhomogeneities need to be mitigated. The use of multiple interfering high-frequency field sources, termed parallel transmission, constitutes a promising solution candidate to tackle these issues. The present thesis contributes to parallel transmission techniques on both theoretical and hardware levels.

Raising the number of independently controllable transmission channels increases the system's potential to compensate inhomogeneity related artifacts, yet commercially available hardware setups are still limited in the number of channels offered. Hence, a scalable multi-channel transmitter for 3T MRI was developed. Featuring a small footprint and low cost, the setup was applied to phantom imaging experiments in conjunction with a twelve channel octahedral coil array, thus going beyond the capabilities of typical vendor-supplied systems. The design sets a foundation for parallel transmission applications requiring even higher channel numbers.

A profound understanding of a coil arrays' electromagnetic behavior is crucial for designing well-performing coils. Particularly, a detailed breakdown of the power balance can give insight into components that most severely impact coil performance. Therefore, a theoretical framework for the multi-channel power balance of coil arrays was derived from Poynting's theorem. Based on electromagnetic simulations, the resulting matrix formalism allows a straightforward analysis of worst-case and excitation-mode-specific losses, and can be additionally applied to generate noise source maps for reception fidelity analysis, and validate the physical plausibility of the simulation data. It thus serves as an important tool for MRI coil array development, assisting in the conception and construction of better-performing coils.

The loss analysis was then applied to the twelve-channel coil array. It was found, that the employed capacitive decoupling mechanism compensates inductive interaction, but results in additional resistive interaction, thus introducing strong losses due to coupling. Eigenmode analysis for transmission performance and noise source maps for reception consistently identified regions of lower coil performance, correlating them with strong capacitive losses. Overall, the array's loss analysis serves as an exemplary application of the previous theoretical considerations, and can be seen as a benchmark implementation of the methods for future coil analyses.

Nomenclature

CSA	Current Sheet Antenna
DAC	Digital/Analog converter
ESR	equivalent series resistance
FDTD	finite-difference time-domain
FIR	finite impulse response
FLASH	fast low-angle shot
GPU	graphics processing unit
LO	Local Oscillator
MPCU	measurement process control unit
MRI	magnetic resonance imaging
NMR	nuclear magnetic resonance
PLL	Phase-locked loop
PML	Perfectly Matched Layer
pTx	parallel transmission
RF	radio frequency
SAR	specific absorption rate
SAR	specific absorption rate
SENSE	sensitivity encoding
SNR	signal-to-noise ratio
SPI	Serial Peripheral Interface
TTL	Transistor–transistor logic

1 Introduction

1.1 State of the art and motivation

Magnetic resonance imaging (MRI) is a versatile technique with a wide range of clinical and pre-clinical applications. At the most basic level, it involves a concerted and synchronized application of magnetic fields spanning multiple orders of magnitude in amplitude and frequency in order to manipulate nuclear magnetizations and acquire spatially resolved images of the human body with a multitude of contrast parameters. A strong static magnetic field, B_0 , is responsible for creating a macroscopic magnetization originating from nuclear magnetic moments. Using an additional radio frequency (RF) magnetic field, B_1 , generated by dedicated resonating structures referred to as “coils” or “probes”, the magnetization can be perturbed from its equilibrium orientation parallel to B_0 . In turn, it induces an RF signal of identical frequency in the probe upon its following relaxation towards equilibrium, which is recorded and used to extract information about the subject under investigation. The frequency of B_1 is directly proportional to B_0 . Hence, the superposition of linearly varying field gradients on top of B_0 induces a spatial frequency variation that is used for generating the desired spatially resolved images [1].

Due to the inherently low magnitude of the induced magnetization, magnetic resonance techniques offer a relatively low intrinsic sensitivity, and measures to improve the signal-to-noise ratio (SNR) were highly sought after since their inception. Most prominently, an increase in the static magnetic field strength B_0 promises a corresponding increase in SNR [2–4], while at the same time raising the required frequency of the RF magnetic fields used for excitation. Due to anticipated RF penetration effects in human tissue, early publications predicted a maximum operation frequency of 10-20 MHz [2, 5], corresponding to a static magnetic field strength of 0.25-0.5 T, respectively. However, this expected limitation was soon overcome with the advent of imaging methods based on the Fourier transform of symmetric echos [6–8], starting a still ongoing race towards ever-increasing field strengths.

Naturally, the resulting increase in B_1 frequency brings along a coincident reduction in wavelength. The high relative permittivity of human tissue further reduces the RF wavelength *in vivo*, bringing it close to or even below the dimensions of the human body. This wavelength decrease, along with the mentioned penetration effects due to the electrical conductivity of human tissues, leads to various issues in high (≥ 3 T) and ultrahigh (≥ 7 T) field MRI. RF coils with current distributions resulting in homogeneous circularly polarized B_1 fields at low frequencies, such as Birdcage

resonators [9], will produce strongly inhomogeneous fields at high frequencies [10]. The inhomogeneities present themselves as central intensity enhancements and even regions of zero field. This hampers excitation as well as reception fidelity, modulates the perceived image contrast, and thus reduces the diagnostic image quality despite the overall increase in SNR. A fully homogeneous RF field over an extended volume at high frequencies, however, is not even achievable in theory according to Maxwell's equations, and achieving field uniformity over smaller subvolumes inside the sample would require correspondingly adapted current distributions on the coils [10]. Furthermore, power dissipation inside the patient due to ohmic heating originating from the RF fields increases, and tends to be focused deeper inside the body, raising additional safety concerns [10]. While the predicted SNR increase has certainly been observed and can even be exceeded [10, 11], it can only be leveraged in a clinical setting if the concomitant RF related issues are properly addressed and resolved.

Parallel transmission (pTx) techniques potentially constitute a promising solution to these problems [12, 13]. They are based on utilizing multiple independent coils in an array configuration to produce interfering RF fields, thus providing additional degrees of freedom to tackle inhomogeneity and power deposition concerns. Building on strong conceptual similarities with parallel reception approaches [14, 15], recent years have seen a surge in theoretical as well as practical research on pTx techniques for increased B_1 and signal homogeneity [16, 17], excitation of arbitrary magnetization patterns [18, 19] and improved management of power deposition (specific absorption rate, SAR) [20–22]. Simultaneously, hardware development has yielded improved coils for parallel transmission [23–29] as well as novel signal generators to individually drive the coil array elements [30, 31]. A current state-of-the-art transmit array system typically features eight transmission channels with dedicated coil arrays, along with a realtime supervision of globally and locally absorbed power to ensure patient safety [22, 32–35]. Despite these advancements, many challenges remain open in order to increase parallel transmission efficacy and bring it into clinical routine application, two of which shall be addressed in the present thesis.

It is well known, that the additional degrees of freedom provided by a larger number of independent transmission channels increase the achievable B_1 homogeneity [16, 36] and improve the performance of transmit SENSE related applications [19, 37] in terms of acceleration, excitation fidelity and power deposition [12]. However, while coils with more than eight transmission channels can be constructed in a relatively straightforward manner, their application is usually hindered by the limited number of RF transmit channels provided by the MRI scanner vendor. Extending the number of channels is a challenging task, as the generated signals for excitation have very stringent performance constraints in terms of temporal stability, and synchronicity with the other hardware components of the scanner.

The transmit coil arrays driven by the independent signal generators show a complex behavior with regards to the electromagnetic field distributions produced by them. While this forms the basis for the advanced excitation capabilities of the arrays, is also mirrored in the power deposition behavior, where different excitation

modes lead to vastly differing distributions of the input power between the various loss mechanisms, such as power deposited in the patient, the electrical components of the coil, radiation, or power reflection due to imperfect decoupling between elements. As unnecessarily high losses result in a substandard coil performance, a close understanding of the loss mechanisms and their interactions is crucial. While each of the loss contributions is well known, they have barely been studied in relation to one another. As an example, many developments solely focus on minimizing power reflection through improved decoupling structures, while at the same neglecting the impact these design modifications have on the overall power balance and coil efficiency.

1.2 Aims and structure of this thesis

The objectives of this thesis were to address two challenges: Firstly, to increase the number of available transmission channels on a commercially available MRI scanner, and secondly to derive a framework for loss analysis in transmit coil arrays.

This first challenge is addressed by describing the construction and application of an extensible pulse generator for parallel transmission MRI at 3T. The setup is shown to generate RF pulses with the required fidelity and synchronicity, which is further proven by multiple successful pTx experiments. The results of this work were presented at multiple international conferences [38–40], and a journal manuscript is in preparation. Since the motivation for the construction of the signal generator was to go beyond eight channels, the measurements were performed using a previously presented twelve-channel array with an octahedral geometry [41]. This coil array also serves as the connecting link between the theoretical and experimental parts of the present work.

The second aim of this thesis was to develop a framework for power balance calculation in RF transmit coil arrays. Theoretical expressions for the power balance are derived and a power loss analysis based on electromagnetic simulations is conducted on the twelve-channel array in order to better understand its behavior. These theoretical considerations were published [42, 43], along with their application to cylindrical RF coil arrays, as these geometries are in wide use and thus of broader interest to the community.

Following the introduction of necessary principles of MRI and corresponding parts of electromagnetic theory in chapter two, chapter three describes the conception, construction and application of an extensible arbitrary waveform generator for MRI parallel transmission. The hardware design approach is detailed, and challenges arising from the integration with the MR scanner are analyzed and some solutions presented. Parallel transmission experiments including static B_1 shimming as well as spatially selective transmit SENSE using an eight-channel commercially available coil array as well as the 12-channel octahedral coil array are shown, demonstrating the viability of the presented setup.

Chapter four will detail the derivation of matrix expressions for the power balance of an RF transmit coil array, based on Poynting's theorem. A special focus is set on separating different loss mechanisms; the interplay between losses and coil coupling is discussed and some, often overlooked, implications are highlighted. Chapter five then applies these theoretical considerations to a numerical analysis of the twelve channel coil array for 3T. First, a complete description and analysis of the coil array using common approaches and methods is done. The novel power balance formalism is then used to analyze a multitude of transmission modes and excitation schemes, highlighting performance bottlenecks and potential solutions. Furthermore, the methodology is applied to the receive case, where it is used to determine the most dominant noise sources.

Finally, the results and conclusions are summarized in chapter six, and an outlook to further applications and advancements of the presented methods is given.

2 Principles of Magnetic Resonance Imaging

The phenomenon of nuclear magnetic resonance (NMR) in condensed matter was independently described by Bloch and Purcell in 1946 [44, 45]. A comprehensive quantum mechanical derivation of NMR exceeds the scope of this thesis, and as many commonly presented portrayals and simplifications are misrepresenting the underlying physics [46–49], an approach based on classical physics is taken. A more in-depth treatment can be found in many excellent books on the matter, such as Abragam [50] or Slichter [51] for a quantum mechanical NMR derivation, Brown et al. [52] for a broader treatment of MRI concepts, and Chen & Hoult for engineering aspects [53].

2.1 Bloch equations

Phenomenologically, MRI is concerned with a manipulation of bulk nuclear magnetic moment (“magnetization”) distributions inside biological samples. The magnetization arises from the alignment of the proton (^1H) magnetic moments inside an external magnetic field. Indicating vector quantities by using boldface, this field is called \mathbf{B}_0 , which is usually defined to be oriented along the z axis. The dynamic response of a magnetization \mathbf{M} to time-dependent external magnetic fields is modeled by the Bloch equations, given in vector components as

$$\begin{aligned}\frac{dM_x}{dt} &= \gamma (\mathbf{M} \times \mathbf{B})_x - \frac{M_x}{T_2} \\ \frac{dM_y}{dt} &= \gamma (\mathbf{M} \times \mathbf{B})_y - \frac{M_y}{T_2} \\ \frac{dM_z}{dt} &= \gamma (\mathbf{M} \times \mathbf{B})_z + \frac{M_0 - M_z}{T_1}.\end{aligned}\tag{2.1}$$

Here, γ is the gyromagnetic ratio, which is a constant for the nucleus under investigation. For protons, it is given as $\gamma/2\pi = 42.58 \text{ MHz/T}$. In thermal equilibrium with $\mathbf{M} \parallel \mathbf{B}_0$, the system exhibits no dynamic behavior. However, the system can be perturbed by magnetic fields orthogonal to \mathbf{B}_0 , termed \mathbf{B}_1 , that are oscillating at or

close to the so-called Larmor frequency $f_L = \gamma/2\pi |\mathbf{B}_0|$. Following this perturbation, the magnetization also exhibits components in the transversal (xy) plane, which are themselves oscillating at the Larmor frequency. The amplitude of the transversal oscillations decays with a time constant T_2 , called the spin-spin relaxation time. Concurrently, M_z returns to the equilibrium magnetization M_0 with the spin-lattice relaxation time constant T_1 . Both time constants can strongly vary between different tissue types, or healthy and pathological tissue.

Many phenomena can be described in a simpler fashion when the Bloch equations are recast in a coordinate system rotating about \mathbf{B}_0 with the Larmor frequency. In this rotating frame, they can be written [50] as

$$\begin{aligned}\frac{dM_x}{dt} &= -\frac{M_x}{T_2} + \Delta\omega M_y \\ \frac{dM_y}{dt} &= -\Delta\omega M_x - \frac{M_y}{T_2} - \omega_1(t) M_z \\ \frac{dM_z}{dt} &= \omega_1(t) M_y - \frac{M_z - M_0}{T_1}.\end{aligned}\tag{2.2}$$

Here, $\Delta\omega = \gamma\Delta B_0$ represents an off-resonance term due to local variations in the \mathbf{B}_0 field, and $\omega_1(t) = \gamma\mathbf{B}_1(t)$ is the time dependent waveform of the \mathbf{B}_1 field. Furthermore, owing to their oscillatory behavior, the xy components of the magnetization can be compounded into a complex phasor-like quantity M_\perp defined as

$$M_\perp = M_x + iM_y\tag{2.3}$$

with the imaginary unit $i = \sqrt{-1}$. Directly following the application of a \mathbf{B}_1 field, the total magnetization is found to be stationary in this frame, being oriented at an angle α to the z axis. This angle is termed the flip angle of the previously applied pulse. For low flip angle, the Bloch equations can be linearized, which significantly simplifies many investigations [54]. In this regime, the M_z component is assumed to be approximately equal to its equilibrium value $M_z \approx M_0 = \text{const.}$

2.2 Excitation, reception and reciprocity

Having gained an overview on the magnetization's interaction with external external fields, the question of signal detection can be addressed. The oscillating transversal magnetization components following a pulsed \mathbf{B}_1 field create a voltage in a nearby conducting loop via Faraday induction [47], which can be detected. An understanding of the relation between the induced voltage versus the relative positioning of loop and magnetization is given by the principle of reciprocity [4, 55].

Suppose the loop were driven by a sinusoidal unit current at the Larmor frequency, thus producing a magnetic induction field \mathbf{B}_1 in its vicinity. The voltage ξ induced during reception is now related to this *hypothetical* field

$$\xi = - \int_{\text{sample}} \frac{\partial}{\partial t} (\mathbf{B}_1(\mathbf{r}) \cdot \mathbf{M}(\mathbf{r})) dV_s. \quad (2.4)$$

Two factors determine the contribution of a magnetization at position \mathbf{r} to the received signal: the local magnetic field strength \mathbf{B}_1 and the local magnetization \mathbf{M} .

A closer inspection of the principle of reciprocity in the rotating frame reveals, that only two different polarization components of \mathbf{B}_1 are responsible for excitation and reception. Starting from a complex phasor representation of the harmonic \mathbf{B}_1 field in cartesian coordinates, it can be split into two circularly polarized components defined as,

$$B_1^+ = \frac{B_{1,x} + iB_{1,y}}{2} \quad (2.5)$$

and

$$B_1^- = \frac{(B_{1,x} - iB_{1,y})^*}{2}. \quad (2.6)$$

During excitation, only the B_1^+ component can act on the magnetization, whereas the received signal is proportional to the local strength of B_1^- [55]. In free space, the \mathbf{B}_1 field produced by a simple loop will be linearly polarized, leading to B_1^+ and B_1^- being of equal magnitude. This equality breaks down *in vivo* with increasing Larmor frequency due to eddy currents induced by \mathbf{B}_1 inside a conducting sample, resulting in an elliptical polarization. Hence, the distinction between B_1^+ and B_1^- is very important, especially for a high static magnetic field strength. The electromagnetics of MRI coils will be further discussed in section 2.5.

2.3 k-space

As indicated by the name, magnetic resonance imaging is concerned with generating spatially resolved images. In principle, this is achieved by inducing a spatial variation of the Larmor frequency by superimposing linear gradient fields \mathbf{G} on top of \mathbf{B}_0 . While a large number of spatial localization schemes exist, most of them can be expressed within the so-called k-space formalism. Suppose a transversal magnetization throughout the sample has been created by the application of a B_1^+ field

just before $t = 0$. Switching on a spatial gradient field \mathbf{G} will induce a phase offset $\phi(\mathbf{r}, t) = -\mathbf{k}(t) \cdot \mathbf{r}$ onto the signal received from location \mathbf{r} , with \mathbf{k} defined as

$$\mathbf{k}(t) = \gamma \int_0^t \mathbf{G}(t') dt'. \quad (2.7)$$

Neglecting relaxation and field inhomogeneity effects, the total signal received from the sample after the application of the gradients can now be expressed as

$$m(\mathbf{k}) = C \cdot \int_{\mathbf{r}} \rho(\mathbf{r}) e^{-i\mathbf{k}\mathbf{r}} d\mathbf{r}, \quad (2.8)$$

with the constant C capturing all concomitant scaling effects. The desired measurement quantity is ρ , termed spin density, which describes the locally available equilibrium magnetization. The equation is easily recognizable as a Fourier integral, and $\rho(\mathbf{r})$ can be recovered via the inverse Fourier transform as

$$\rho(\mathbf{r}) = \frac{C}{(2\pi)^n} \int_{\mathbf{k}} m(\mathbf{k}) e^{i\mathbf{r}\mathbf{k}} d\mathbf{k}. \quad (2.9)$$

Here, n denotes the number of dimensions of the \mathbf{k} -space. Reconstruction of ρ of course crucially depends on a sufficient number of adequately distributed sampling points in \mathbf{k} . The overwhelming majority of MRI sequences is concerned with applying different strategies to sample the \mathbf{k} -space in both two or three dimensions. In conjunction with relaxation effects, appearing as additional time dependent weighting factors in the Fourier transform, this results in a very large number of possible contrasts in the resulting images. Depending on the applied pulse sequence, physical information about the coil \mathbf{B}_1 field distribution [56] (\mathbf{B}_1 mapping), the main magnetic field homogeneity (\mathbf{B}_0 mapping), or even temperature [57] can be extracted.

2.4 Spatially selective excitation

The described \mathbf{k} -space formalism in principle allows to acquire three-dimensionally resolved images from the whole sample. However, when only images from a specific subvolume are of interest, sampling the full volume introduces significant time overheads, and thus reduces the achievable resolution or prolongs the measurement unnecessarily. Hence, it is desirable to only create a transversal magnetization in a specified region. Spatially selective excitation can also be understood within the \mathbf{k} -space formalism introduced before. Within the low flip angle regime, it can be shown [58] that the concurrent application of temporally varying B_1^+ fields and gradients is related to a spatial variation of the transversal magnetization via

$$M_{\perp}(\mathbf{r}) = i\gamma M_0 \int_{\mathbf{K}} W(\mathbf{k}) S(\mathbf{k}) e^{i\mathbf{k}\mathbf{r}} d\mathbf{k}. \quad (2.10)$$

As before, this expression resembles a Fourier integral. The weighting function $W(\mathbf{k})$ represents the Fourier transform of the desired spatial excitation pattern, and $S(\mathbf{k})$ is a sampling structure capturing the trajectory in k-space, $\mathbf{k}(t)$, traversed by the gradients during the pulse playback. The relation to the $B_1^+(t)$ and gradient waveforms $\mathbf{G}(t)$ is given by

$$B_1^+(t) = W(\mathbf{k}(t)) |\gamma \mathbf{G}(t)|. \quad (2.11)$$

By defining a spatial pattern $W(\mathbf{k})$ and an appropriate gradient waveform with a sufficient coverage of k-space, the required pulse shape of B_1^+ can be directly calculated. The most ubiquitous application of selective excitation methods is the slicewise excitation. Even without invoking the k-space formalism, it can be intuitively understood. Overlaying the homogeneous \mathbf{B}_0 field with a linear gradient and playing back a shaped pulse with a specific center frequency and limited bandwidth, only regions possessing a Larmor frequency falling within the bandwidth would experience an excitation. Due to the linearity of the gradient field, this region resembles a slice. It should be noted, that this formalism allows the definition of not just slices, but arbitrarily shaped regions to be excited. However, the resulting pulse lengths are potentially prohibitive for direct applications, as relaxation effects occurring during the pulse playback can significantly impact the resulting pattern fidelity. Overcoming this drawback is one of the main motivations for employing parallel transmission techniques, which will be introduced shortly.

2.5 Electromagnetics of MRI coils

MRI coils are conducting structures carrying RF currents at the Larmor frequency in order to produce the \mathbf{B}_1 field inside the sample. A wide range of literature on the design and construction of coils exists. An overview can be found in the books by Mispelter [59] and Jin [60], which cover electromagnetic basics, classical coil design approaches and electronic circuit design considerations. Phased array coils are introduced and extensively analyzed in Roemer's seminal paper [14], and further investigations into their application and interactions can be found in papers by Wright [61, 62], Lee [63], Fujita [64] and Keil [65]. Most of the results pertaining to receive coil arrays are valid for transmit arrays as well. Some contemporary coil designs for high and ultrahigh field MRI include transmission line arrays [23, 24, 66, 67], concentric coils [68], degenerate birdcages [69], monopole [70] and dipole [27] approaches, multi-row arrays [29], and various loop-based arrays exploring advanced decoupling methods [26, 28, 71, 72]. This list is by no means complete, but can serve as a starting point for further investigations. In the following, some general aspects of the electromagnetics of MRI coils common to many of the mentioned designs will be presented. All currents and fields are assumed to be time harmonic, resulting in the well known correspondence $\frac{\partial}{\partial t} \leftrightarrow i\omega$.

2.5.1 Vector potential, magnetic induction and electric fields

For a filamental current I flowing along the contour C , the relation between current and the produced electromagnetic fields can be calculated through the vector potential \mathbf{A}

$$\mathbf{A}(\mathbf{r}) = \frac{\mu_0 I}{4\pi} \int_C \frac{d\mathbf{l}'}{|\mathbf{r} - \mathbf{r}'|}, \quad (2.12)$$

with the resulting magnetic induction field \mathbf{B}_1 given by

$$\mathbf{B}_1 = \nabla \times \mathbf{A}. \quad (2.13)$$

At the same time, an electric \mathbf{E}_1 field is produced as well, which is given by

$$\mathbf{E}_1 = -i\omega\mathbf{A}. \quad (2.14)$$

For now, conservative electric fields potentially originating from a charge separation along the conductor are neglected.

The concomitant electric field leads to a power deposition inside a conducting sample such as the human body. The total power dissipation in a volume V is given by

$$P = \frac{1}{2} \int_V \sigma(\mathbf{r}) |\mathbf{E}_1(\mathbf{r})|^2 dV. \quad (2.15)$$

This power deposition is usually nonuniform across the sample [2], even if the corresponding \mathbf{B}_1 field is homogeneous. As a result, localized tissue heating occurs, which can lead to localized tissue damage and a global increase in body core temperature. This is, of course, to be avoided.

Serving as a proxy for tissue heating, the specific absorption rate (SAR) is defined as the time-averaged power deposited in the human body.

$$\text{SAR} = \frac{P}{m} \quad (2.16)$$

The mass m corresponds to the exposed body mass. Limits to SAR, which have to be obeyed during an MRI procedure on humans, are defined in standards such as the International Electrotechnical Commission (IEC) standard 60601-2-33.

2.5.2 Wave impedance

The requirements for a well-performing MRI transmit coil can be stated as

1. Generate a strong and homogeneous B_1^+ field in a specific region of interest (e.g. head, body,...)

2. Minimize electric field exposure and power deposition over the whole body

The relation between electric and magnetic field components is given by the wave impedance Z_w , which is defined as the ratio of electric and magnetic field $|\mathbf{E}|/|\mathbf{H}|$. For plane electromagnetic waves in free space, this ratio is fixed at $Z_w = \sqrt{\mu_0/\epsilon_0} \approx 377 \Omega$, the impedance of free space. However, even at ultra high fields strengths with corresponding wavelengths of ≈ 1 m, MRI is predominantly a near-field phenomenon [48]. The impedance of a conducting structure in the near field is spatially varying, and determined by its geometry and current distribution. Based on the stated performance requirements, a low field impedance would be required for MRI coils. From basic electromagnetics, two prototypical field sources are well known: a short dipole and a small loop. While they cannot be distinguished in the far field, their near field behavior is considerably different, as is demonstrated in Fig. 2.1. Due to their significantly lower near field impedance, loop-like structures are the basic building blocks of most MRI coils. At the increasing frequencies coming with higher field strengths, the interaction of the coils with the human body is no longer strictly in the near field regime, and alternative configurations such as the dipole [27] or traveling waves [73] are becoming viable.

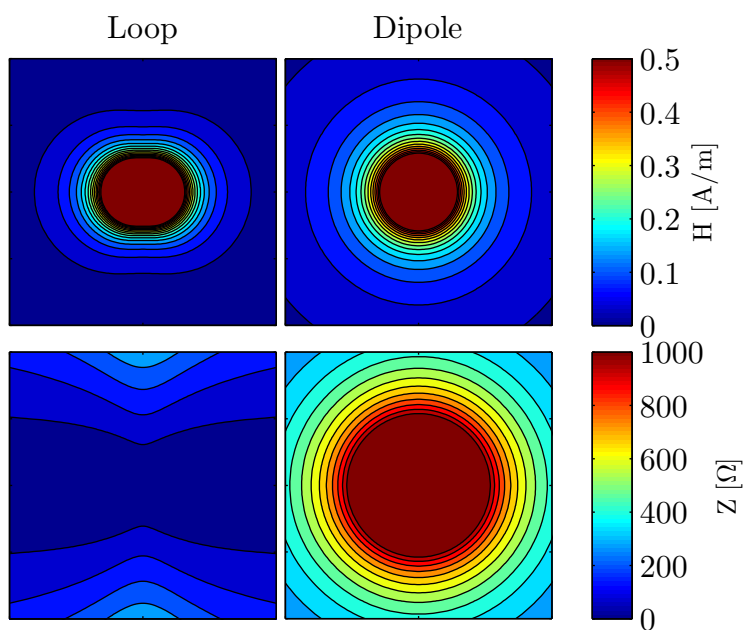


Figure 2.1: Magnetic field (top) and field impedance (bottom) of a small loop and short dipole, respectively, both driven with a current of 1 A. The loop has a much lower field impedance compared to the dipole. The dipole is oriented perpendicular to the shown plane, and the normal direction of the loop is oriented from left to right.

2.5.3 Tuning and Matching

In a circuit theoretical approach, a loop appears as an inductor, e.g. as having a positive reactance $i\omega L$ depending on the loop's inductance and the operating frequency. When it is brought close to a conducting sample, the aforementioned power deposition caused by the concomitant electric fields will manifest as an additional resistance R . Also contributing to this resistance are losses occurring in the coil conductor material, housing, capacitors, etc. and the total impedance of the loop is then

$$Z = R + i\omega L. \quad (2.17)$$

For MRI coil configurations, the resistance is typically below 50Ω , whereas the reactance can be much higher. Current flow is hindered by both resistance and reactance. In order to maximize the current, the inductance can be compensated by appropriate series capacitors satisfying the condition

$$C = \frac{1}{\omega^2 L}. \quad (2.18)$$

This capacitor is commonly referred to as tuning capacitor, as it tunes the coil to resonate at the Larmor frequency. It is customary to segment this capacitor into multiple series capacitors distributed along the coil. Introduced by Alderman and Grant [74], the segmentation ensures that the voltage across a single capacitor is now distributed over multiple capacitors, thus lowering the total voltage differential across each single one. This is necessary, because the electric fields across the capacitors also interact with the sample. The total electric field in this case becomes

$$\mathbf{E}_1 = -i\omega\mathbf{A} - \nabla\phi, \quad (2.19)$$

where $\nabla\phi$ is the conservative electric field originating from the charges stored on the capacitor. Segmenting the capacitors significantly reduces the impact of the conservative fields, and a properly built coil will almost exclusively interact with the sample via the induced rotational fields.

Having eliminated the reactance of the coil, it would now be possible to connect a voltage or current source in order to create a current flow in the coil. However, the currents required on the coils are on the order of 10 A or more, and taking the coil's resistance into account reveals required peak powers on the order of multiple kW. Such sources exist, albeit most commonly in the form of power amplifiers with an internal impedance of $Z_0 = 50 \Omega$. According to the maximum power transfer theorem, such an amplifier operates most efficiently when the impedance of the connected device is equal to its internal impedance. With most MRI coils exhibiting resistances of far less than 50Ω , the question arises on how to connect the coil to

the amplifier in an efficient manner. This is achieved by connecting the coil to the amplifier through a matching circuit, which transforms the coil's impedance to $50\ \Omega$ in order to allow maximum power transfer. The tuning and matching process is visualized in Fig. 2.2 for an example configuration. Many more matching schemes exist and are described in the mentioned introductory literature.

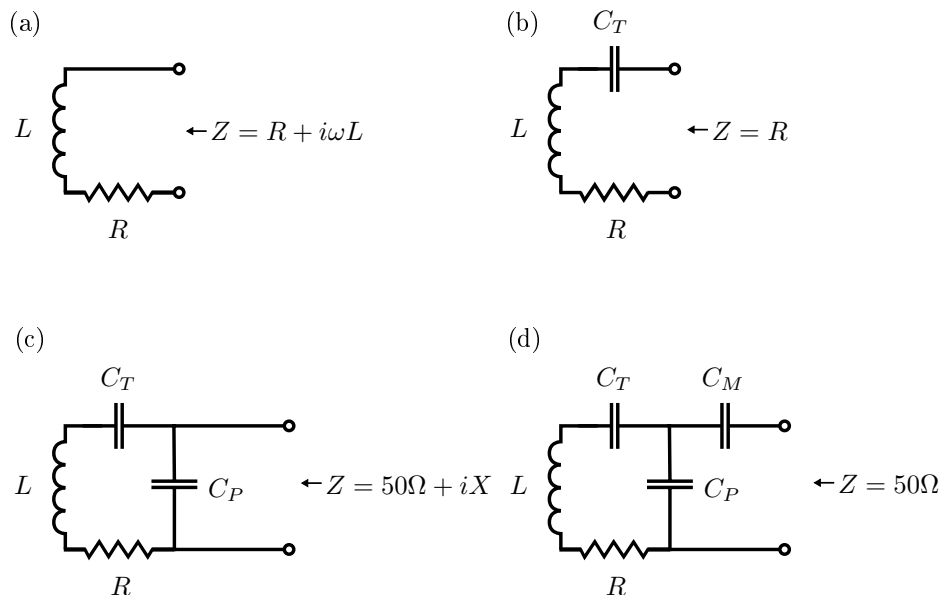


Figure 2.2: An MRI coil can be regarded as a series circuit consisting of an inductance and a resistance, resulting in a complex impedance (a). By inserting an appropriate series tuning capacitor C_T into the circuit, the reactance can be eliminated (b). The capacitor is usually split into multiple capacitors distributed evenly along the inductor. This setup now represents a series resonance circuit. Transforming it into a parallel resonance circuit as shown in (c), and carefully adjusting C_T and C_P allows tuning the impedance to a resistance of $50\ \Omega$ and an additional positive reactance X . Inserting a matching capacitance C_M allows compensating this reactance, leaving a purely real resistance of $50\ \Omega$ as is required for optimum power transfer.

2.5.4 Efficiency and Q-factor

As described before, the real part of a loop's impedance consists of multiple contributing resistances, which all reduce the current flowing in the coil for a given input power, and thus degrade its performance. While the resistance originating from electric field interactions with the biological sample cannot be avoided, other losses originating from the coil's components should be minimized. The Q-factor of a resonant system such as an MRI coil is defined as the ratio of its reactance and

resistance as

$$Q = \frac{\omega L}{R}. \quad (2.20)$$

A high Q indicates a weakly dampened system with little losses. It can be measured using a network analyzer, and measuring a coil's Q -factor with and without a sample can give an indication of its efficiency. With the intrinsic coil resistance R_C and the sample related resistance R_S , the unloaded Q -factor is $Q_U = \omega L/R_C$, and the loaded Q -factor is $Q_L = \omega L/(R_C + R_S)$. Their ratio

$$\frac{Q_U}{Q_L} = \frac{R_C + R_S}{R_C} = 1 + \frac{R_S}{R_C} \quad (2.21)$$

is an indicator of coil performance. A high Q -ratio indicates that most losses are unavoidable due to sample interactions, and the intrinsic coil losses play a minor role. The crossover value of 2 indicates equal contributions of coil and sample losses. This is also a rule of thumb for lower acceptable Q -factor limit for high field MRI coils. For signal reception, these losses also play a significant role, as the received noise is dependent on the total coil resistance. Assuming coil and sample are at a temperature T , and the receive bandwidth is Δf , the root-mean-square noise voltage measured is

$$v_n = \sqrt{4k_B T R \Delta f}. \quad (2.22)$$

R is the total coil resistance $R = R_C + R_S$, and k_B is the Boltzmann constant. At Q -ratios larger than 2, the noise is said to be sample dominated.

2.5.5 High frequency effects

The frequency increase due to higher static field strengths causes significant qualitative and quantitative changes in the \mathbf{B}_1 field distributions throughout a biological sample, which is in detailed studied analytically in Hoult's seminal paper [10]. Both the high permittivity of human tissues ($\epsilon \approx 6 - 90$ at 123 MHz), as well as their conductivity ($0.03 - 2.1$ S/m at 123 MHz) [75] have a detrimental impact. Inside a volume resonator the permittivity leads to standing wave features such as local field extrema and a central \mathbf{B}_1 field focusing, while the conductivity results in an appreciable surface field enhancement due to the skin effect. The impact of these effects on the \mathbf{B}_1 fields in a head-sized spherical phantom at 123 MHz and 300 MHz is shown in Fig. 2.3. It is important to note, that a homogeneous field distribution is not a solution to Maxwell's equations in the high-frequency scenario, where conductivity and permittivity effects cannot be ignored. Such homogeneity can only be achieved over smaller subvolumes, with the required current distributions outside the sample differing depending on the desired subvolume to be homogenized [10].

This is one of the main motivations for employing transmit coil arrays, as they allow a degree of control over their current distributions.

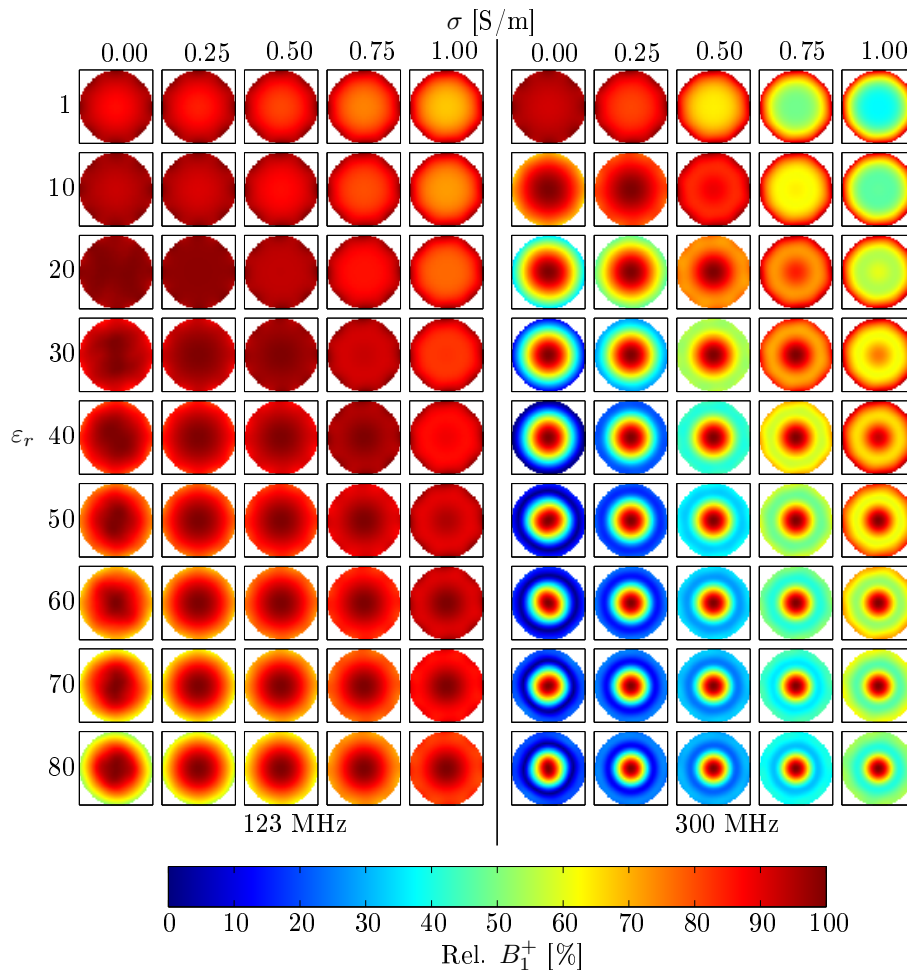


Figure 2.3: Effects of permittivity and conductivity on the B_1^+ field distribution inside a volume resonator loaded with spherical phantom at 123 MHz and 300 MHz. All plots are scaled to their individual maximum, so the comparison is purely qualitative. In air ($\epsilon_r = 1$, $\sigma = 0$), the B_1^+ field is very homogeneous at both frequencies. Increasing ϵ_r leads to a central brightening effect, which becomes apparent already at 123 MHz, but is significantly more pronounced at 300 MHz, where the B_1^+ distribution even shows complete voids. A conductivity increase, on the other hand, results in a peripheral field enhancement due to the skin effect. Again, the effect is much more strongly apparent at 300 MHz.

2.5.6 Coil arrays

Field superposition

In the presence of n filamental currents, the total vector potential as well as the resulting electric and magnetic fields are a superposition of the contributions of each individual current:

$$\mathbf{A}(\mathbf{r}) = \sum_{k=1}^n \frac{\mu_0 I_k}{4\pi} \int_{C_k} \frac{d\mathbf{l}'}{|\mathbf{r} - \mathbf{r}'|}. \quad (2.23)$$

This is a consequence of the Maxwell equations' linearity, and forms the basis for multi-channel coil arrays. Each individual coil represents one of the current paths, and the application of currents with different amplitudes and phases allows the generation of different spatial field distributions that are beneficial for the chosen application.

To exemplify the field distributions and properties of coil arrays, a virtual eight-channel coil array for 7 T head MRI was constructed, i.e. a computer model of a non-existing coil. The coil design is depicted in Fig. 2.4.

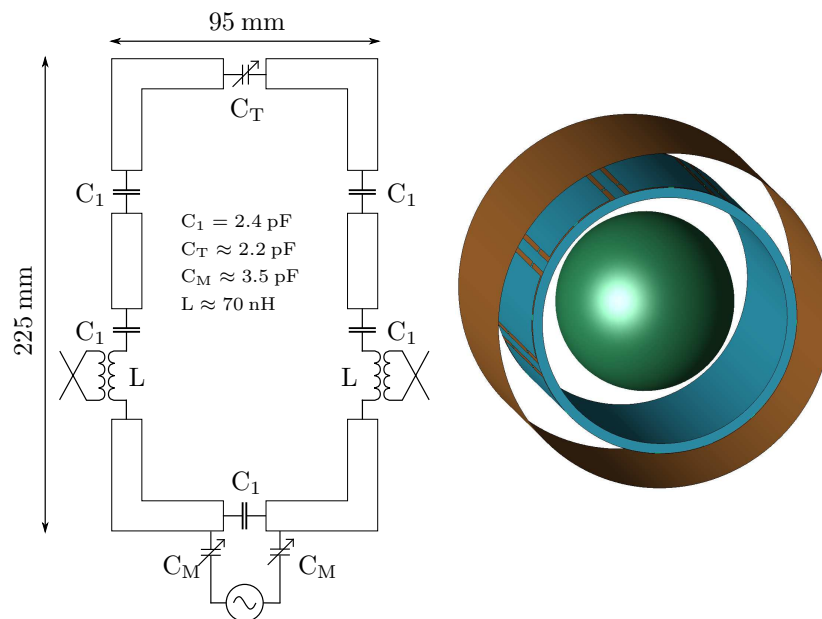


Figure 2.4: Design of the virtual 8-channel array. It consists of eight transformer decoupled [26]rectangular loops arranged conformally on a cylindrical former (right). The aforementioned tuning- and matching capacitors are depicted in the single coil element schematic on the left. The coil is loaded with a homogeneous spherical phantom containing tissue-mimicking gel with a permittivity of $\epsilon = 55$ and a conductivity of $\sigma = 0.66 \text{ S/m}$. (Figure taken from [43])

The distributions of B_1^+ are shown in Fig. 2.5, and corresponding electric fields are shown in Fig. 2.6.

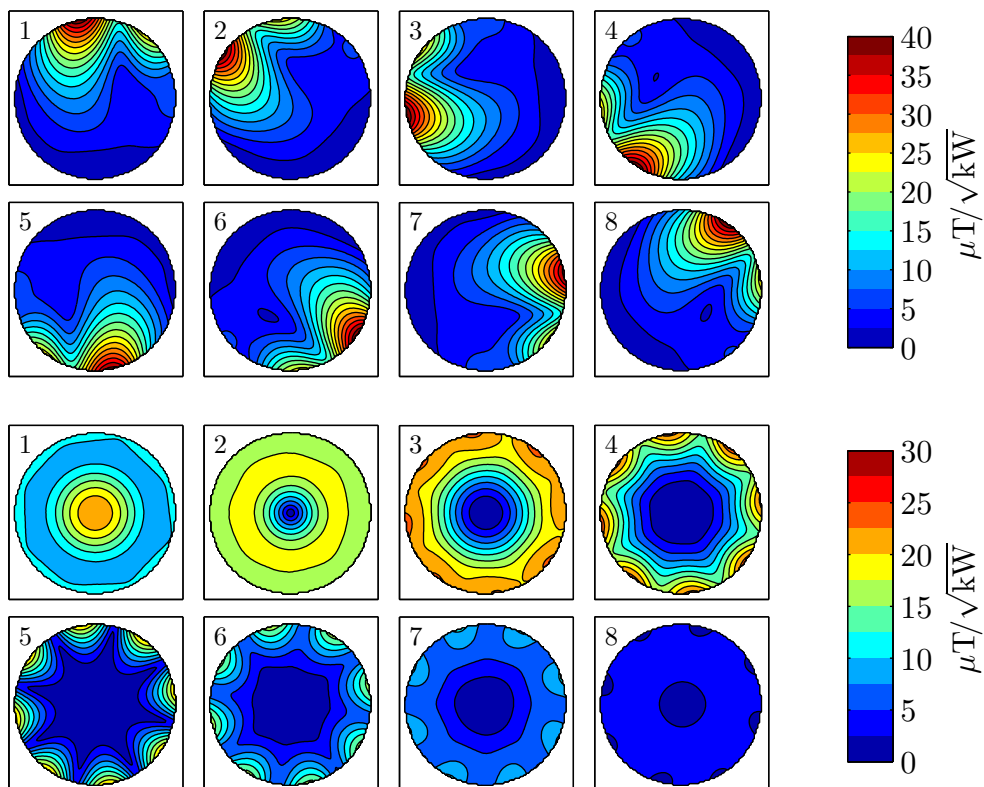


Figure 2.5: Single-coil magnitude B_1^+ field distributions of the 8-channel array are shown on top. The distributions are identical, but incrementally rotated by 45° . The numbering corresponds to the channel number. The resulting B_1^+ fields when concurrently driving the the individual channels with currents of the same amplitude but different phase offsets are shown below. Here, the numbering corresponds to the nearest-neighbor phase offset between the currents, with 1 representing a phase shift of 45° , 2 representing a phase shift of 90° and so on. Higher nearest-neighbor phase shifts correspond to the B_1^+ being increasingly concentrated on the periphery of the phantom. Only the first mode has an appreciable field intensity in the center, and the aforementioned field focusing effect is clearly visible. The mode #8 corresponds to all elements being driven with the same phase, resulting in a negligible B_1^+ field. The eight depicted modes correspond to the well-known Eigenmodes of degenerate birdcage resonators [69].

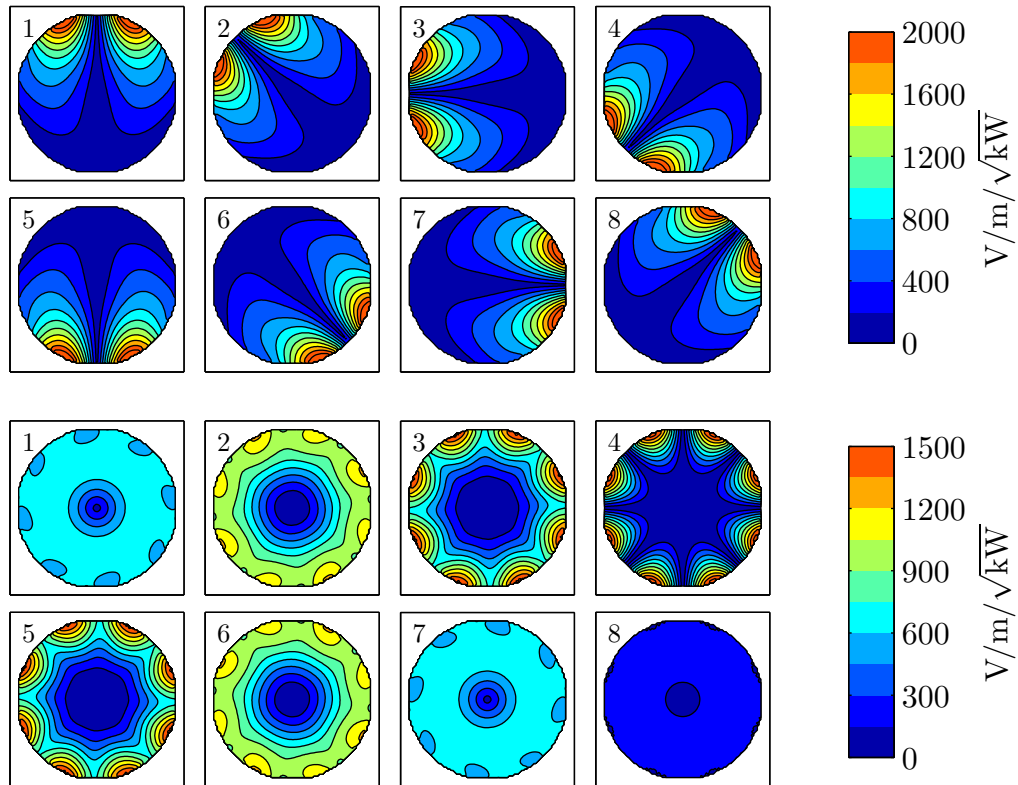


Figure 2.6: Single-coil magnitude E field distributions of the 8-channel array are shown on top, and the concurrent drive electric fields are shown in the bottom. Similar to the B_1^+ , higher order modes concentrate the fields in the periphery. However, the electric field is zero in the center independent of the mode. While the B_1^+ fields for all modes differ, the electric field distributions show a degeneracy, with modes 1 and 7, 2 and 6 as well as 3 and 5 being identical. This discrepancy is explained by the symmetry breaking induced by splitting the magnetic induction field into B_1^+ and B_1^- . The total field B_1 shows the same degeneracy as the electric fields.

Coil interactions

Multiple sources producing interfering electromagnetic fields will interact under most circumstances, which has been investigated extensively in the context of MRI coils [14, 61, 63]. These interactions can be described within the framework of impedance matrices, which extends the concept of impedance to multi-source environments. For the moment, all coils will be considered to be unmatched, that is voltage sources are directly connected to the coils. An n -channel coil array can now be treated as a passive n -port circuit characterized by its impedance matrix \mathbf{Z} , which relates the currents and voltages occurring on the coil elements via $\mathbf{v} = \mathbf{Z}\mathbf{j}$, with \mathbf{v} and \mathbf{j} representing the source voltages V and coil currents I arranged in a vector, respectively.

The elements Z_{ij} of the impedance matrix \mathbf{Z} are defined as

$$Z_{ij} = \left. \frac{V_i}{I_j} \right|_{I_k=0 \text{ for } k \neq j}. \quad (2.24)$$

They are determined by driving one port with a known current, terminating all remaining ports with an open circuit and measuring the voltages at each port. A specific set of source voltages \mathbf{v} results in currents on the coils that can be calculated by $\mathbf{j} = \mathbf{Z}^{-1}\mathbf{v}$. For a passive linear network, \mathbf{Z} is symmetrical, i.e. $Z_{ij} = Z_{ji}$.

The diagonal elements represent the self-impedance of the individual coil elements, containing a real part corresponding to the coil- and sample losses as well as an imaginary part corresponding to the coil's reactance. The off-diagonal elements contain information about the interactions between two coil elements, and can also be grouped into reactive and resistive contributions. The most common, and also most significant interaction mechanism is given by a mutual inductance M_{12} between coils. For two closed current paths C_1 and C_2 , it is defined by the Neumann integral

$$M_{12} = \frac{\mu_0}{4\pi} \oint_{C_1} \oint_{C_2} \frac{d\mathbf{l}_1 d\mathbf{l}_2}{r}, \quad (2.25)$$

with $d\mathbf{l}_1$ and $d\mathbf{l}_2$ representing an infinitesimal segment along the contours C_1 and C_2 , respectively, and r being their distance. With two coil elements having a mutual inductance M , their mutual impedance is $i\omega M$. Another interaction is given by mutual resistance effects, which are only present in case both coils are loaded with a lossy sample, and the mutual resistance R_{12} is proportional to the electric field interactions inside the material via

$$R_{12} \propto \iiint_V \sigma \mathbf{E}_1 \mathbf{E}_2^* dV. \quad (2.26)$$

The combined effect of these interactions manifests in a total mutual impedance $Z_{12} = R_{12} + i\omega M_{12}$.

Coil decoupling, meaning the reduction or elimination of these effects is essential, as coupling significantly complicates coil manufacturing by introducing resonance line splitting and impeding the ability to properly match the coil elements to the transmit/receive circuitry. In theory, coupling does not impact achievable SNR during reception as long as the channel correlation is taken into account [76] during image reconstruction and the preamplifiers are assumed to be noiseless. However, realistic preamplifiers are noisy, and coupled coil arrays allow the crosstalk of noise waves originating from the preamplifiers, leading to a modest degradation in receive performance [77]. During transmission, the available power for excitation is reduced as coil coupling leads to an undesired power deposition in the amplifiers' dummy loads. Most techniques focus on eliminating the mutual inductance (see e.g. [14, 26,

63, 78]), however some techniques to also eliminate mutual resistance have emerged recently as well [28]. Their impact on coil performance will be briefly analyzed on a theoretical basis in chapter 4.

In a real setup, coil interactions will be measured with the full matching network present. For this purpose, the scattering matrix approach is more useful, which does not relate port currents and voltages, but rather incident and reflected waves \mathbf{a} and \mathbf{b} [79]. They are defined via the port currents I and voltages V as $a = (V + Z_0 I) / (2\sqrt{Z_0})$ and $b = (V - Z_0 I) / (2\sqrt{Z_0})$, given a real characteristic impedance Z_0 . Both are related via the system's scattering matrix via $\mathbf{b} = \mathbf{S}\mathbf{a}$. The diagonal elements of \mathbf{S} indicate how well a coil element is matched, while the off-diagonal elements give a measure of coil coupling. It is customary to present the coupling matrix on a logarithmic scale, with diagonal elements of less than -20 dB indicate a well matched coil receiving 99% of the power delivered by the amplifier. Non-decoupled coil elements can exhibit a coupling of more than -7 dB, and the goal of most decoupling measures is to lower these interactions below -15 dB if possible. Based on the scattering matrix, it is possible to calculate the total power absorbed in the coil and sample for arbitrary driving voltages at the sources. This will be discussed in detail in chapter 4.

2.5.7 Numerical techniques

Analytical solutions to the field distributions of MRI coils are only available for simple geometries. While these benchmark cases can give deep insight into most phenomena, predicting the behavior of a coil or coil array in a realistic setting is very helpful for making coil design decisions. To this effect, a large number of numerical techniques have been applied to solve for the electromagnetic field distributions of coils using realistic geometries and numerical models of the human body [80]. One of the most commonly used methods is the finite-difference time-domain (FDTD) technique. Introduced by Yee [81], it is used for solving Maxwell's equations on a discrete spatial grid in the time domain. An extensive introduction to the method can be found in Taflove's textbook [82]. The advantages over other methods are its capability of modeling arbitrarily complex geometries with the memory requirements only being proportional to the overall number of grid cells. It can be easily optimised for massively parallel computing environments, and the use of state-of-the-art general purpose graphics processing units (GPU) has reduced simulation times by an order of magnitude compared to computations on multi-core CPUs. A common simulation would involve digitally constructing the coil under investigation, including realistic boundary conditions given by the MRI scanner, circuit components, and including a digital human model with a realistic positioning inside the coil. After transforming the continuous geometry into a discrete grid, energy is fed into the coil via the application of a voltage pulse. The algorithm then steps through the temporal field response of the system with discrete time steps, the fields can be recorded where desired. A discrete fourier transform can then extract the steady-state fields

at the desired MRI coil frequency. It is important to sample the response until all of the energy put into the system via the pulse has either been absorbed or radiated through the boundaries. Failure to do so will result in truncation artifacts [83].

For an accurate representation of electromagnetic phenomena and a reduction of numerical artifacts resolutions of about 15 cells per wavelength are required. Modeling fields in water at 300 MHz would hence require a spatial resolution of 7 mm, in air about 7 cm would be sufficient. However MRI coils have features in the millimeter range which need to be resolved. This is also true for high resolution digital human models [84]. Hence, the smallest cell in the computational space can be on the order of 1 mm^3 or even below. A drawback of the method is, that the discrete timestep length is determined by the smallest cell size, with smaller cells requiring proportionally shorter timesteps. Hence, more timesteps are required to iterate through the temporal response, which prolongs simulation time. A careful balance between desired accuracy and simulation runtime has to be found.

Computation time will additionally depend on the Q-factor of the system, as this determines how quickly the energy gets absorbed. High-Q resonators, such as MRI coils, can take multiple microseconds until the energy levels have sufficiently decayed. With timesteps on the order of picoseconds, this corresponds to multiple million timesteps, taking more than a day of real time for computation. The fields crucially depend on the reactive elements, such as capacitors, in the structure, and the exact values are not known beforehand and are usually found iteratively until the simulated scattering matrix matches expectations. As the number of required iterations for sufficient tuning, matching, and decoupling is not deterministic and, depending on the model complexity, can easily reach triple digits, this leads to prohibitively long simulation times.

The linearity of Maxwell's equations can be leveraged to significantly speed up this process. Replacing all discrete components in the structure by sources and exciting them consecutively, a large scale dataset consisting of port and field data can be assembled. The field distributions for the sources being replaced by arbitrary linear components such as capacitors can then be calculated as a linear superposition of the large scale datasets. The weighting factors depend on the actual components used, and can be calculated within circuit co-simulation programs in a matter of seconds. This significantly speeds up the simulation process, as the lengthy iterative repetitions have been shortened. The additional calculation time due to the larger number of ports is offset by the decrease in simulation time of a single simulation: as the structure is no longer resonant, it has a low Q-factor and thus simulations are significantly shorter. The co-simulation approach is described in detail by Kozlov [85], Lemdiasov [86] and Beqiri [87].

Taken together, GPU acceleration in conjunction with co-simulation approaches allow completely modeling a complex multi-channel coil array within a matter of a few days. This significantly speeds up the coil building process, as design decisions can be quickly evaluated before the actual construction.

All simulations shown in this work were performed using XFDTD 7.4 (Remcom, State College, USA) for the 3D field simulations, and ADS (Agilent, Santa Clara, USA) as the co-simulation solver. All post-processing and field combination was done using Matlab (The MathWorks, Natick, USA).

2.6 Parallel transmission

With the principles of MRI and the electromagnetics of coils having been established, a short overview of parallel transmission applications will be given. An in-depth overview of pTx techniques can be found in the review papers by Katscher [12] and Padormo [13].

An important prerequisite for these techniques is a knowledge about the transmit field distribution. Especially at high frequencies, the B_1 distribution can be strongly subject dependent, making it necessary to acquire spatially resolved B_1^+ magnitude and phase maps using so-called B_1 -mapping sequences. A review on the application and performance of different mapping techniques was published by Stollberger et al. [88], and more recently by Pohmann et al. [56].

2.6.1 B_1 -shimming

The most basic parallel transmit technique is B_1 -shimming. It consists of finding a specific linear combinations of the single-channel coil fields under a given set of constraints, such as a maximized mean B_1^+ magnitude in a region of interest, or a sufficient B_1^+ homogeneity. The total B_1^+ field of an n -channel array is given as a weighted sum of the individual channel fields $B_{1,k}^+$ via

$$B_{1,total}^+ = \sum_{k=1}^n \alpha_k e^{i\phi_k} B_{1,k}^+. \quad (2.27)$$

Here, α_k is a magnitude weighting factor representing the driving voltage magnitude for the coil element k , and ϕ_k is a phase shift of the respective voltage. Other factors such as concurrent minimization of locally or globally absorbed power also can come into play [20], resulting in potentially complex optimization target functions [89]. Analytical and semi-analytical approaches have been investigated as well [90, 91]. Once a satisfying field combination has been found, it is kept constant throughout the MRI experiment. Often, the optimization is restricted to adjusting the phase of the individual coils only. An example of phase-only B_1 -shimming is given by the previously shown modes of the exemplary eight-channel coil array in Fig. 2.5.

2.6.2 Time-interleaved Acquisition of Modes

The time-interleaved acquisition of modes (TIAMO) technique sits between simple B_1 shimming and more complex parallel transmission techniques [17]. It leverages the complementarity of the field distributions of differently B_1 shimmed excitation modes. Combining images acquired using different excitation modes, e.g. mode 1 and 2 in Fig. 2.5, yields a resulting composite image with a significantly improved homogeneity. It has been successfully applied at field strengths up to 9.4 T (400 MHz) [92].

2.6.3 Transmit SENSE

The most powerful parallel transmission technique is given by transmit SENSE [12, 18]. It extends Pauly's spatially selective excitation concept introduced in section 2.4 to utilize the additional degrees of freedom offered by multiple transmission coils with spatially distinct B_1^+ profiles. Within the framework given in Eq. 2.10, each coil with a sensitivity profile $\mathbf{S}_i(\mathbf{r})$ excites an undersampled spatial pattern $W_i(\mathbf{r})$, so that their combination is the desired spatial target pattern. The advantage over selective excitation with one coil only are the significantly shortened RF pulses that are possible by traversing an undersampled trajectory in k-space during the pulse playback. This is analogous to parallel reception techniques [15], where multiple coils are utilized to acquire a fully resolved image while undersampling k-space. It has been demonstrated, that the quality of the resulting excitation pattern is directly related to the acceleration factor, which is limited in turn by the number of available independent RF-channels [93].

The required excitation pulses to be played out on each transmit channel can be calculated with a variety of techniques [18, 94–99]. The pulses for spatially selective excitation shown in both the experimental and theoretical work of the present thesis were calculated following the approaches detailed by Grissom [95] and Yip [99]. The techniques were implemented by Tomasz Lindel and Patrick Waxmann at the PTB in Berlin during their PhD theses, and were thankfully made available for the required pulse design tasks.

2.7 Signal synthetization

MRI requires a highly stable signal source in order to generate the excitation pulses to be fed into the coils. Being sensitive to phase, even slight phase changes or jitters due to timing instabilities can be significantly detrimental to image quality. Most commercial vendors implement some form of single-side-band (SSB) modulation to generate the required pulses, similar to the setup shown in Fig. 2.7. For a transmit array configuration, the shown setup needs to be replicated for each channel, on order

to allow the creation of completely independent pulse shapes in amplitude, frequency and phase. The following chapter will present an alternative to this approach and demonstrate its feasibility for parallel transmission experiments.

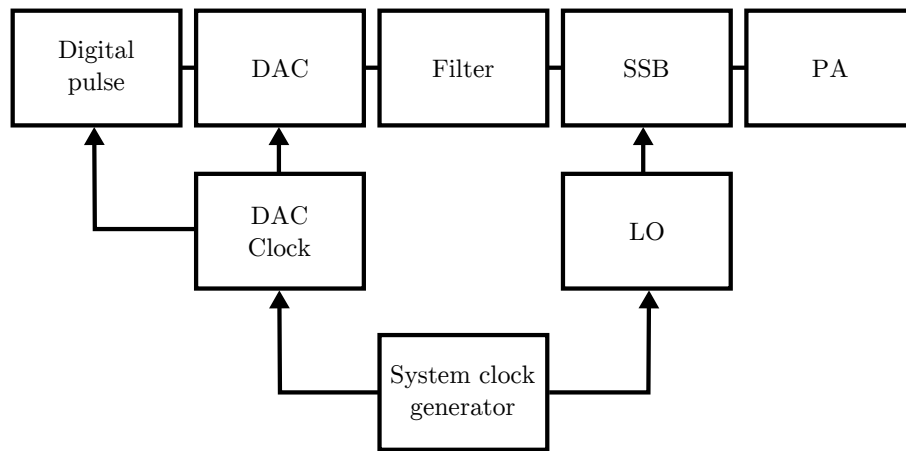


Figure 2.7: Exemplary design of an MRI scanner's transmit signal chain. The basis for an accurate frequency is the system clock generator, which is usually temperature stabilized. The system's local oscillator (LO) is derived from this frequency, and is usually close to the required Larmor frequency within a few MHz. The pulse shape is digitally generated, and converted to an analog signal, which is subsequently filtered to remove harmonics from the conversion process. The frequency of this signal is on the order of a few MHz. When mixed with the local oscillator signal in the SSB unit, the resulting signal is exactly at the desired Larmor frequency. Usually, the LO signal is variable within a certain band to allow the generation of pulses within the required bandwidth.

3 Design and application of a scalable multi-channel RF signal generator

While multi-channel transmission coils with eight or more channels are increasingly common [28, 100], the number of available RF channels is rarely seen to be higher than eight. As opposed to custom-built RF coils, the just described signal synthesis chain is usually not easily modifiable by the user due to its very tight integration with the scanner hardware architecture. Hence, an extension of the available channels is complicated, as not all information required for a synchronous operation of additional hardware is available.

The aim of the subsequently presented setup is to design and build a completely independent RF transmit chain and interface it with a Siemens Verio 3T MR scanner, thus circumventing issues arising from the synchronization of external equipment. The focus is set on a small footprint and low price, in order to build a foundation for an easily extensible large-scale parallel transmission architecture. Additional goals were the capability for a broadband operation and straightforward integration with existing MR scanners across vendor platforms.

3.1 Hardware design

3.1.1 Concept

The hardware design approach for the signal generator is detailed in Figure 3.1. Broadly speaking, the desired MR pulse is digitally generated at an intermediate frequency, and consecutively transformed to the required excitation frequency, converted to an analogue signal, filtered and passed to the power amplifiers. In contrast to the previously detailed standard signal chain, the presented setup lacks the SSB modulator and instead performs the required frequency conversion directly in the signal processing blocks of the DAC. The design concept and the utilized components will be described in detail hereafter.

The hardware can be divided into analog and digital components, each housed in a separate 4HE 19" case. The digital signal is generated by digital pattern generators

M2i.7020 and M2i.7021. These addon cards are housed inside a control PC, which is also running the software required to program and control the signal generator. The digital signal is then fed into digital/analog converters (DAC 5687), which digitally upconvert the signal to the required frequency. The analog signal output is then fed through bandpass filters in order to remove unwanted frequency components from the signal. The filtered output is finally fed into the power amplifiers.

Synchronization to the MR scanner is achieved via a 10 MHz reference clock signal which is generated by the scanner console and ensures frequency stability of the additional hardware. The MR pulse output is triggered through an unblanking TTL pulse generated by the scanner for every pulse that is to be transmitted. This signal is also fed into the additional Dressler power amplifiers for unblanking.

Additional sequence programming is reduced to replicating the RF playback structure of the desired sequence on the home-built pTx system. The hardware needs to be programmed to play back the required pulse whenever a trigger event is received.

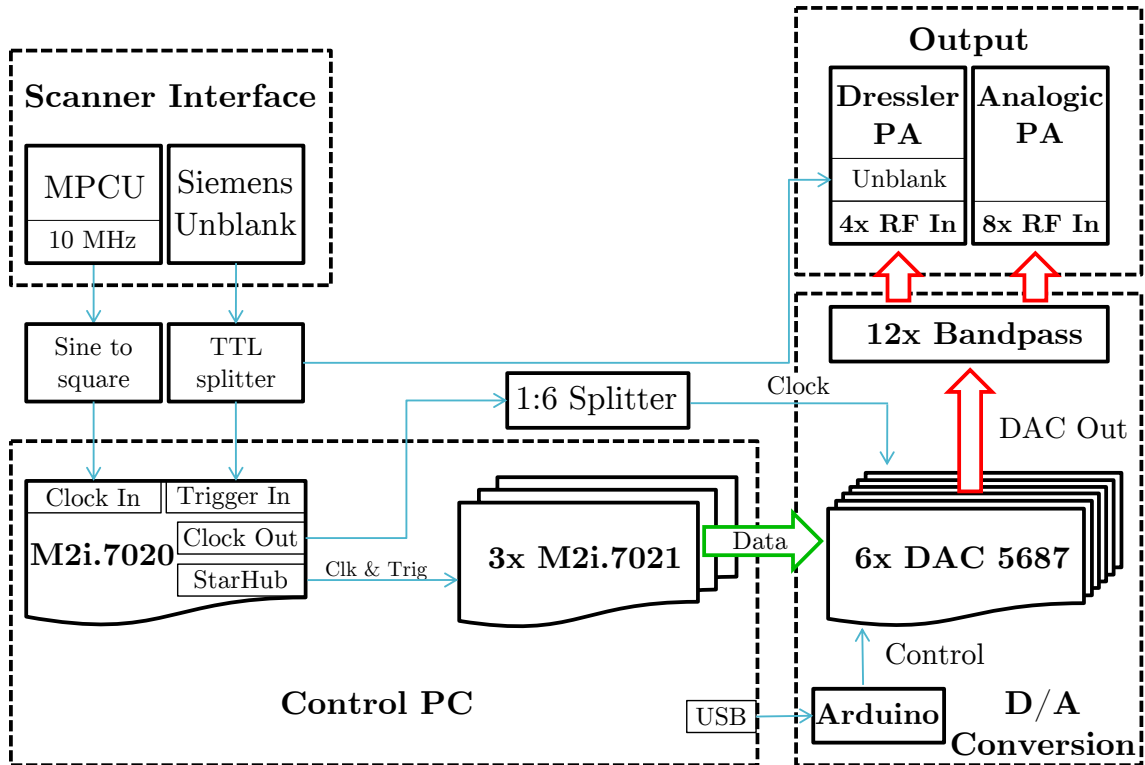


Figure 3.1: Hardware design concept for the signal generator. Thin arrows depict control signals, whereas bold arrows show pulse signal flow, which is further subdivided into digital (green) and analog (red) stages.

3.1.2 Digital signal hardware

Hardware specifications

The control PC contains three TTL compatible M2i.7021 PCI-Express digital pattern generator cards (Spectrum GmbH, Germany), used for signal creation and output, as well as a single M2i.7020 PCI card acting as a control and synchronization hub.

The M2i.7021 can output arbitrary of 64-Bit words at arbitrary sampling rates of up to 60 MS/s, and the output waveforms can be stored in the 256 MiB onboard memory. In order to synchronize the card to external signals, an input clock channel (Clock In) is provided to supply a reference clock signal for the internal phase-locked loop (PLL). The internally used clocking signal derived from the PLL can then be fed into external components if required (Clock Out).

An advanced internal triggering engine allows the combination of up to two trigger signals fed into the trigger input (Trigger In) via logical AND and OR operators in order to start pulse playback based on a large variety of conditions. Upon detection of a trigger condition, a TTL trigger signal can be generated for synchronization of additional hardware (Trigger Out). Several modes are available to configure pulse playback following a trigger event. It is possible to playback the complete memory or arbitrarily chosen memory segments, and looping modes are available for repeated playback of specific pulse sequences.



Figure 3.2: M2i.7021 extension card used for the digital signal generation.

As opposed to conventional MR signal synthesizers, where the amplitude, phase and frequency modulation required for pulse formation is imposed upon an independently generated carrier wave close to the Larmor frequency in discrete steps, the present setup synthesizes a digital signal corresponding to an appropriately modulated high frequency pulse. This approach allows a very fine-grained control over the signal output which has been shown to have advantages over the standard implementation done by some MR vendors [31].

DACs operating in the required frequency range usually feature a resolution of 16 Bit, which is sufficient to generate MR pulses at the required fidelity. Consequently, the 64-Bit digital output of one card can be utilized to drive four 16-Bit transmission channels, resulting in a total of twelve channels for the complete setup.

Multi-card synchronization

Each of the cards can act independent from the others, however, in the context of MRI parallel transmission, a synchronized playback is required. For this purpose, a so-called “Star-Hub” is available from the vendor. It consists of a small add-on module for one M2i card, which can then distribute common clock and trigger signals to up to four additional cards. For legacy reasons [38, 101], an additional pattern generator with an integrated StarHub was available (M2i.7020), and thus used for synchronization (see Fig. 3.3). In principle, this 32-Bit card could drive two additional channels, which was, however, not required for the present work.

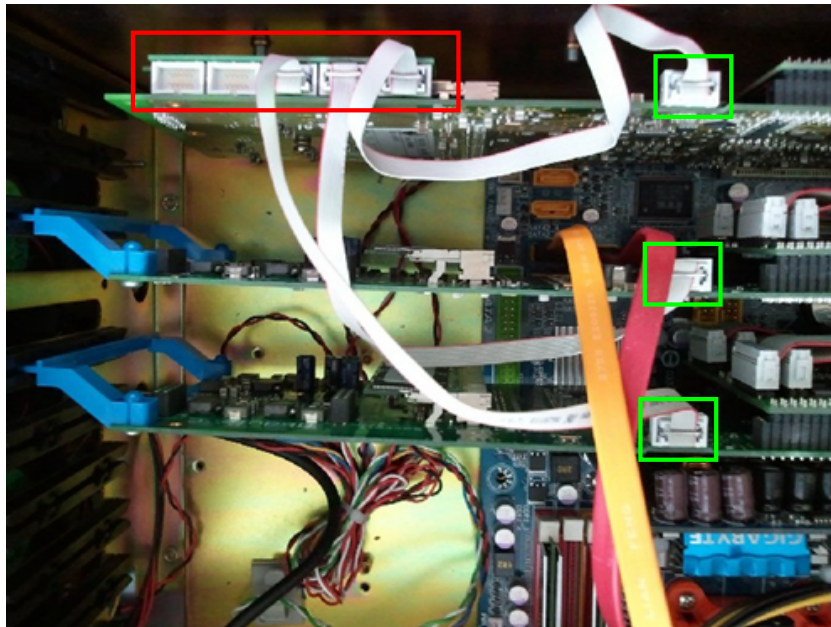


Figure 3.3: Synchronization setup using the StarHub (red box). The hub is attached to one of the cards (M2i.7020), and distributes the clock- and trigger signals to the other cards and also back to itself (green boxes). This allows an exact synchronization without phase or trigger delays. The shown picture lacks the third card used in the final setup.

Sampling rate selection

The maximum digital sampling rate is too low to directly synthesize a signal at the required Larmor frequency. This is alleviated by the DACs’ frequency up-conversion

capabilities. Consequently, an internal sampling rate of 44 MHz was chosen, and the digital signals along with a 44 MHz clock signal were fed into the DACs. The frequency up-conversion process will be described in the following subsection.

3.1.3 Digital/Analog conversion

DAC Specifications

The signal generator employs four Texas Instruments DAC5687 digital-to-analog converters, each offering two 16-bit channels at a maximum sampling rate of 500 MHz. It additionally offers digital signal processing capabilities for sampling rate conversion and signal interpolation, which allows the input signal at a 44 MHz sampling rate to be converted to the Larmor frequency at approximately 123.2 MHz. While the DACs are usually sold as an integrated package only, a vendor-supplied test and evaluation board with common interfacing ports was used for the setup (Fig. 3.4).

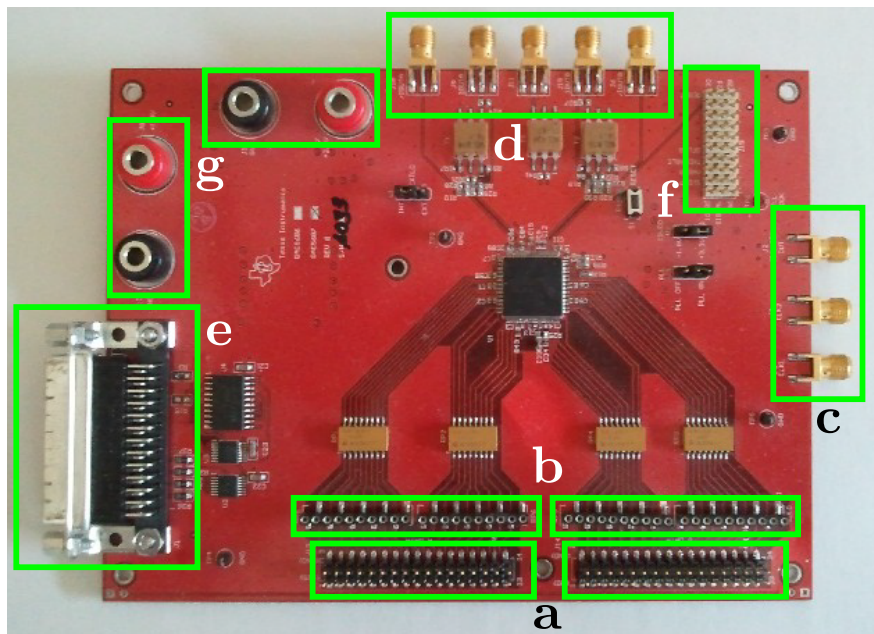


Figure 3.4: Layout of the DAC. The two 16-Bit digital signals are fed into the board through the connectors (a). Appropriate termination resistors can be inserted into the input lines (b) in order to decrease ringing. Clock signals are fed into the appropriate SMA connectors (c), depending on the chosen clocking mode. Real, complex or summed output signals are output through the connectors (d). The parallel port connector (e) allows access to the programming registers of the DAC in order to set up the DAC operation modes. The jumper switches (f) can be used to set additional options. Operation input voltages of 3.3 V and 1.8 V are provided through the connectors (g).

The six DACs were operated in real output mode (one output port per channel) and were clocked using the single-ended clock signal from the M2i cards. In order to supply an identical clock signal to all DACs, the single clock output signal was distributed to the DACs using a 1:6 power splitter and identical cables, ensuring a coherent output between all channels.

Frequency up-conversion

The DAC5687 was operated in the so-called “X4L”-mode, which employs two sampling rate converters, frequency mixers and digital FIR high-pass filters in order to shift the output signal to the desired frequency. With a fixed sampling rate of 44 MHz, the modulated MRI carrier signal needs to be digitally created at a frequency around 8.8 MHz. The conversion process to up-convert this signal to the required frequency of 123.2 MHz is detailed in Figure 3.5.

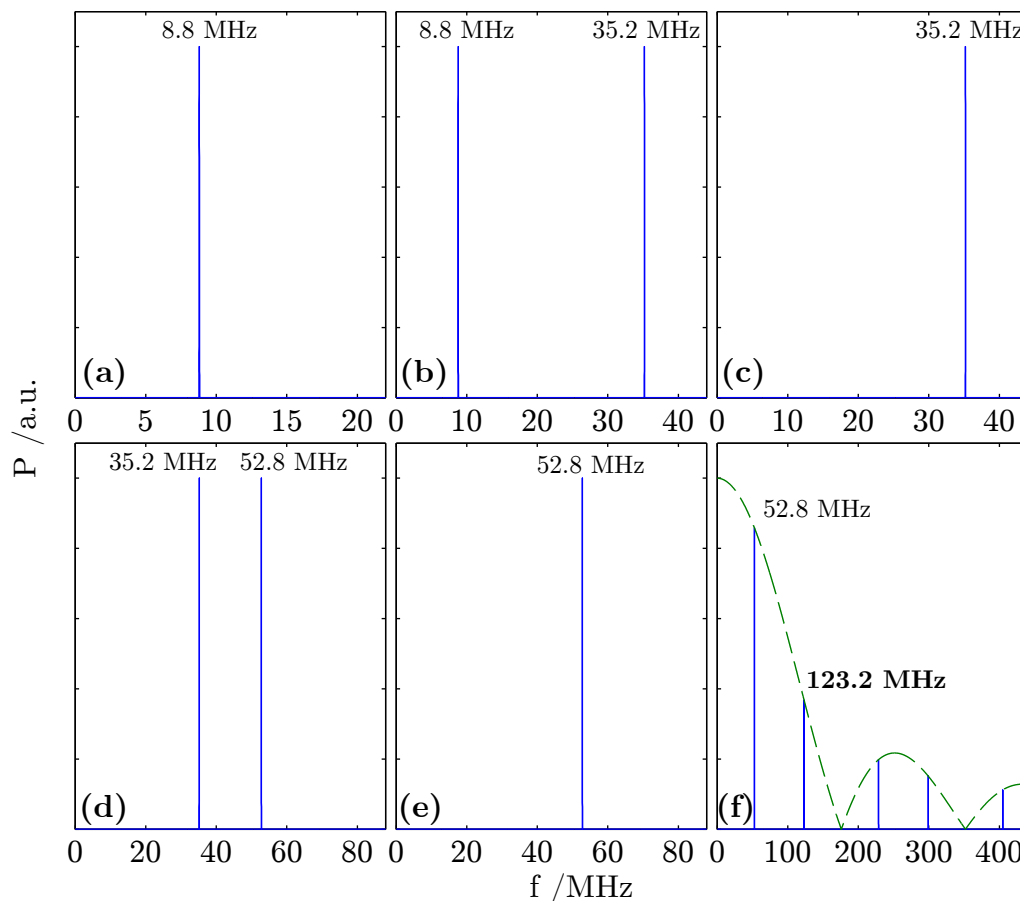


Figure 3.5: Depiction of the DAC frequency up-conversion process. The digital pattern generators create a harmonic signal with a frequency of 8.8 MHz with a sampling rate of 44 MHz (a). In the first up-conversion stage, the sampling rate is doubled and the data is digitally mixed with a sinusoidal signal at the Nyquist limit. This results in an additional image frequency component at 35.2 MHz (b). The original 8.8 MHz signal is removed through a FIR high-pass filter. The up-conversion and mixing is repeated (d, e), resulting in a signal at $f = 52.8$ MHz with a sample rate of $f_s = 176$ MHz, which is fed to the DAC output stage. The resulting analogue signal spectrum is depicted in (f). Due to the periodicity of the digital/analog conversion, the spectrum contains image signals at $n \cdot f_s \pm f$, which are attenuated by the characteristic “sinc” response of a sample-and-hold DAC (green dashed line). The first image frequency corresponds to the desired MR frequency. The other frequency components are then removed via analogue band-pass filtering

Setup & Control

In order to set the DAC into X4L mode and adjust additional settings such as gain, the control registers of the DAC need to be accessed and properly set. This is possible through the integrated SPI bus, which is accessible through a 25-pin D-sub connector.

While a single DAC can be conveniently programmed using a vendor supplied cable and software, this does not allow the use of multiple converters in one system. In order to conveniently program all DACs, an Arduino-based microcontroller was employed (Arduino Duemilanova Mega, www.arduino.cc). The microcontroller is connected to the control PC via USB, and was programmed to receive input signals through its integrated serial console and translate these inputs into appropriate SPI commands for the DAC. Convenient removable connection to the individual DACs was achieved by designing an add-on-board for the Arduino (“shield”), which connects the required Arduino output pins to ribbon cable jacks, which in turn connect to the DACs via ribbon cables. This setup proved robust and flexible, and can be easily extended to more than four DACs. For convenience, the required default register values were automatically written to the DACs upon connecting the Arduino to the USB port.

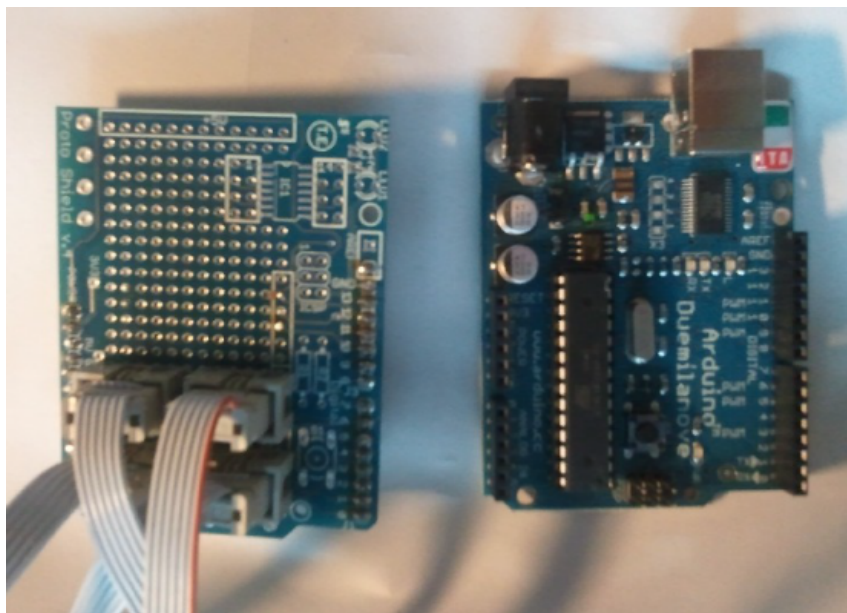


Figure 3.6: Depiction of the Arduino microcontroller board (right) and the add-on shield (left) used to connect to the DAC.

Analog Filtering

Spectral signal components sufficiently far from the Larmor frequency have no impact on the spin system. However, if the DAC output signal containing these undesired frequencies is fed into the power amplifiers, the amplifiers will saturate at lower input levels, which would hamper the achievable dynamic range and maximum output power. Hence, all spectral components besides the desired 123.2 MHz signal were removed using a low- and highpass filter to form a band-pass. To this end, a Mini-Circuits SLP-150 low pass filter and SHP-100 high-pass filter were cascaded.

The output components closest to the MR frequency are located at 52.8 MHz and 228.8 MHz, where the filter cascade offers an attenuation of more than 35 dB, with the remaining high frequency components being dampened by more than 60 dB.

3.1.4 Scanner interfacing and synchronization

Clock signal extraction

The Siemens Verio uses a 10 MHz clocking signal for internal synchronization. This signal is also accessible to the user via the Measurement, Physiological & Communication Units (MPCU), and it was thus utilized as the PLL reference of the digital signal cards. While the provided signal is sinusoidal with a 1V amplitude, the M2i cards expect a TTL-level square wave clock signal. To this end, the signal was first fed into the reference input of an arbitrary signal generator (Tektronix AFG3102), which in turn generated a square wave signal to be fed into the M2i clock input.

Receive phase compensation

While the previously described synthetization of a modulated MR pulse at the desired frequency offers great control over the signal, it also introduces complications when used in conjunction with the heterodyne receiver hardware as employed in most commercial MR scanners [102]. The resulting signal phase differences for every repetition, explained in Figure 3.7, lead to an image shift in the phase encoding direction in case of simple gradient echo images.

This behavior was alleviated by computationally shifting consecutive RF pulses by the phase expected from the receiver, essentially bringing each pulse in phase with the system's local oscillator (LO). This however, requires more memory on the M2i cards, as each phase-shifted pulse needs to be stored individually.

Trigger accuracy

The viability of the presented signal generator depends crucially on the availability of a high precision trigger signal. This is provided by the Siemens scanner through the possibility of creating highly stable trigger events inside an MR sequence (OscBit). This, however requires a modification of each sequence to be used. Instead, an alternative solution was sought that does not require any sequence programming, in light of the fact that the source code for many pre-installed sequences is not available and lacks appropriate trigger signals. The power amplifiers require an unblanking TTL signal prior to each pulse playback. High precision oscilloscope timing measurements at a sampling rate of 20 GHz revealed that this pulse was highly stable in the sub-picosecond range, and it was thus used to replace the software based trigger signal, making all sequence modifications obsolete. A required post-trigger delay of

223 μs was measured, and then programmed into the signal generator to match the pulse output to the internal delays of the Siemens system.

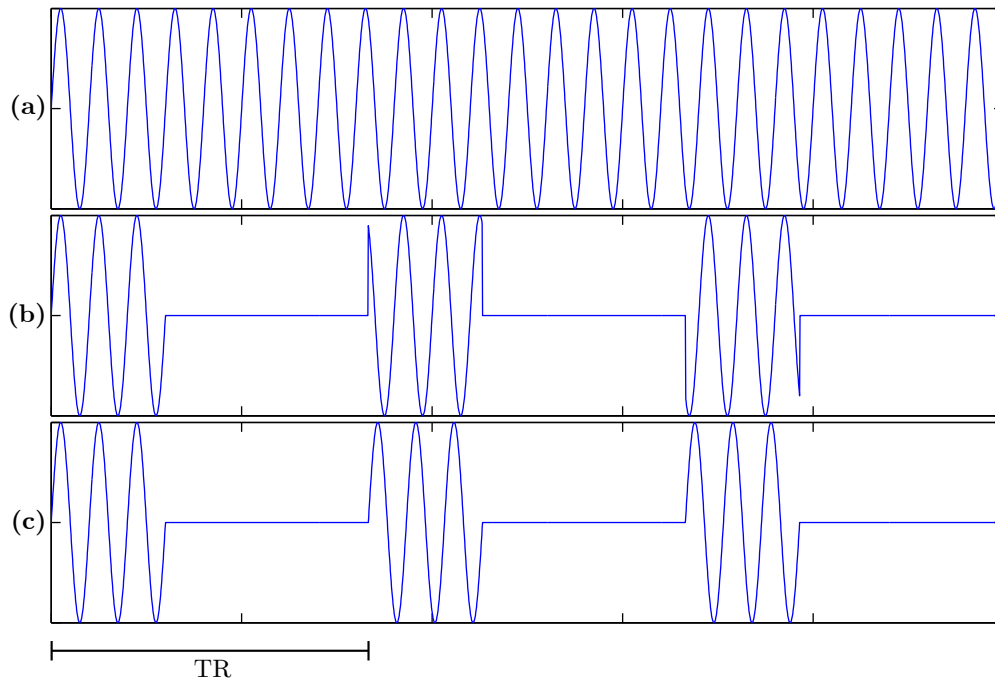


Figure 3.7: Side-by-side comparison of the MR pulse phase when using the vendor transmission hardware vs. the novel signal generator setup. A continuous sinusoidal signal corresponding to the system's local oscillator is shown in (a). This signal is set to the desired excitation frequency, and will be used as the carrier upon which the desired MR pulses will be modulated. Graph (b) shows three consecutive hard RF pulses derived from this signal, separated by a repetition time TR. Taken individually, each of these pulses visibly exhibits a different RF phase, as each pulse represents a section of the LO signal starting at non-integer multiples of the LO period. Pulses generated by the presented setup (c), however, exhibit the same phase for each pulse, as an identical signal is generated every time. The signal received from the spins exhibits a phase proportional to the excitation phase. In the vendor's RF concept the same LO reference signal (a) is used for generating the transmit and for demodulating the receive pulses. The phase offsets between pulses in (b) are thus compensated and the phases of the final signals used for image reconstruction are identical for each excitation. Conversely, this implies that the LO reference signal (a) cannot directly be used for demodulating receive signals which were excited using the phase-stable transmit pulses (c) since otherwise an unwanted signal phase increment would occur from excitation to excitation.

Sequence adjustments

Some advanced techniques require a manipulation of the transmit frequency or phase that need to be accounted for during reception. Notably, RF spoiling uses a different excitation phase for each repetition to prevent transverse magnetization coherences [103]. This phase is usually compensated during reception. As RF spoiling was not implemented in the signal generator, it had to be disabled in the sequence settings as well to prevent ghosting artifacts resulting from the application of receive phase shifts that were not applied during transmission.

All but the most basic MRI sequences require the application of switched gradient fields for spatial localization. These time-dependent magnetic fields induce eddy currents in the surrounding structures that are detrimental to data quality [104–106]. While eddy currents resembling linear gradient field distributions are compensated by pre-distorting the desired gradient waveforms (pre-emphasis), some of these eddy currents induce a homogeneous field that results in a B_0 shift. This time-dependent offset can be either compensated by a dedicated Z_0 coil, or, as performed on the Siemens system, by dynamically adjusting the carrier frequency. While the former method is completely transparent and requires no further consideration during reception, the latter necessitates a corresponding shift during reception. Hence, the B_0 compensation was deactivated, because required calibration data for an implementation of the B_0 compensation in pulse calculation was not available. Nevertheless, this did not result in visible image distortions or shifts, as the utilized sequences were not particularly susceptible to these effects.

Amplifier connection and input calibration

The channels one through eight were connected to the small signal input ports of the Analogic amplifiers (AN8135S8, Analogic Corp, Peabody, USA). In order to calibrate amplitudes of the system with respect to the original Siemens output, the small signal amplitudes of the output signals were measured for the Siemens system as well as the presented setup. At their maximum output amplitude, the signal generator voltage corresponds to RMS voltages at the coil plug of approximately 240-250 V. As these voltages are above the hardware limits for the utilized coils, no further amplification was necessary.

The remaining channels nine through twelve were connected to the additional Dressler PAs (LPPA 13040W, Dressler, Stolberg, Germany), which feature a comparable gain of approximately 75 dB. Since these amplifiers were part of a legacy Bruker MRI installation, calibration factors for the available power inside the scanner room were not available. However, as all required quantitative information for parallel transmission experiments is contained in the measured B_1 maps, an exact knowledge of the input voltage is not necessary. The calibration factors were roughly estimated from the amplifier gain and cable losses, resulting in approximately 300 V at the coil connection when the signal generator operated at maximum output amplitude.

Channel	1	2	3	4	5	6	7	8
Peak amplified voltage $/V_{\text{RMS}}$	242	244	257	239	246	257	258	260

Table 3.1: Amplified MR transmit voltages when driving the signal generator at maximum output amplitudes. These values can be used to directly relate a given numerical amplitude in the pulse design to a physically measurable voltage. The differences between the individual channels can be attributed to slight variations in DAC and bandpass filter performance, as well as slight variations between the eight power amplifier channels.

3.1.5 Pulse and sequence programming

Constructing the digital excitation pulses and programming the M2i cards for pulse sequence playback was done using Matlab. For all gradient echo (fast low angle shot, B_1 - and B_0 -Mapping sequences, a 2.5 ms windowed sinc shaped pulse was used, similar to the default pulse played back in the respective sequences by the Siemens RF hardware. Pulse- and sequence setup for these sequences was done according to the following process:

1. Definition of the sequence and pulse parameters, mimicking the sequence timing defined on the Siemens console
2. Calculation of the pulse train
3. Channel multiplexing
4. Card initialization and pulse data transfer
5. Sequence start on the Siemens console

The defined sequence parameters (excitation frequency, TR, resolution and individual channel amplitudes and phases), were fed into a pulse train calculation function, which is unique to each sequence. There, the complete train of required pulses was shaped from a sinusoidal base signal, with appropriate amplitude and phase factors as well as the required phase offset between each repetition, derived from the base frequency and TR. While this calculation was done in full floating point accuracy, the waveforms were then converted to 16-Bit signed integers, as required by the DACs. Each M2i.7021 is responsible for pulse playback on four channels. Due to the internal memory organization, the four waveforms for each card need to be written in an interleaved manner in order to be played out simultaneously. With the samples notated as $S_{m,n}$, where m corresponds to the channel number and n the sample number with N total samples over the whole pulse train, a composite waveform is created as $[S_{1,1}; S_{2,1}; S_{3,1}; S_{4,1} \dots S_{4,N}]$. The interleaved pulse data is then transferred to the cards, and the memory segmented into blocks corresponding to the pulse lengths. The card is then set into a playback mode, where one memory block is played back upon each trigger detection.

The FLASH sequence requires the playback of the same pulse with a phase shift based on the sequence timing (see Fig. 3.7) upon each trigger event. The utilized

transmit SENSE sequence uses the same timing with the spatially selective pulses replacing the non-selective pulses of the FLASH sequence, hence requiring no further sequence programming on the home-built pTx system. Similarly, the B_0 -maps were calculated using two FLASH images with a different echo time to retrieve the local off-resonance frequency [107]. B_1 -mapping was achieved using a modified preparation-pulse technique [108, 109] with a fast readout. Hence, the system was programmed to generate a non-selective preparation pulse upon the first trigger event, followed by a readout pulse upon each of the following triggers.

3.1.6 Assembled setup

The complete signal generator hardware is shown in Figure 3.8.

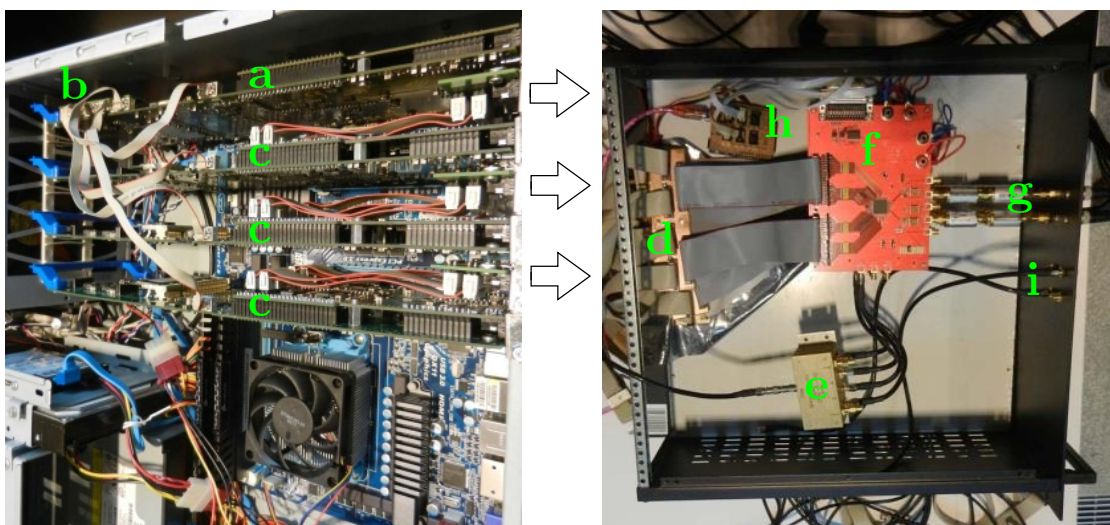


Figure 3.8: Depiction of the complete setup inside the 19" enclosures, with the control PC (left) and D/A conversion unit (right). The M2i.7020 (a) contains the StarHub (b), and receives the external clock and trigger signals, which are distributed to the M2i.7021 cards (c). These cards generate the digital pulse waveforms, and output them along with clock- and trigger signals via ribbon cables. These cables connect to breakout boards (d), which route the pulse signals to the six stacked DACs (f), and offer SMA connectors for the clock and trigger I/O lines. The clock signal is routed to a 1:6 power splitter (e), which distributes the 44 MHz clocking signal to the DACs. The analog DAC output is band-pass filtered (g) to remove all spectral components besides the desired 123.2 MHz MR pulse signal, which is output via twelve SMA jacks. The Arduino microcontroller (h) can program the DAC setup registers and is connected to the control PC via USB. Access to trigger in- and output is provided by two additional SMA connectors (i), which are routed to the M2i.7020 card.

During the measurements, the system was placed in the MR scanner tech room as shown in Figure 3.9.

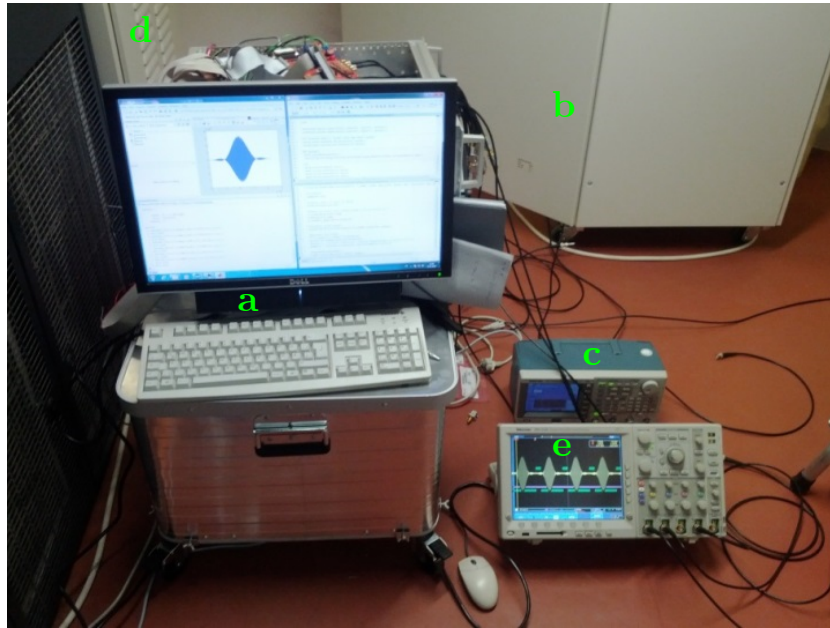


Figure 3.9: The home-built 12-channel pTx system connected to the Siemens MR scanner. The control PC and D/A unit (a) are set up close to all required interfacing components. The power amplifier (d) is connected to eight of the output channels, and one of its unblanking TTL inputs is tapped using a T-piece to extract the trigger signal. The MPCU cabinet (b) allows access to the 10 MHz clocking signal, which is converted to a usable square wave signal by the Waveform generator (c). The connected oscilloscope (e) was used for testing and calibration measurements, and shows a continuous train of generated sinc pulses.

3.2 Measurements

3.2.1 Pulse output fidelity

In order to evaluate the spectral fidelity of the generated signals, a 2.5 ms block pulse was recorded using an oscilloscope (Tektronix DPO 4104) and subjected to a power spectral analysis shown in Figure 3.10. In order to reduce spectral sidebands potentially masking any imperfections, a Blackman-Harris window was applied to the block pulse, which features a spectral side lobe suppression of more than 90 dB. Hence, any spurious signals appearing beside the main lobe above this level can be attributed to imperfections in the generated pulse.

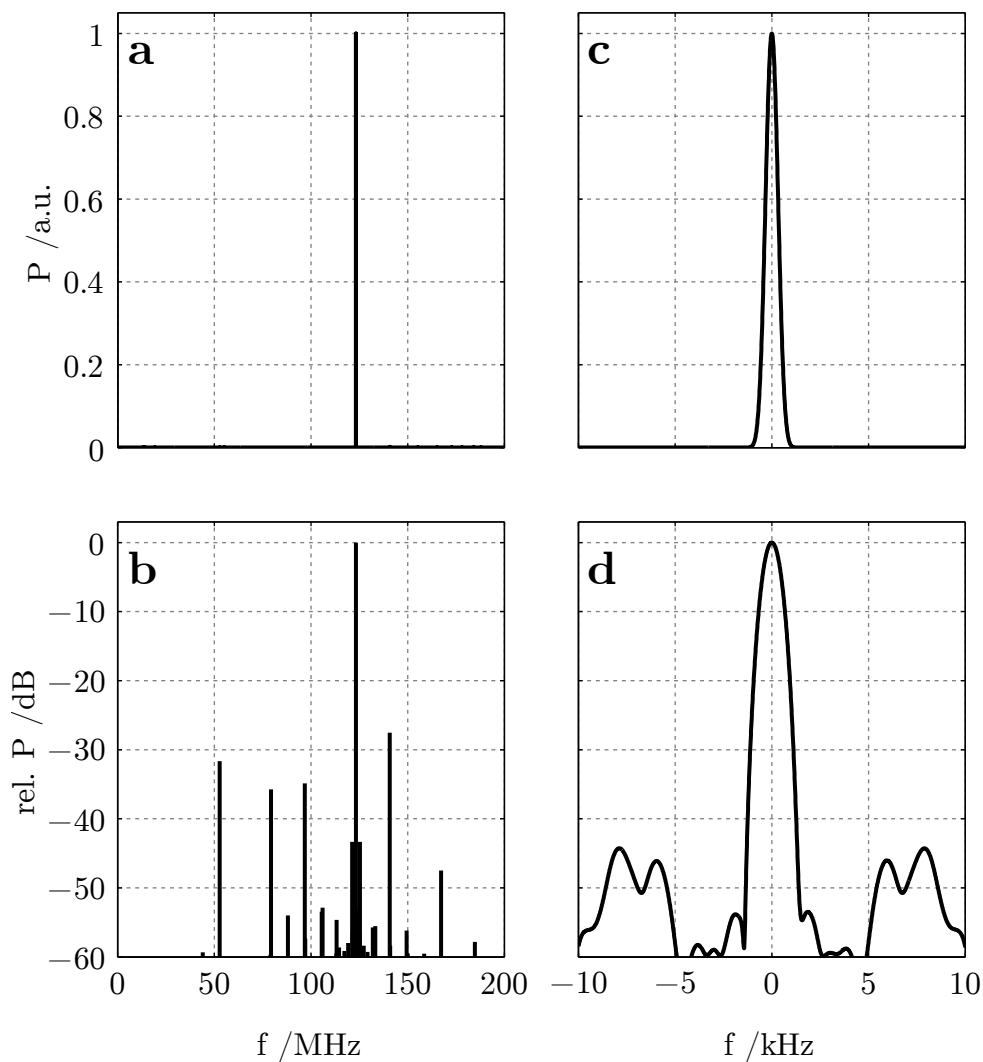


Figure 3.10: Power spectrum analysis of the windowed block pulse. On a linear scale (a), only the desired signal at 123.2 MHz is visible. At a logarithmic level (b), multiple spurious signals can be seen. The closest significant sidebands on this scale appear at ± 2 MHz from the center frequency, albeit with a level below -43 dB. The strongest spurious signal is found at 140.8 MHz with a power of -28 dB. The fundamental output frequency of the DAC at 52.8 MHz is attenuated below -30 dB. At a bandwidth of 20 kHz around the center frequency, no spurious signals are apparent at a linear scale (c). Here, the closest sidebands appear between 5 to 10 kHz, with amplitudes below -44 dB (d).

3.2.2 8-channel measurements

Prior to the extension to twelve channels, the viability of the proposed setup was tested through eight channel measurements, where the complete Siemens pTx system was replaced. Measurements were performed with an eight-channel degenerate

birdcage [69] type head coil filled with a cylindrical agarose phantom, shown in Figure 3.11.

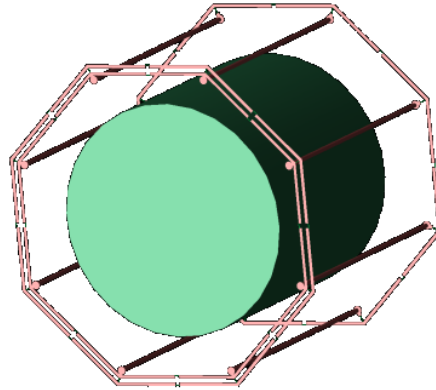


Figure 3.11: CAD model of the eight-channel coil used for the initial parallel transmission experiments.

Calibration measurements

In order to perform transmit SENSE experiments, B_0 and B_1 -maps were acquired with the system, which are shown in Figures 3.12 and 3.13.

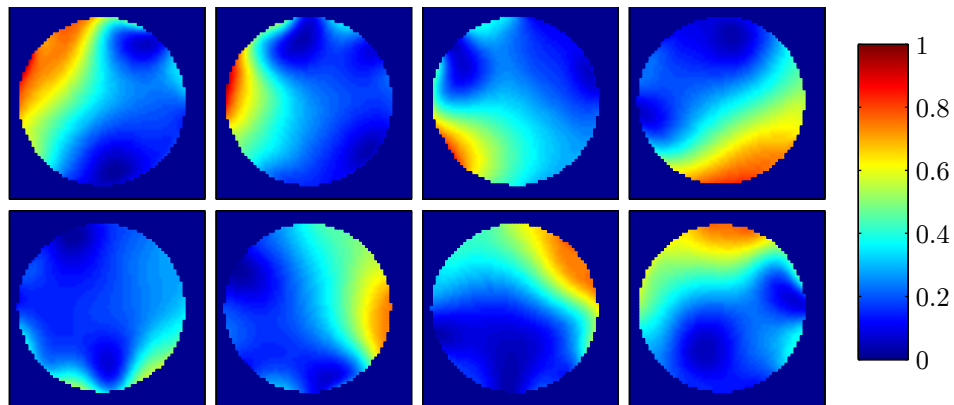


Figure 3.12: Normalized B_1 maps of the 8-channel coil in the central axial slice, acquired using the home-built pTx system for transmission. No ghosting artifacts or image shifts are visible.

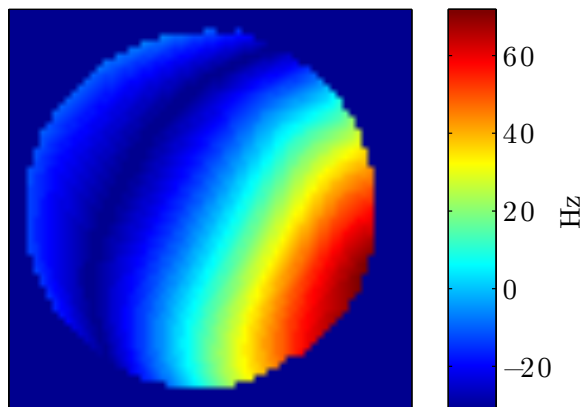


Figure 3.13: B_0 map of the central axial slice. The relatively strong off-resonance in the lower right region is explained by the Siemens B_0 -shimming routine only utilizing a single channel for excitation, resulting in regions that do not contribute any signal and are thus not considered in the B_0 -shim algorithm.

Static B_1 shimming

Based on the center phase of the measured B_1 maps, static RF shimming was performed to excite the first three canonical Birdcage modes, corresponding to nearest-neighbor phase differences of 45° , 90° and 135° , respectively.

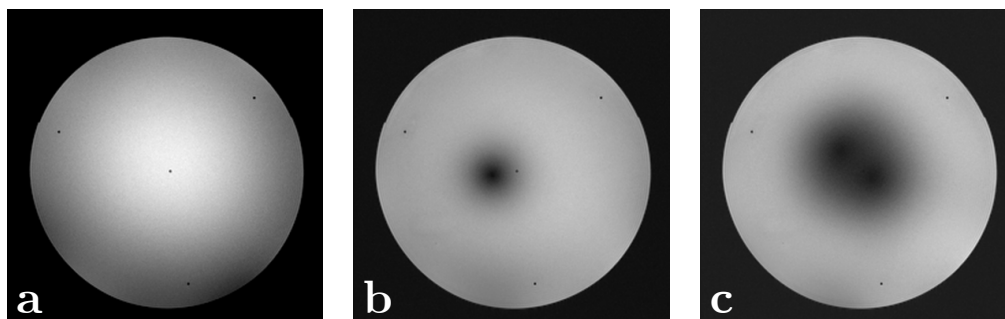


Figure 3.14: Statically B_1 -shimmed FLASH images of the first (a), second (b) and third (c) Birdcage mode of the coil. The image parameters are $TR = 50$ ms and $TE = 2.5$ ms.

Transmit SENSE

Spatially selective pattern excitation images achieved with the 8-channel coil are shown in Figure 3.15.



Figure 3.15: Transmit SENSE 2D spatially selective excitations using the signal generator. Multiple varying shapes were excited, including an off-center rectangle (a), the PTB logo (b), as well as images of Otto von Guericke and Albert Einstein. All patterns were designed on a 64^2 field of excitation with 4x acceleration, resulting in 6.72 ms pulses; with the sequence parameters being $TR=100$ ms and $TE=5$ ms. Apodization for ringing suppression was achieved by downsampling all excitation shapes from a higher resolution image prior to pulse calculation, leading to smoothed edges.

3.2.3 (Almost) 12-channel measurements

An octahedral coil array, which will subsequently be described in-depth in Chapter 5, was utilized for parallel transmission experiments with twelve channels. However, due to an irreparable hardware defect on one of the M2i.7020 cards, the system was reduced to eleven channels for the final measurements. Hence, one channel was disconnected and terminated with a 50Ω resistance.

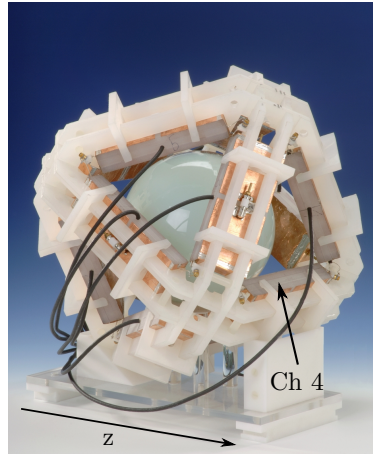


Figure 3.16: Photo of the octahedral coil, with the deactivated channel shown.

Transmit SENSE

The most characteristic feature of the octahedral coil is its high symmetry where all three spatial axes exhibit significant sensitivity variations. This allows accelerated

transmission or acquisition in all directions and not just in the transversal x,y plane. Even with one defunct channel this ability is largely maintained, as demonstrated in Fig. 3.17, where selective excitation in the axial and coronal plane of the phantom is shown.

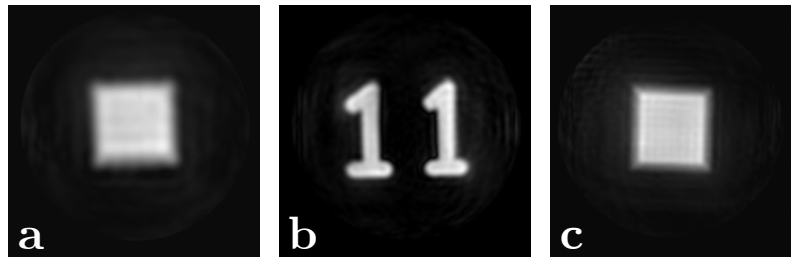


Figure 3.17: Transmit SENSE 2D spatially selective excitations using the signal generator with 11 channels active. A rectangular excitation in the axial plane is shown in (a), the number 11 in an axial plane in (b), and (c) showing a rectangular pattern in the coronal plane. Pattern (a) was designed on a 32^2 field of excitation, whereas patterns (b) and (c) were designed on a 64^2 field of excitation. The sequence parameters were $TR=100$ ms and $TE=5$ ms.

A detailed comparison of the achieved excitation fidelity with the defined and simulated patterns is shown in Figure 3.18.

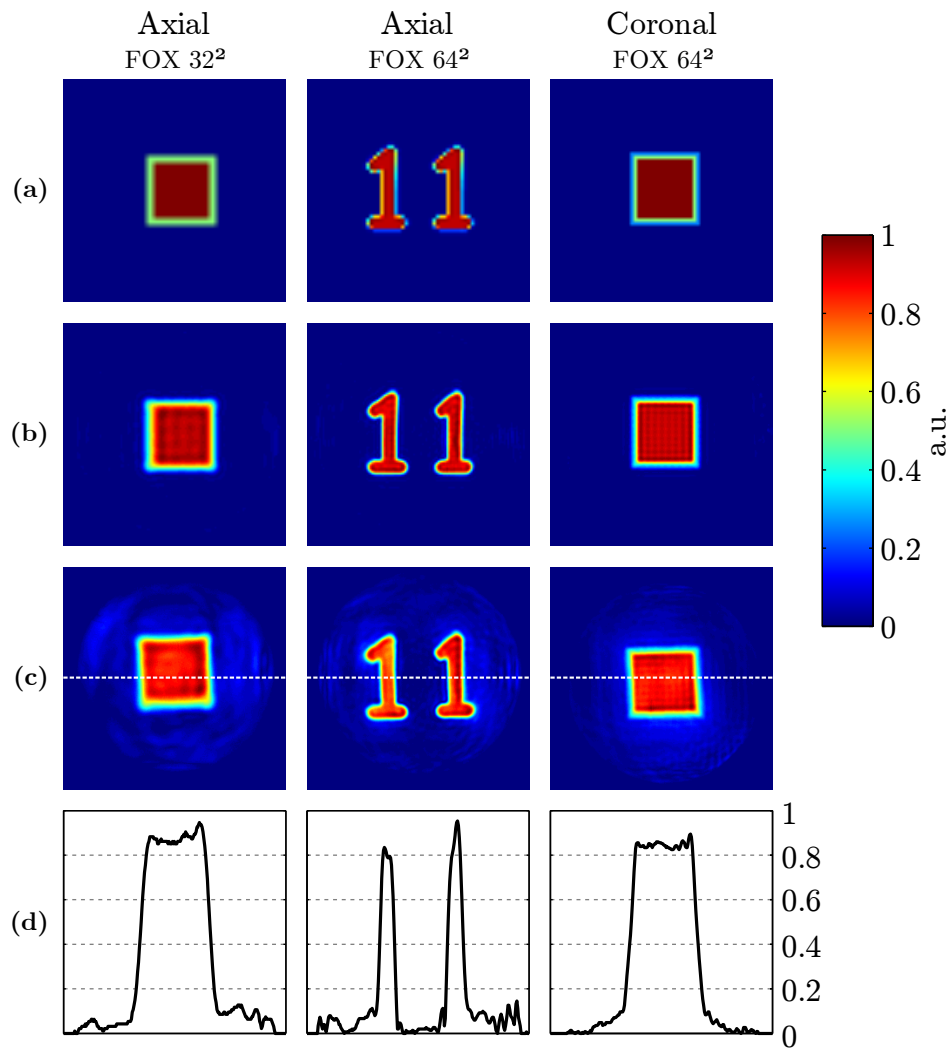


Figure 3.18: Detailed comparison of the previously shown measured selective excitation patterns with the defined and simulated shapes. The top three rows show the defined pattern (a), Bloch simulation result (b) and measurement result (c), respectively. The bottom row shows (d) measured signal profiles taken along the dashed lines shown in (c).

3.3 Discussion

The designed system features a very small footprint of two 4HE 19" cases. It can be integrated with the MR scanner in a straightforward manner, relying only on a reference clock and trigger signal. It is thus capable of working across vendor platforms, and a preliminary design was previously utilized on a Bruker MedSpec 30/100 MRI scanner [38, 101]. While the designed setup only used twelve channels due to coil- and amplifier limitations, up to 5 M2i.7021 cards could be employed in a single control computer, resulting in 20 channels. Multiple of these setups could then

be linked via an additional StarHub for cross-computer synchronization, allowing for even larger channel numbers. The flexible frequency synthetization process would allow operation at other field strengths, or even X-Nucleus parallel transmission, given the availability of power amplifiers in the desired frequency range.

The results unanimously show, that the presented setup is capable of producing synchronized pulses of the required fidelity. The spectral quality analyzed in Figure 3.10 shows a strong suppression of potentially detrimental sidelobes. All required sequences for parallel transmission applications were shown to be properly functioning, including B_0 and B_1 mapping, statically B_1 shimmed FLASH imaging as well as transmit SENSE excitation. No ghosting, blurring or image shift artifacts are visible in the images, indicating a stable output frequency and consistent trigger operation.

The measured transmit SENSE patterns show a good agreement compared to the simulation. Nevertheless, a slight rotation artifact is visible in the images, especially in the square patterns. This is most likely due to a slight miscalibration in the post-trigger delay of the signal generator, leading to a minor offset between the pulse and the gradients [93]. The background signal in regions outside the desired excitation shape remains well below 10% in most parts, which is similar to results shown by e.g. Ullmann et al. [19, 93]. The remaining difference between the Bloch simulation result and measurement can be attributed to the delay mismatch, as well as inaccuracies in the field maps for B_0 and B_1 , which are not an intrinsic problem of the described setup, but rather systematic errors stemming from the utilized MR sequences.

The required deactivation of the B_0 -compensation as described in Sec. 3.1.4 led to no visible artifacts for the presented measurements. However, sequences with stronger gradients or higher gradient slew-rates might be impacted adversely. This can only be circumvented by implementing the required transmission frequency shifts in the home-built pTx system. Similarly, RF spoiling could be implemented by replicating the expected RF phase shifts of the Siemens console. These two issues are a direct consequence of the presented setup's lack of a continuously running reference clock oscillating close to the required Larmor frequency.

The original eight channels were supervised by the integrated Siemens power and SAR monitoring unit. However, the additional amplifiers were not connected to a similar monitoring interface, making the system not appropriate for *in vivo* use in its current state.

3.4 Conclusion

The presented multichannel signal generator approach for MRI parallel transmission has been shown to operate satisfactorily, as was demonstrated in bench and MR imaging experiments. It allows to go beyond the vendor-provided number of transmit

channels in order to benefit from the additional degrees of freedom provided by the extra channels. It has a small footprint, is relatively low in cost (1500€/channel), and can be integrated with any MRI system, provided adequate clock and trigger signals are available. The system can in principle generate arbitrary frequencies limited only by the maximum DAC sampling rate, and could be extended to 7T proton imaging at 300 MHz by replacing the DAC. An equal number of power amplifiers is, of course, required for its application. However, the presented setup could be utilized in conjunction with on-coil power amplifiers or current sources [110, 111] in order to construct a many-element transmit array.

4 The electromagnetic power balance of an RF transmit coil array

With the previous chapter detailing the synthetization of coherent multi-channel signals, the focus is now shifted further down the RF chain. As described in section 2.5.3, pulse powers in the kW range are required for spin excitation. Only a negligible amount of this power is actually transferred to the spin system, with the majority being absorbed in the RF coil and patient through ohmic heating. For multi-channel coil arrays, the distribution of the input power between different loss mechanisms depends on the excitation conditions imposed on the array. One set of driving amplitudes and phases could result in most of the input power being deposited in the patient, whereas another set leads to almost all power being deposited inside a decoupling circuit or being radiated into the far field. This behavior has implications on patient safety, component damage protection and overall coil performance. Current parallel transmission systems often suffer from a lack of available power, and hence minimizing losses is a priority for a coil designer. Knowing which losses have the strongest impact is invaluable for improving a coil array's design. On one hand, this knowledge can show the best avenue for increasing performance, while on the other hand strategies that only seem to improve performance based on other metrics like decoupling can be identified and discarded. A merely 5% performance improvement might not be worth the additional complexities that are required.

This chapter will introduce a framework to estimate the loss behavior of RF transmit coil arrays based on electromagnetic simulations. It is aimed at assisting in reaching optimum design decisions, and understanding the interactions of different loss mechanisms on a fundamental level.

The sections 4.1 - 4.6 were previously published by the author in reference [43]. Hence, they are cited verbatim from the introduction and theory sections. Only section 4.7 on coupling effects is modified and extended from the published article.

4.1 Introduction

The power balance, i.e. the breakdown of all coil losses by loss mechanism, is an important metric for assessing radiofrequency (RF) coil efficiency. While power deposition inside a conducting sample cannot be avoided due to the concomitant electric fields linked to the desired excitation RF field (B_1), additional losses occurring in the coil itself can be minimized by prudent design choices. To quantify the contributions of coil and sample losses, the power efficiency, i.e. the fraction of the input power deposited in the lossy sample, is used as a figure of merit for single coils [3, 112].

Multiple coil elements can be combined to form phased arrays for reception [14] as well as transmission [94] in order to increase receive sensitivity and excitation fidelity, respectively. However, inductive, capacitive and resistive interactions between the individual coil elements incur additional losses, leading to increased noise, decreased transmission efficiency and less distinct coil sensitivity profiles. A variety of methods exists to reduce coil coupling effects in transmit arrays, ranging from coil overlap [14], shared L/C elements [78], transformers [26] and resonant circuit elements [28] to active techniques involving modified transmitter hardware [110, 111, 113].

At ultra-high field strength (≥ 7 T), coils employing radiative power transfer into the subject have been shown to yield advantageous B_1 distributions [27], and traveling-wave MRI even completely relies on radio wave propagation at high frequencies [73, 114]. However, power loss due to unwanted far field radiation is increasing with frequency as well ([115, , and references therein]). While electromagnetic energy leaving the magnet bore is, of course, almost perfectly contained by the scanner's Faraday cage and ultimately dissipated in the sample and other lossy structures inside the scanner room, its interference pattern with the desired coil fields is hardly predictable; and radiative losses are routinely mitigated through the use of metallic coil shielding structures [116].

The introduction of shields and additional decoupling components, however, can introduce further losses, and it is of high interest to the coil designer to weigh their benefits against the costs. Apart from low loss requirements, component voltage and power limits affect design choices as well and have to be carefully examined regarding their impact on coil performance. According to manufacturer datasheets, high-voltage rated capacitors often exhibit far lower Q factors compared to capacitors with lower working voltages, but conversely feature lower maximum current limits due to their increased losses.

Ideally, power is mainly dissipated in the subject. This power deposition, however, critically depends on the exact superposition of the individual coil elements' electric fields, and the assumption of a lossless coil has been shown to yield significantly different specific absorption rate (SAR) estimates as compared to more realistic models [117]. The absence of specific loss mechanisms will invariably lead to a

different redistribution of the input power onto the remaining losses, impacting local and global SAR estimates and thus apparent coil performance.

Electromagnetic simulations are an important tool to evaluate coil design choices and, additionally, are obligatory for SAR evaluation of multi-channel coils used in parallel transmission [80]. However, computational approaches such as the finite-difference time-domain (FDTD) method [81] often do not encompass the full problem space. Instead of including the Faraday cage, free-space boundary conditions are being used [118, 119], thus introducing a radiated power component that needs to be accounted for when estimating coil efficiency and SAR [115, 120]. This simplification is useful for multiple reasons. From a purely practical standpoint, the inclusion of the cage greatly raises the memory requirements for the simulation. Additionally, the simulation time will increase, as it is proportional to the Q-factor of the modeled system, and the closed scanner room can be regarded as a high-Q cavity. Finally, the knowledge about radiated power leaving the bore is invaluable to the coil designer, as it allows to quantify and compare the efficacy of different radiation shielding measures.

Increasingly complex coil setups have spurred the development of sophisticated simulation approaches [85, 86, 121], where data is often exchanged between different commercial simulation programs and in-house developed post-processing tools. While this allows a very flexible and powerful analysis of coil behavior, it is imperative to ensure the integrity of the results, especially if patient safety is directly affected. Frequently, B_1 mapping and temperature measurements are used for simulation validation [108]; however it is desirable to additionally verify a particular coil simulation in its entirety based on a single metric. Energy conservation, expressed for electromagnetic fields in the Poynting theorem, is a prime candidate for this purpose. Trivially, the power balance can be calculated after superimposing the single-channel fields. However, this approach is tedious, as it is computationally intensive in practice and only allows examination of a limited number of driving modes. As yet, no comprehensive scheme adapted to the unique loss behavior of transmit arrays has been published. It is well known, on the other hand, that the power correlation matrix formalism can greatly simplify the estimation of power deposited inside lossy materials, and it is routinely used for local and global SAR estimation in simulation as well as in situ [22, 32, 122]. Starting out from our initial investigations [42], the aim of this paper is to extend this formalism by deriving a power correlation matrix for each term contributing to the total power balance. This will allow to address the aforementioned coil design and simulation issues by providing a framework for straightforward and consistent calculation of all loss terms, comparison of different array design approaches via their respective loss matrices, and integrity validation of electromagnetic field simulations in order to more accurately predict and evaluate transmit coil array behavior.

4.2 Poynting's Theorem

Conservation of electromagnetic energy is expressed in Poynting's theorem [123]. For time-harmonic fields, the real part of the theorem represents the power balance of the system, $-P_{\text{src}} = P_{\text{dis}} + P_{\text{rad}}$, equating the source power P_{src} in a volume V to the sum of the power dissipated inside, P_{dis} , and the power P_{rad} radiated through the volume's boundaries:

$$-\frac{1}{2} \iiint_V \text{Re}(\mathbf{J}^* \cdot \mathbf{E}) dv = \frac{1}{2} \iiint_V \sigma(\mathbf{r}) |\mathbf{E}|^2 dv + \frac{1}{2} \oint_{\partial V} \text{Re}(\mathbf{E} \times \mathbf{H}^*) d\vec{s}. \quad (4.1)$$

Here, \mathbf{E} , \mathbf{H} , \mathbf{J} and σ represent the spatially varying electric field, magnetic field, current density and conductivity, respectively, and the asterisk indicates complex conjugation.

Since the individual coils of an N-channel transmit array are driven by N discrete sources, the left-hand integral can be replaced by the sum $\frac{1}{2} \sum_{i=1}^N \text{Re}(I_i^* U_i)$ over the source voltages and currents U_i and I_i . Treating the system as purely linear, all fields, voltages and currents can be represented as linear combinations of their respective single-channel excitation values, e.g. $\mathbf{E} = \sum_{i=1}^N \alpha_i \mathbf{E}_i$, where α_i is a dimensionless complex scaling factor and \mathbf{E}_i represents the electric field generated by coil element i for a unit excitation. The scaling factors are commonly regarded as equivalent to driving voltages that are variable during an MR experiment, being updated in discrete intervals long enough to maintain the time-harmonic field behavior during each individual step. Eq.4.1 must necessarily hold for each of the discrete steps. In order to separate the static, i.e. geometry dependent, from dynamic, i.e. excitation dependent, contributions, it can be expressed in terms of quadratic forms $\mathbf{v}^H \mathbf{Q} \mathbf{v}$, with a static hermitian positive-semidefinite matrix \mathbf{Q} specific to each power term, \mathbf{v} constituting the time-dependent coil array driving voltage vector common to all quadratic forms, and superscript H denoting the conjugate transpose. Subsequently, these matrices will be derived, with a focus on separating contributions of different loss mechanisms.

4.3 Source power

Most commonly, transmit arrays are driven using a discrete power amplifier for each channel, with a fixed source impedance of $Z_0 = 50\Omega$, and the individual coil elements impedance-matched to Z_0 for maximum power transfer. When describing the power flow within an N-port network such as a coil array, three distinct notions of power are of interest. The forward power P_{fwd} denotes the power incident to the system, with a fraction P_{src} of this power being transmitted into the network, and the remainder P_{ref} reflected from it due to imperfect impedance match and coupling, eventually being absorbed in the power amplifier circulators. The power flow can be analyzed

in terms of normalized forward and reflected voltage wave vectors, \mathbf{a} and \mathbf{b} , which are related through the system's $N \times N$ scattering matrix \mathbf{S} via $\mathbf{b} = \mathbf{S}\mathbf{a}$ [79]. The source term in Eq.4.1 can be conveniently formulated in terms of \mathbf{S} . Power incident into the system is given by $P_{\text{fwd}} = \frac{1}{2} \mathbf{a}^H \mathbf{a}$. This can be expressed as a quadratic form of the driving voltage amplitude vector $\mathbf{v} = \sqrt{Z_0} \mathbf{a}$:

$$\begin{aligned} P_{\text{fwd}} &= \frac{1}{2} \mathbf{a}^H \mathbf{I}_N \mathbf{a} = \mathbf{v}^H \left(\frac{1}{2Z_0} \mathbf{I}_N \right) \mathbf{v} \\ &= \mathbf{v}^H \mathbf{Q}_{\text{fwd}} \mathbf{v}. \end{aligned} \quad (4.2)$$

With \mathbf{I}_N denoting the identity matrix of size N , the resulting forward power matrix \mathbf{Q}_{fwd} is thus purely diagonal.

Power that is reflected from the network due to mismatch or lost via inter-element coupling can be calculated from the reflected waves \mathbf{b} as $P_{\text{ref}} = \frac{1}{2} \mathbf{b}^H \mathbf{b}$, which can be rewritten in terms of the incident waves and the scattering matrix to yield the reflected power correlation matrix \mathbf{Q}_{ref} :

$$\begin{aligned} P_{\text{ref}} &= \frac{1}{2} \mathbf{a}^H (\mathbf{S}^H \mathbf{S}) \mathbf{a} = \mathbf{v}^H \left(\frac{1}{2Z_0} \mathbf{S}^H \mathbf{S} \right) \mathbf{v} \\ &= \mathbf{v}^H \mathbf{Q}_{\text{ref}} \mathbf{v}. \end{aligned} \quad (4.3)$$

By convention of Eq.4.1, source power is regarded as negative, while all loss terms are positive, thus defining total source power as $P_{\text{src}} = \mathbf{v}^H [- (\mathbf{Q}_{\text{fwd}} - \mathbf{Q}_{\text{ref}})] \mathbf{v}$.

The elements v_i of vector \mathbf{v} are voltages by dimension and related to the scaling factors α_i via $\alpha_i = v_i / \sqrt{2 \cdot Z_0 \cdot P_0}$, assuming a forward power equal to P_0 was used for the unit excitation of the single channel fields. To increase readability, the factor $\kappa = (2 \cdot Z_0 \cdot P_0)^{-1}$ is used throughout the following sections.

4.4 Dissipative losses

It is advantageous to categorize power dissipation into material and lumped element (e.g. capacitor, inductor, resistor, etc.) losses, as the discrete elements can be more easily treated via circuit theoretical methods. Accordingly, power dissipated inside a lumped element can be calculated using the voltage drop U across the element and the current I flowing through it via $P = \frac{1}{2} \text{Re}(UI^*)$. Arranging the voltages and currents of multiple lumped elements in column vectors \mathbf{u} and \mathbf{i} , the dissipated power is given by $P_{\text{imp}} = \frac{1}{2} \text{Re}(\mathbf{i}^H \mathbf{u})$. For an N channel coil, matrices \mathbf{U} and \mathbf{I} can be constructed, in which the N^{th} column contains the voltages or currents of each lumped component for a unit excitation of coil element N . The total power dissipated inside the discrete components for an excitation vector \mathbf{v} is

now $P_{\text{imp}} = \frac{\kappa}{2} \cdot \text{Re}(\mathbf{v}^H \mathbf{I}^H \mathbf{U} \mathbf{v})$, and taking the real part via addition of the complex conjugate leads to

$$\begin{aligned} P_{\text{imp}} &= \frac{\kappa}{4} \left[\mathbf{v}^H \mathbf{I}^H \mathbf{U} \mathbf{v} + (\mathbf{v}^H \mathbf{I}^H \mathbf{U} \mathbf{v})^H \right] \\ &= \mathbf{v}^H \left[\frac{\kappa}{4} (\mathbf{I}^H \mathbf{U} + \mathbf{U}^H \mathbf{I}) \right] \mathbf{v} \\ &= \mathbf{v}^H \mathbf{Q}_{\text{imp}} \mathbf{v}, \end{aligned} \quad (4.4)$$

with \mathbf{Q}_{imp} denoting the lumped element loss matrix. Multiple matrices \mathbf{U} and \mathbf{I} can be utilized to differentiate element groups, such as matching, tuning and decoupling components.

The power dissipated inside a conductive material via interfering electric fields generated by multiple sources can be expressed as a quadratic form as previously described [94, 124]

$$P_{\text{mat}} = \mathbf{v}^H \mathbf{Q}_{\text{mat}} \mathbf{v}. \quad (4.5)$$

The entries q_{ij} of the power correlation matrix \mathbf{Q}_{mat} are defined as

$$q_{ij} = \frac{\kappa}{2} \iiint_V \sigma \mathbf{E}_i^* \mathbf{E}_j dV, \quad (4.6)$$

with the indices ij denoting the coil element number. The diagonal entries of this matrix denote the power dissipation when driving a single channel only, whereas the off-diagonal entries provide a measure of electric field orthogonality and thus coil element interaction. Apart from a scaling factor, \mathbf{Q}_{mat} is identical to the noise resistance matrix of a receive coil array [14, 125]. Integrating only over the volume of a specific medium (e.g. coil substrate, load, etc.) will yield a matrix for losses inside this particular medium.

4.5 Radiative losses

A radiated power correlation matrix \mathbf{Q}_{rad} similar to the dissipated power correlation matrix in Eq.4.6 can be constructed from the single coil fields. Starting with

$$P_{\text{rad}} = \frac{1}{2} \text{Re}(\mathbf{v}^H \tilde{\mathbf{Q}}_{\text{rad}} \mathbf{v}), \quad (4.7)$$

where the elements \tilde{q}_{ij} of matrix $\tilde{\mathbf{Q}}_{\text{rad}}$ are defined as

$$\tilde{q}_{ij} = \kappa \oiint_{\partial V} (\mathbf{E}_j \times \mathbf{H}_i^*) d\vec{s}, \quad (4.8)$$

and again taking the real part yields

$$\begin{aligned} P_{\text{rad}} &= \mathbf{v}^H \left[\frac{1}{4} (\tilde{\mathbf{Q}}_{\text{rad}} + \tilde{\mathbf{Q}}_{\text{rad}}^H) \right] \mathbf{v} \\ &= \mathbf{v}^H \mathbf{Q}_{\text{rad}} \mathbf{v}. \end{aligned} \quad (4.9)$$

4.6 Power balance

Poynting's theorem can now be stated in terms of quadratic forms, leading to the matrix equality

$$\mathbf{Q}_{\text{fwd}} = \mathbf{Q}_{\text{ref}} + \mathbf{Q}_{\text{imp}} + \mathbf{Q}_{\text{mat}} + \mathbf{Q}_{\text{rad}}. \quad (4.10)$$

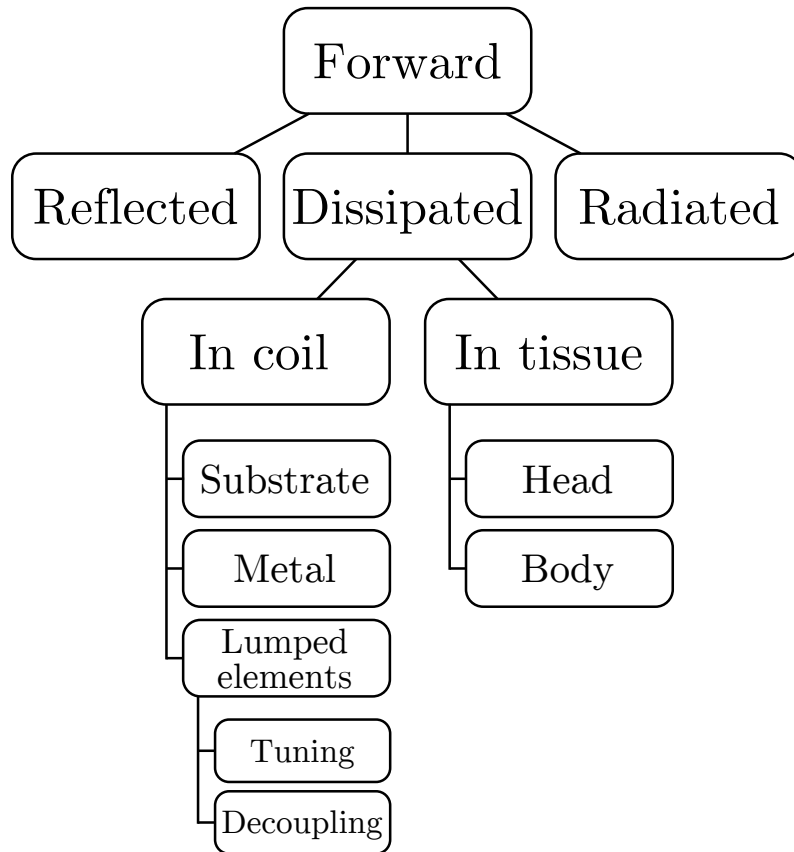


Figure 4.1: Branching diagram depicting the separation of the fundamental loss mechanisms into multiple subsets. Each subset can be represented by an individual loss matrix and further subdivided if a more differentiated loss analysis is desired.

The individual matrices can be analyzed by established mathematical tools, such as Eigendecomposition, which is routinely applied to investigate the quadratic forms

appearing in (local) SAR calculations [32] or the evaluation of phased array SNR [125, 126]. Eigenvectors form a basis where the power correlation matrices are diagonal; physically they represent non-interacting modes [69, 125]. The corresponding Eigenvalues define the losses occurring when exciting the Eigenmodes. For a vector \mathbf{v} of unit norm, the range of a quadratic form $\mathbf{v}^H \mathbf{Q} \mathbf{v}$ is limited by the largest and smallest Eigenvalues of the matrix \mathbf{Q} . Consequently, these values can be used to find the maximum and minimum possible loss contributions pertaining to an arbitrary power correlation matrix, and thus help in identifying major loss contributions. A visualization of a possible practical breakdown of these loss mechanisms into specific subsets is provided in Fig. 4.1.

Potential violations of the equality can be utilized to assess the integrity of a given multi-channel EM coil simulation result. For this purpose, an additional matrix \mathbf{Q}_ϵ is introduced to the right-hand side, constituting the error matrix required to balance the equation. The by magnitude largest Eigenvalue of \mathbf{Q}_ϵ corresponds to the maximum power imbalance that might occur for this simulation. As energy is conserved in EM simulations [127], this matrix is expected to be negligible.

4.7 Coupling effects

Based on Eq. 4.10, the interplay between losses and coil coupling can be investigated on a theoretical level. As an example, a perfectly matched, non radiating, symmetric two-channel coil array loaded with a lossy sample, but without any intrinsic losses (e.g. made of perfect conductors and lossless capacitors) is assumed. Hence, the power balance of this coil can be written as $\mathbf{Q}_{\text{fwd}} = \mathbf{Q}_{\text{ref}} + \mathbf{Q}_{\text{mat}}$. Furthermore, it is presumed that the two coil channels produce non-orthogonal electric fields, resulting in non-vanishing off-diagonal entries in \mathbf{Q}_{mat} . The sum $\mathbf{Q}_{\text{ref}} + \mathbf{Q}_{\text{mat}}$ needs to result in a scaled identity matrix, and it can be concluded, that \mathbf{Q}_{ref} cannot vanish as it needs to contain non-zero elements to balance this equation. Hence, coils exhibiting resistive interactions via non-orthogonal electric fields inside a lossy medium will necessarily be coupled.

By some added decoupling mechanism, all coil interactions are eliminated, i.e. $\mathbf{Q}_{\text{ref}} = \mathbf{0}$. It is obvious that the resulting power balance with perfect decoupling, i.e. $\mathbf{Q}_{\text{fwd}} = \mathbf{Q}_{\text{mat}}$, cannot be satisfied. For a unit forward power, it resolves to

$$\begin{bmatrix} 1 & 0 \\ 0 & 1 \end{bmatrix} \neq \begin{bmatrix} 1 & k \\ k & 1 \end{bmatrix}, \quad (4.11)$$

with $|k| \leq 1$. This equation is clearly wrong for any non-zero k , i.e. for the assumed coils with non-orthogonal electric fields. Independent of its physical implementation, the structure providing the perfect decoupling between the two channels needs to be constructed of lossy components, and thus add an additional matrix term, i.e.

$\mathbf{Q}_{\text{fwd}} = \mathbf{Q}_{\text{mat}} + \mathbf{Q}_{\text{imp}}$, to the power balance. The naïve choice of

$$\begin{bmatrix} 1 & 0 \\ 0 & 1 \end{bmatrix} = \begin{bmatrix} 1 & k \\ k & 1 \end{bmatrix} + \begin{bmatrix} 0 & -k \\ -k & 0 \end{bmatrix} \quad (4.12)$$

is impossible, as the added matrix is not positive-semidefinite and thus cannot be physically realized by a passive linear component. For the simple two-channel case, the requirement for positive-semidefiniteness is, that the off diagonal entries need to be smaller or equal by magnitude compared to the diagonal entries:

$$\begin{bmatrix} 1 & 0 \\ 0 & 1 \end{bmatrix} \neq \begin{bmatrix} 1 & k \\ k & 1 \end{bmatrix} + \begin{bmatrix} k & -k \\ -k & k \end{bmatrix}. \quad (4.13)$$

This equality is now clearly violated for the diagonal entries. It is, however, possible to construct a solution by introducing additional factors into the equation. A valid power balance is given by

$$\begin{bmatrix} 1 & 0 \\ 0 & 1 \end{bmatrix} = \alpha \begin{bmatrix} 1 & k \\ k & 1 \end{bmatrix} + \beta \begin{bmatrix} 1 & -1 \\ -1 & 1 \end{bmatrix}, \quad (4.14)$$

assuming that the conditions

$$\alpha = \frac{1}{1 + |k|} \quad \text{and} \quad \beta = \frac{k}{1 + |k|} \quad (4.15)$$

are met. The constant α can be regarded as an attenuation factor, since $0 \leq \alpha \leq 1$. Hence, in order to achieve the desired perfect decoupling, power deposition in the sample is attenuated, which directly translates to a reduced B_1^+ for unit forward power, as some fractions of the power are instead absorbed in the necessarily lossy decoupling structures. A close examination of some practical decoupling structures [28] reveals, that these theoretical considerations exactly mirror their behavior.

This intrinsic relation between coupling and losses was previously noted by Hoult [113] for the case of receive arrays, where he ascribed an increase in noise and noise correlation to the use of resistive coupling compensation bridges. This, however, is only partly true. With noise clearly increasing due to the added lossy elements, noise correlation is vanishing as long as $\mathbf{Q}_{\text{ref}} = \mathbf{0}$ [128], which is known as Bosma's theorem, which will be invoked again in the upcoming numerical coil analysis section 5.2.2.

In a practical setting, all decoupling networks will inevitably introduce some amount of loss. The described limitation is, however, fundamental in nature, and defines a theoretical limit on achievable decoupling with lossless components. This limitation only pertains to the resistive part of mutual array element interactions, thus coils exhibiting only reactive coupling are not affected, and "perfect" decoupling is possible without additional losses required by conservation of power.

A first application of these basic considerations found a perfect agreement with full analytical solutions in a 2-channel case [129].

5 Numerical characterization of the 12-channel octahedral coil array

With the loss analysis methodology introduced in the previous chapter, it shall now be applied in the context of a comprehensive electromagnetic simulation of an RF coil array, namely the octahedral setup previously used for parallel transmission experiments in chapter 3.

The octahedral coil array was initially conceived and built by Thomas Riemer and Evgeniya Kirilina [41]. The design goals for the array were to enable accelerated imaging and excitation in arbitrary slice orientations by providing reasonably distinct coil sensitivity distributions not only in the transversal xy plane but throughout all orientations. A secondary expectation was a simplified decoupling procedure due to the strong symmetry of the coil. While some of these goals were met, such as accelerated imaging in all three slice directions [41] and transmit SENSE in multiple orientations as presented in this work, some detrimental properties of the coil only became apparent after construction. Firstly, decoupling was found to be significantly impacted upon the introduction of a load, and distinct areas of reduced coil sensitivity are apparent in the final images.

One of the major benefits of electromagnetic simulations for MRI coils is the possibility to identify potential performance bottlenecks before construction, and thus speed up the coil design process. While a significant amount of intuitive and theoretical understanding of MRI coils went into the inception of the octahedral coil array, most of the advanced numerical techniques required for an accurate numerical coil analysis were not yet available to confirm the assumptions. This chapter presents a post-hoc analysis of the array based on extensive electromagnetic simulations. The power balance formalism introduced in the previous chapter will be used in conjunction with established numerical coil analysis techniques to gain a complete understanding of the coil's behavior. Additionally, the loss analysis will be extended from the described transmit-only case to also incorporate a noise source analysis for reception.

Following the analysis of a single element, the full array behavior is characterized, with a focus on identifying the most dominant loss mechanisms and thus expected performance bottlenecks. In addition to a full SNR and noise source analysis, an Eigenmode approach is utilized in order to characterize the coil transmit sensitivity patterns and identify regions with suboptimal field coverage. Finally, the perfor-

mance for accelerated transmit SENSE spatially selective excitation in multiple slice directions is evaluated.

5.1 Coil Setup

5.1.1 Current sheet antennas

The basic building block of the array is the current sheet antenna (CSA) [130, 131]. It is constructed of a copper sheet wrapped around the surface of a cuboid with open sides, with a small gap on top to accommodate a tuning capacitor C_T . Matching to 50Ω is achieved with a so-called gamma-feed, which connects the source through a small wire loop and a series matching capacitor C_M to the inside of the copper sheet. A depiction of a single CSA with all components is shown in Fig. 5.1.

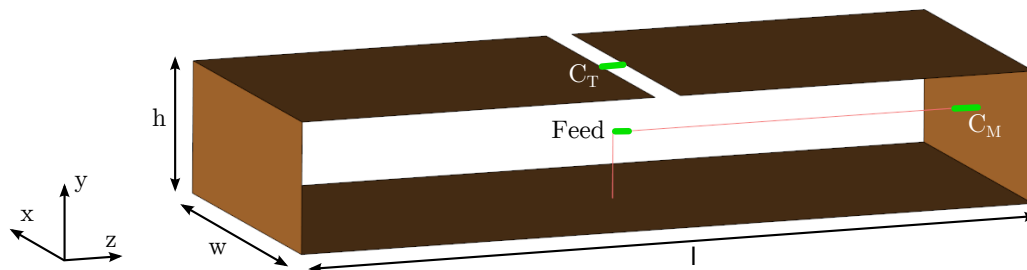


Figure 5.1: Depiction of a current sheet antenna as utilized in the octahedral array with dimensions $l \times w \times h = 173 \times 70 \times 30$ mm. The locations of the tune- and match capacitors as well as the feed connection are shown in green.

5.1.2 Array design

The coil array consists of twelve individual current sheet elements arranged on the edges of an octahedron, and is depicted in Fig. 5.2. Nearest-neighbor coils are interconnected with capacitors C_D to enable decoupling of the array.

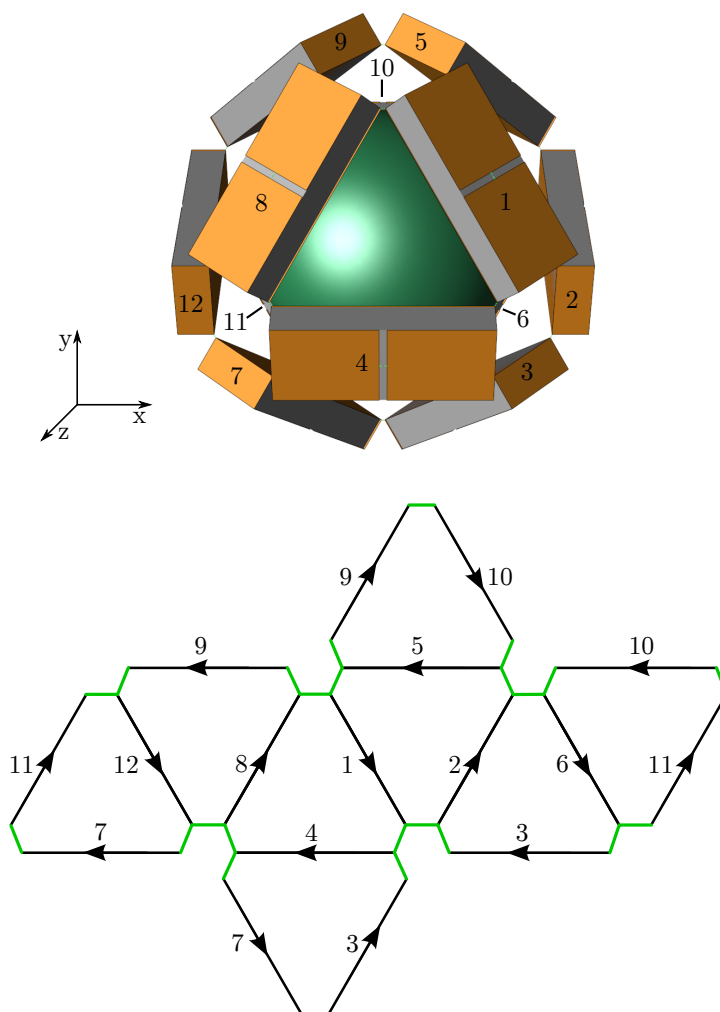


Figure 5.2: Model of the complete octahedral coil array with marked channel numberings (top), and a planar net representation of the octahedron (bottom). The arrows depict the current flow direction when driven with zero phase, and connections via the decoupling capacitances are indicated in green. The orientation of the coil is shown as seen looking into the magnet bore. As per the usual NMR convention, the adapted cartesian coordinate system is right-handed. Consequently, the x-axis is oriented from left to right, the y-axis from bottom to top and the z axis from back to front.

5.2 Coil Analysis Methodology

5.2.1 Electromagnetic simulations

Electromagnetic simulations were performed to gain insight into the behavior and performance of the coil array. Specifically, three distinct scenarios were investigated:

1. Single coil behavior
2. Insight into the decoupling mechanism
3. Performance of the full array

The single coil performance was characterized by simulating an isolated CSA element in free space.

To understand the decoupling mechanism, a set of three coils representing the edges of the same octahedron face (e.g. channels 1, 4 and 8) were analyzed without any other coils present. The matching network was neglected, and all coils were driven at the tuning capacitor port to characterize mutual impedances directly without the transformation applied by the matching circuit. Additionally, all component losses were neglected.

Finally, the full array including all components was simulated.

3D Field Simulations

The 3D field simulations were performed using XFDTD 7.4.0.5 (Remcom, State College, PA).

The single coil was simulated at a very high (0.5 mm isotropic) resolution, and all coil faces were oriented along the coordinate axes in order to get an accurate estimate of the single coil feed- and near field impedance. The gamma feed was not considered in this setup, and coil feeding was achieved through the tuning capacitor gap.

The full array was simulated using a 2-mm isotropic resolution in the coil volume. Because of its symmetry, the coil array only has three degrees of freedom for the tune, match, and decoupling capacitances. Due to the FDTD discretization scheme, simulating the octahedral array in the in-bore orientation as depicted in Fig. 5.2 would lead to unrealistic asymmetries in the calculated port impedances, manifesting as different required tuning, matching and decoupling capacitances depending on coil orientation. In order to preserve symmetry, the coil was oriented differently in simulation, as shown in Fig. 5.3. The final coil fields were rotated in post-processing to restore the actual in-bore orientation.

Preservation of all symmetries also required neglecting the gradient shield and bore from the simulation. This is a common approach, however the simulated far field

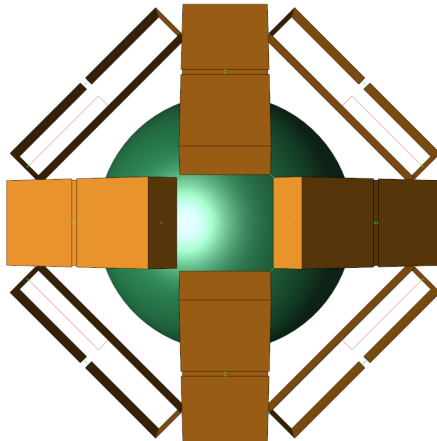


Figure 5.3: Orientation of the coil array as used in simulation in order to preserve all symmetries.

radiation losses are usually overestimated [115]. This loss component will hence be critically discussed in detail.

The simulations were performed with a 7-cell perfectly matched layer (PML) boundary to allow far-field radiation, and employed a 0.25λ (60 cm) free-space padding in order to separate the reactive near field from the absorbing boundaries.

All variable elements were replaced with 50Ω feeds, requiring a total of 60 ports.

Co-Simulation

Based on the S-Parameters from the 3D simulations, ADS (Agilent, Santa Clara, USA) was employed for circuit co-simulation. For the decoupling characterization of the three-coil set, all other ports were left unconnected in the co-simulation. In order to tune, match, and decouple the coil, the power reflected from the array when driving a single channel was minimized [85], where only one channel needs to be considered due to the coil symmetry. In order to assure convergence to a global optimum, a wide range of the tune-match-decouple parameter space was evaluated.

Loss modeling

Copper losses determined through FDTD simulations have been shown to be potentially prone to large errors [132], especially for thin rectangular conductors influenced by the lateral skin effect [133]. The lateral skin effect influence on current density is depicted in Fig. 5.4. The increasing current density curvature towards the conductor edges is difficult to reproduce in a numerical model without resorting to impractically high mesh resolutions.

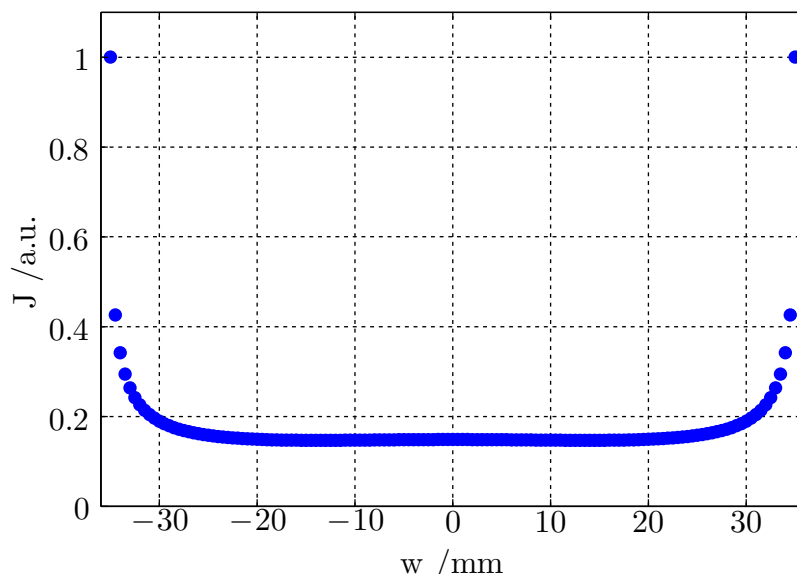


Figure 5.4: Simulated current density J distribution along a 70 mm wide copper strip with the strong increase in current density towards the edges indicating the lateral skin effect.

A closed form analytical solution for losses in a conductor with rectangular cross-section does not exist, unfortunately [134]. Hence, three different numerical and semi-analytical approaches were explored and compared.

The first estimate was calculated via the high resolution single CSA FDTD simulation. To this end, the copper conductivity was assumed as 5.98×10^7 S/m, and a good conductor approximation enabled in XFDTD [135].

For a second estimate, the lateral skin effect was neglected, and the resistance was calculated using a simple planar estimation for a 400-mm long, 70-mm wide copper strip with a skin depth of $5.86 \mu\text{m}$, an approach that was previously employed for SNR estimation for receive coil arrays [136].

Finally, the software package FastHenry [137] was utilized to model the copper losses. There, the copper sheet was discretized into 400-mm length wire filaments, with 100 filaments across the width and 20 across the thickness of the sheet.

The loss estimates gained from the three methods were compared (see “Loss characterization” on page 67) and the FastHenry estimate was used to approximate copper losses in the full octahedral coil simulation using lumped resistors. Consequently, all copper components were modeled as lossless in the 3D simulation.

The 11-cm radius phantom was comprised of a gel with a conductivity of $\sigma = 0.33$ S/m and permittivity $\epsilon = 76$.

Capacitor losses were taken from data sheets for ATC 100E type capacitors (American Technical Ceramics, Huntington Station, NY, USA), and solder losses estimated

using literature data [136]. In the following analysis, capacitor losses are always given including their associated solder joint losses.

Effects of parallel capacitance splitting

As will be shown in the further analysis, the singular tuning capacitor introduces strong losses. To assess the potentially mitigating effect of splitting the tuning capacitor into multiple parallel elements [136], the total resulting resistance for multiple splitting configurations (1-10 capacitors) was calculated analytically. For this purpose, an empirical model was constructed for the equivalent series resistance (ESR) of the utilized capacitors. The equation

$$ESR = \left[a \cdot \left(\frac{C}{1 \text{ pF}} \right)^b + d \right] \Omega \quad (5.1)$$

contains the capacitance C and three free parameters a , b and d , which were fitted to ESR values published by the manufacturer. The resulting model can be used to calculate the total resistance of an arbitrary capacitor arrangement.

5.2.2 Maximum B_1 and Receive SNR analysis

Based on the simulated B_1 fields and the coil loss data, a maximum transmit- and receive efficiency analysis was performed. Due to reciprocity and the fluctuation-dissipation theorem [55, 138], maximizing transmit field strength is closely related to the optimum superposition of multi-channel receive data [14, 86]. Both cases require to find an optimum vector \mathbf{v} in order to maximize a generalized Rayleigh quotient [62, 90],

$$\mu^2 = \frac{\mathbf{v}^H \mathbf{B} \mathbf{v}}{\mathbf{v}^H \mathbf{Q} \mathbf{v}}, \quad (5.2)$$

where $B_1^2 = \mathbf{v}^H \mathbf{B} \mathbf{v}$ is the square of the local strength of the transmit or receive field, with the matrix \mathbf{B} derived individually for every voxel by calculating the outer product of the local transmit or receive sensitivity vector $\mathbf{b}(\mathbf{r})$, i.e.

$$\mathbf{B} = \mathbf{b}(\mathbf{r}) \mathbf{b}(\mathbf{r})^T, \quad (5.3)$$

where the spatial dependence in $\mathbf{b}(\mathbf{r})$ is implied from now on. The expression $\mathbf{v}^H \mathbf{Q} \mathbf{v}$ is a quadratic form of some power correlation matrix \mathbf{Q} , where the exact choice of \mathbf{Q} depends on the desired application.

To derive a figure proportional to SNR, the ratio of receive sensitivity B_1^- and total noise power needs to be maximized. For this purpose, the noise power correlation matrix \mathbf{Q}_N is derived from the reflected power correlation matrix according to Bosma's theorem as $\mathbf{Q}_N = \mathbf{Q}_{fwd} - \mathbf{Q}_{ref}$ [128].

For transmit efficiency, multiple choices of \mathbf{Q} are possible. Choosing \mathbf{Q}_{fwd} estimates efficiency with respect to forward power, while \mathbf{Q}_{mat} gives an estimate of efficiency vs. absorbed power and thus SAR.

Independent of the choice for \mathbf{Q} , the maximum ratio is reached with a vector

$$\mathbf{v} \propto \mathbf{Q}^{-1}\mathbf{b}^*, \quad (5.4)$$

leading to the maximum value of

$$\mu = \sqrt{\mathbf{b}^H \mathbf{Q}^{-1} \mathbf{b}}. \quad (5.5)$$

In order to derive each individual loss mechanism's contribution to the overall received noise at a certain location, the optimum weighting vectors \mathbf{v} are calculated for every voxel location \mathbf{r} . It is then possible to analyze the fractional contributions of all loss mechanisms to the total generated noise. With the locally optimal weighting vector given as $\mathbf{v} = \mathbf{Q}_N^{-1}\mathbf{b}^*$, the fraction η of the total noise power contributed by a loss mechanism with a corresponding power correlation matrix \mathbf{Q}_L is given by

$$\eta = \frac{\mathbf{b}^T (\mathbf{Q}_N^{-1})^H \mathbf{Q}_L \mathbf{Q}_N^{-1} \mathbf{b}^*}{\mathbf{b}^T (\mathbf{Q}_N^{-1})^H \mathbf{b}^*}. \quad (5.6)$$

Calculating this ratio using all desired loss matrices (e.g. dissipative losses, tune capacitance losses, decoupling component losses, etc.) yields spatially resolved maps detailing the relative contribution of each loss mechanism when performing an optimum-SNR image reconstruction.

It should be noted that the presented SNR estimation assumes ideal noiseless preamplifiers for reception. In the presence of preamplifier noise, SNR will be degraded uniformly by a factor proportional to the preamplifier noise figure. Additional spatially dependent degradation occurs via preamplifier noise coupling, which is however only relevant in case of significant coil coupling and mismatch [139, 140]. Transceive coil arrays as the one described here are generally well-matched, and are thus not impacted by preamplifier noise coupling.

5.2.3 Parallel transmission

Due to the infinite number of possible coil field superpositions, a parallel transmit efficiency evaluation is hardly possible based solely on the single channel coil fields. However, transforming the coil fields from their usual single channel basis into more suitable basis configurations allows deeper insight into the parallel transmit behavior of the system. The chosen basis configurations are given by the Eigenvectors' specific power- and energy-correlation matrices of the array. Besides the overall power balance of these modes, a specific focus lay on characterizing the coil performance in different slice orientations.

Eigenmode analysis

The first basis is given by the Eigenvectors of the phantom material loss matrix \mathbf{Q}_{mat} . The corresponding Eigenmodes are non-interacting in the sense that their electric fields \mathbf{E} and current densities \mathbf{J} are orthogonal inside the phantom, i.e.

$$\iiint_{Phantom} \mathbf{E}_i \mathbf{J}_j dv \propto \delta_{ij}. \quad (5.7)$$

They are also corresponding to a vanishing noise correlation between these modes [125]. The accompanying Eigenvalues denote the power absorption when driving this mode, which can serve as a proxy for the transmit efficiency of this mode. In the following sections, these modes will be referred to as electric Eigenmodes.

However while power loss is caused by all polarizations and components of the electromagnetic fields, only the B_1^+ component is viable for spin excitation. It is thus desirable to construct a basis of orthogonal B_1^+ modes using an approach related to a principal component analysis of receive array sensitivities [141]. For an arbitrary volume of interest V , a correlation matrix \mathbf{T} with its elements defined as

$$\mathbf{T}_{ij} = \iiint_V B_{1,i}^+ (B_{1,j}^+)^* dv \quad (5.8)$$

can be constructed from the single channel fields. Its diagonal elements correspond to the squared B_1^+ magnitude integrated over the volume of interest, which is a measure of the magnetic field energy stored in the B_1^+ field component. The off-diagonal elements represent the correlation between coil channels. An Eigendecomposition of this hermitian positive-semidefinite matrix yields orthogonal Eigenmodes, with the corresponding Eigenvalues being proportional to the magnetic field energy stored in these modes. Hence, these values are a direct indicator of this mode's transmit efficiency. This analysis was performed for three different volumes of interest corresponding to central slices in the xy, xz and yz orientation, and also the complete phantom volume.

The power balance for all constructed Eigenmodes was then calculated to investigate the influence of the different loss mechanisms on these modes.

Transmit SENSE

Finally, the array's applicability to transmit SENSE 2D spatially selective excitation was investigated. Based on the simulated fields, the excitation pulses were calculated for a target flip angle of 20° using an inward spiral trajectory on a 32×32 (240×240 mm) field of excitation for the excitation of a rectangular region. Again, the power balance was investigated for each of the excitation pulses, with a focus on similarities and differences between the three slice orientations.

5.3 Results

5.3.1 Single element characterization

Wave impedance

The current distribution along the CSA is inherently loop-like, resulting in a low wave impedance in the near field, and the heating effect can be attributed to the conservative electric fields originating from the tuning capacitor gap. Hence, if the coil is oriented with the capacitor facing away from the subject, the uninterrupted coil side opposite of the tuning capacitor acts as a shield preventing the electric fields from further penetration. The wave impedance in the central zy coil plane is depicted in Fig. 5.5 and clearly shows the described difference between coil sides.

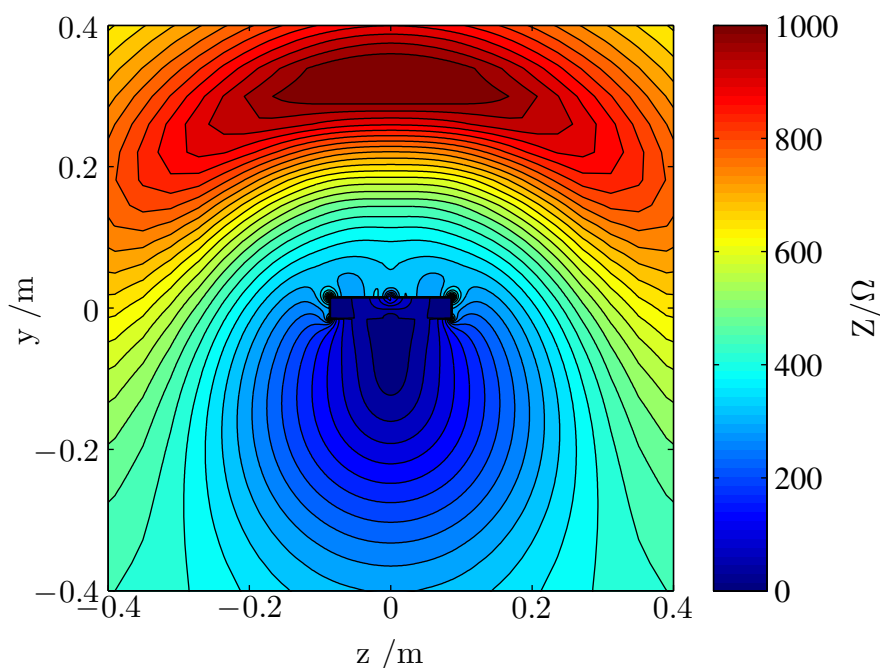


Figure 5.5: Simulated wave impedance Z of a CSA element with the capacitor placed at the top of the coil. It is clearly evident, that the side facing the capacitor experiences high wave impedance with a maximum of about 1000Ω located approximately 30 cm away from the coil. The opposing side shows a low impedance that slowly increases with distance, which is consistent with a magnetic field source.

Loss characterization

Without any attached tuning- or matching capacitor, the coil impedance at the gap was determined as $Z = 0.174 + i60.5 \Omega$, corresponding to an inductance of 78 nH.

The power balance of a loaded single CSA element is shown in Tab. 5.1. The power efficiency of just 37% corresponds to a Q-ratio of 1.6, which indicates an undesired coil loss dominance.

Mechanism	Loss fraction
Phantom	37.3%
Tune Capacitor	47.5 %
Radiation	10.0 %
Copper	4.8 %
Match Capacitor	0.3 %

Table 5.1: Power balance of a single loaded and tuned CSA element. Solder joints are included with the capacitor losses.

The copper loss percentage translates to an equivalent series resistance of 16 m Ω . The simple planar approximation neglecting the lateral skin effect yields approximately 8 m Ω , and the calculation using FastHenry resulted in a resistance estimate of 20 m Ω . As expected, neglecting the lateral skin effect would result in a significant underestimation of losses. The estimates from the 3D simulation and FastHenry however, are in relatively close agreement, indicating that a sufficiently high resolution FDTD simulation without oblique copper surfaces can yield relatively accurate loss estimates. As a further increase in the FDTD resolution would likely result in a convergence of the resistance towards the high resolution FastHenry result, a 20 m Ω resistor was chosen to represent copper losses in the full octahedral coil simulation.

The fitted model of a capacitor's ESR is shown in Fig. 5.6

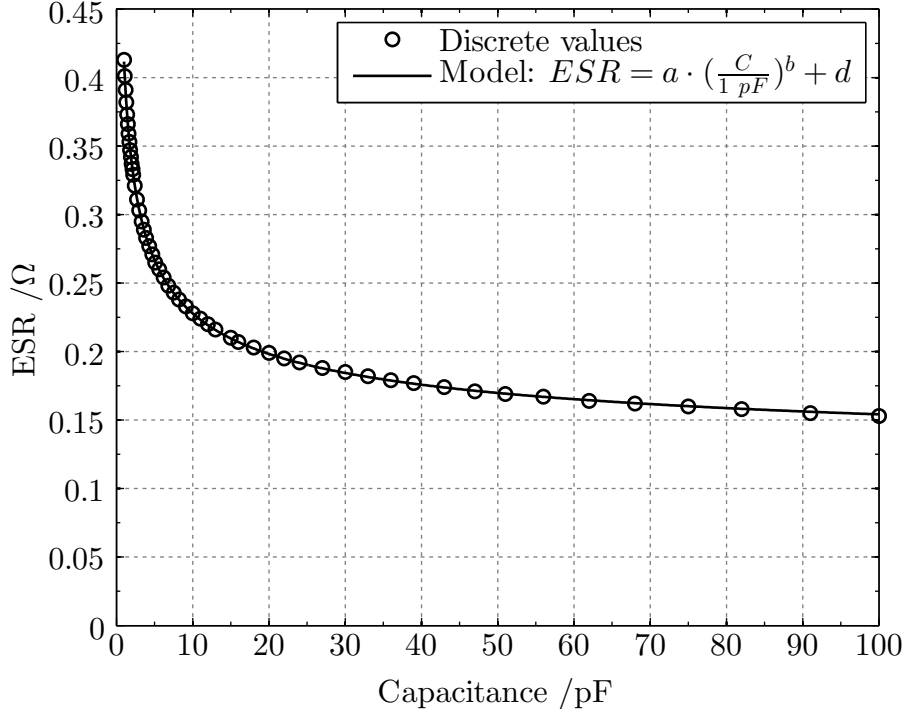


Figure 5.6: ESR dependence on the capacitance. The figure shows both the resistance values given by the manufacturer for all available capacitors between 1 and 100 pF and the model function fitted to these values. An excellent agreement with $R^2 = 0.99995$ is visible. The fitted parameters are $a = 0.307 \Omega$, $b = -0.397$ and $d = 0.105 \Omega$.

It becomes obvious that smaller capacitances exhibit larger series resistances. The total capacitance resulting from connecting multiple capacitors in parallel is equal to the sum of the individual capacitance values. Hence, parallel splitting of a capacitor requires multiple smaller capacitors with higher individual ESR values. This is countered by the total resistance decrease following the parallel connection of the individual resistances. As long as the inequality

$$a \cdot \left(\frac{C}{1 \text{ pF}} \right)^b + d > \frac{a}{n} \cdot \left(\frac{C}{n \cdot 1 \text{ pF}} \right)^b + \frac{d}{n} \quad (5.9)$$

holds, splitting of a capacitor with a capacitance C into n parallel elements with capacitance C/n will result in a lower total resistance. For a 20 pF component, which is approximately equal to the tuning capacitance required for a CSA element, the achievable loss reduction is shown in Fig. 5.7.

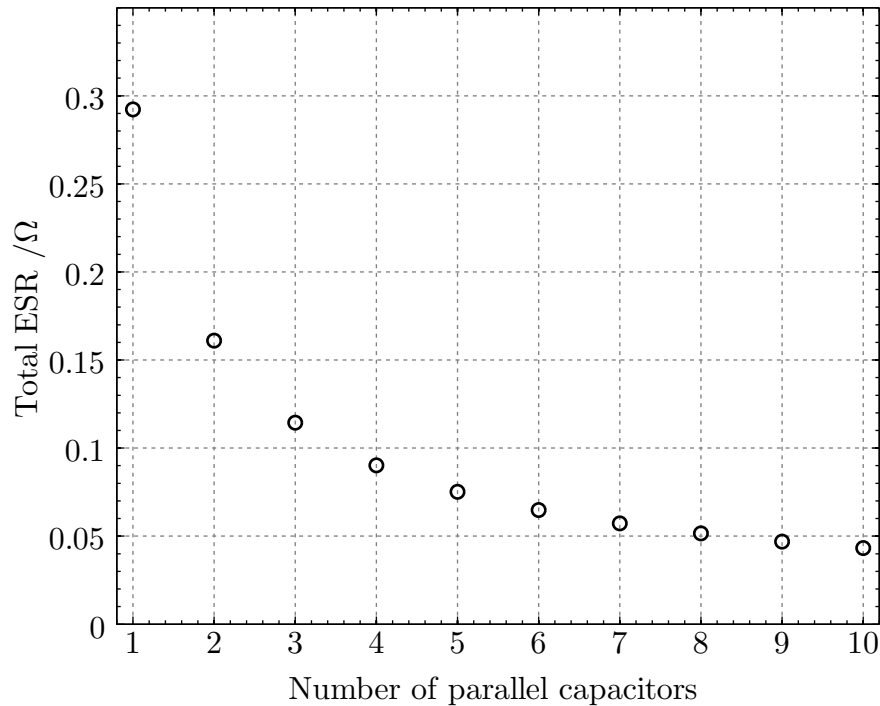


Figure 5.7: Total ESR dependence on number of parallel capacitors and a constant total capacitance of 20 pF. The resistance drops significantly with an increasing number of parallel capacitors. An exemplary practical case of 5 parallel capacitors (e.g. 4 fixed and 1 variable) would yield a resistance reduction by a factor of 3.9.

5.3.2 Decoupling mechanism analysis

The impedance matrix \mathbf{Z} of three coils comprising the edges of an octahedral face is given by

$$\mathbf{Z} = \begin{bmatrix} 0.19 + 60i & 0.015 - 1.36i & 0.015 - 1.36i \\ 0.015 - 1.36i & 0.19 + 60i & 0.015 - 1.36i \\ 0.015 - 1.36i & 0.015 - 1.36i & 0.19 + 60i \end{bmatrix} \Omega. \quad (5.10)$$

For a tuned coil, the imaginary diagonal components vanish; and perfectly compensating the inductive coupling component would eliminate the imaginary off-diagonal components. The residual resistive coupling factor of $k = 0.015/0.19 = 0.079$ would, in theory, lead to a remaining coupling of ≈ -28 dB.

Inserting the decoupling capacitors and adjusting for compensation of the inductive coupling leads to an impedance matrix of

$$\mathbf{Z} = \begin{bmatrix} 0.40 + 60i & 0.20 & 0.20 \\ 0.20 & 0.40 + 60i & 0.015 \\ 0.20 & 0.20 & 0.40 + 60i \end{bmatrix} \Omega. \quad (5.11)$$

The imaginary off-diagonal components have been fully compensated, however the self resistances, and most significantly, the mutual resistances increased significantly. With a resulting resistive coupling factor of $k = 0.5$, the residual coupling now is increased to ≈ -13 dB.

5.3.3 Full array analysis

Tuning, Matching, and Decoupling

The results of the capacitance parameter sweep are shown in Fig. 5.8. A single maximum is visible, indicating that the found capacitances represent the globally achievable optimum in terms of single channel transmit efficiency.

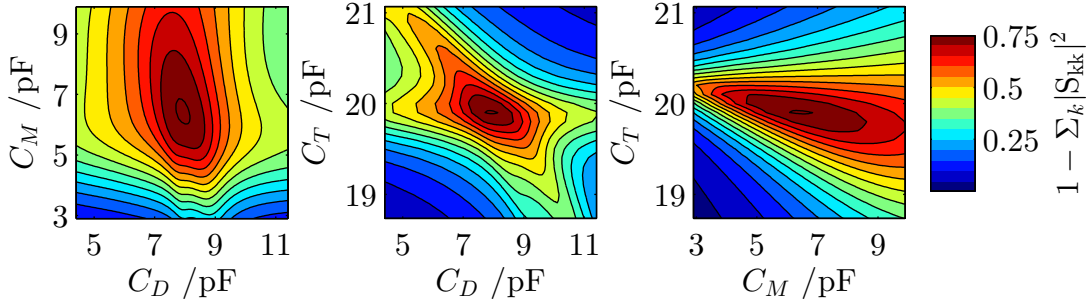


Figure 5.8: Depiction of the tuning-matching-decoupling capacitance parameter space in three orthogonal slices centered at its maximum ($C_T = 19.9$ pF, $C_M = 6.4$ pF and $C_D = 7.9$ pF). The transmit efficiency $P_{eff} = 1 - \sum_k |S_{kk}|^2$ shows a global maximum without any adjacent local maxima.

The resulting scattering matrix is shown in Fig. 5.9. As previously noted by Kozlov and Turner [85], the maximum absorbed power in a coupling transmit array occurs for a configuration that is not perfectly matched ($|S_{kk}| \approx -13$ dB).

Single channel excitation

When integrated into the array, a single element behaves differently compared to the previously investigated isolated coil due to interactions with the other array

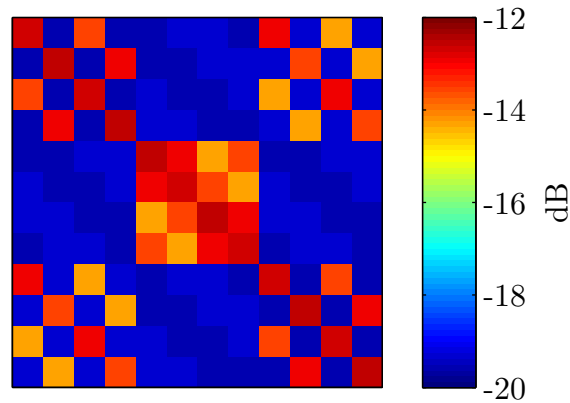


Figure 5.9: Scattering matrix of the simulated octahedral array.

elements. The power balance of the single channel excitation, shown in Tab. 5.2, reveals a redistribution of the input power compared to Tab. 5.1. The total power absorbed in the phantom is very slightly increased, and the losses inside the tuning capacitors and copper are halved. Radiative losses are decreased as well.

Mechanism	Loss fraction		
	Self	Global	Other
Phantom	-	38.9 %	-
Coupling	-	27.6 %	-
Copper	2.1 %	-	0.3 %
Tune capacitors	20.7 %	-	3.1 %
Match capacitors	0.5 %	-	0.1 %
Decoupling capacitors	-	0.8 %	-
Radiation	-	5.9 %	-

Table 5.2: Power balance of the coil array when driving a single channel. The losses are separated into self losses (occurring in the actively driven coil itself), global losses (not assignable to a single coil) and other losses (occurring in the passive coils and interlinking capacitors)

The B_1^+ field distributions for all single channels are given in Fig. 5.10. Depending on the relative orientation of the coil element towards the slice, different sensitivity profiles can be observed. While the xy oriented slice is well covered with the field profiles, the remaining two orientations display sensitivity drops towards the front and back ($\pm z$) regions of the phantom.

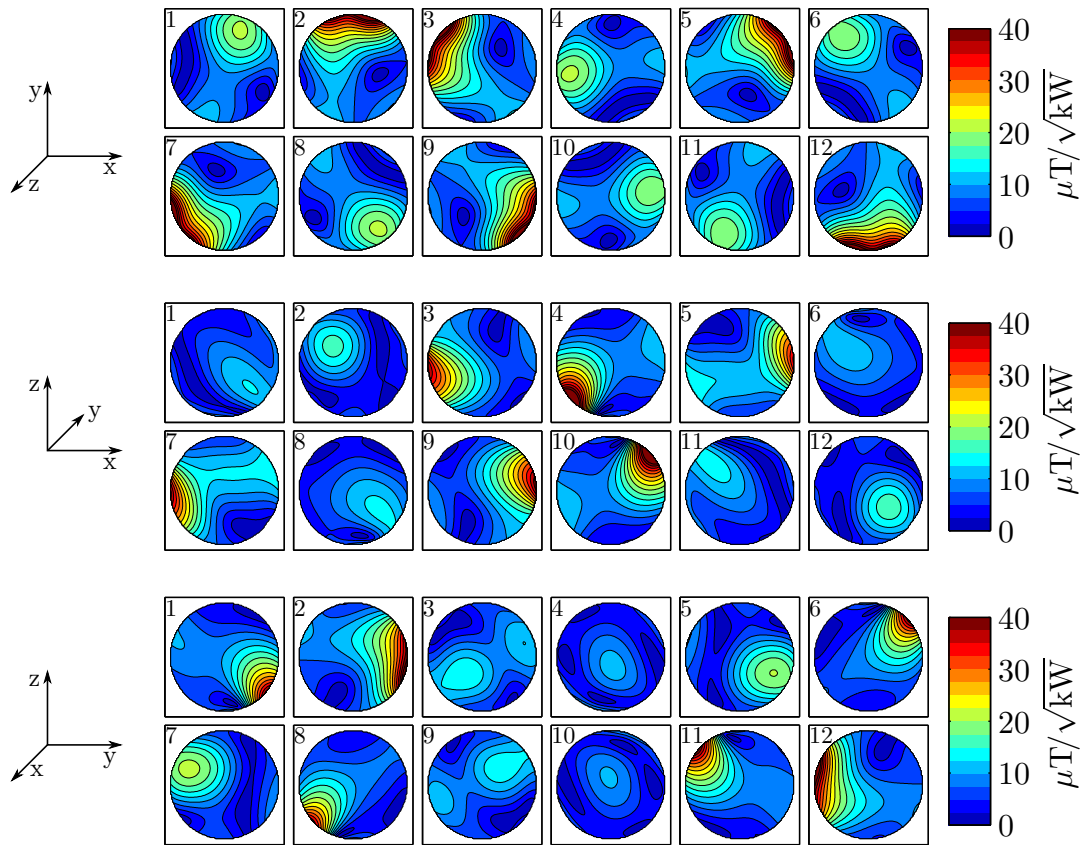


Figure 5.10: Single channel B_1^+ distributions in the central slices of the xy (top), xz (middle) and yz plane (bottom).

Maximum transmit- and receive efficiencies

SNR maps comparing the ideally obtainable to the realistic case are shown in Fig. 5.11. While central SNR is close to optimal (95 %), it significantly drops in the periphery, which is an expected behaviour of lossy array coils [125].

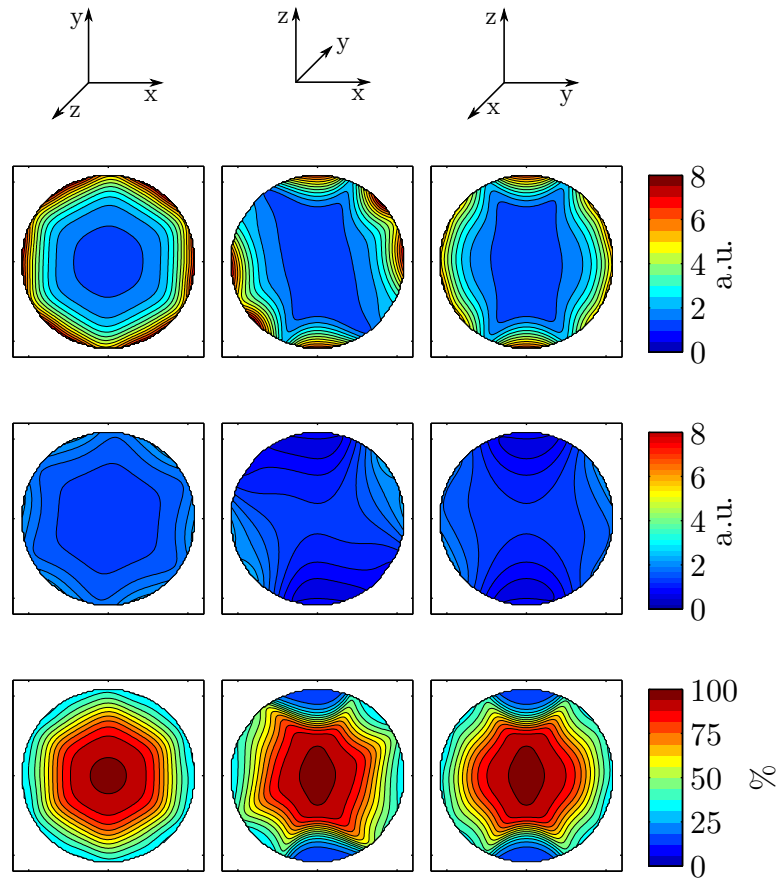


Figure 5.11: SNR distributions for the theoretical optimum considering only phantom noise (top) and realistic losses (center). The bottom figure shows the ratio of realistic vs. optimum SNR.

Noise contribution maps derived from the optimum SNR combination vectors are given in Fig. 5.12. These maps can be used to gauge the exact impact of the individual losses on SNR. The two low-SNR regions located at the $\pm z$ phantom locations visible in the xz and yz slices are dominated by losses in the coil copper conductors as well as tuning and matching capacitors. Radiative losses show a similar qualitative behavior. In contrast, noise originating from the decoupling capacitors shows a minimum at these locations, and an overall different distribution.

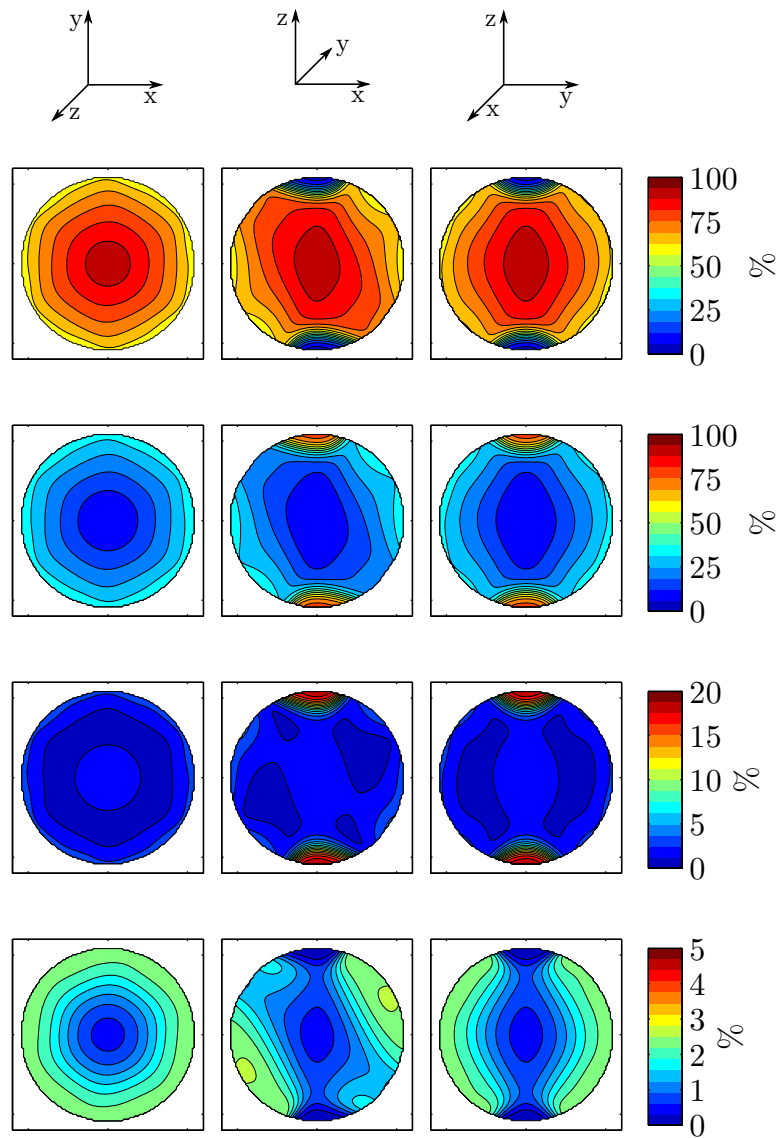


Figure 5.12: Relative noise contributions from the different loss mechanisms from top to bottom: phantom; copper, tune and match capacitors together; radiation; decoupling capacitors.

Reciprocity and the still comparatively strong similarity between the B_1^+ and B_1^- component at 123 MHz result in a distribution of the maximum transmit efficiency that is qualitatively comparable to the previously shown optimum SNR maps. Figure 5.13 shows the maximum achievable transmit efficiency with respect to forward power and phantom absorbed power, corresponding to using Q_{fwd} and Q_{mat} in Equation 5.5, respectively.

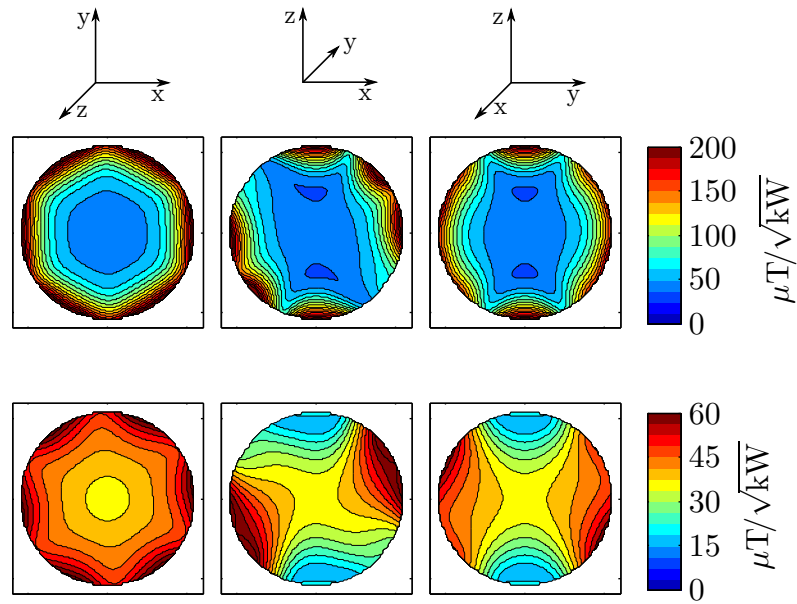


Figure 5.13: Maximum transmit efficiency with respect to absorbed power (top) and forward power (bottom). At each point the given value corresponds to the maximum possible transmit field strength attainable while fixating either absorbed or forward power at 1kW, respectively.

Maximum and minimum losses

The loss components contribute differently to the total power balance based on the excitation mode, with their range being constrained by the smallest and largest Eigenvalue of the corresponding loss matrices, which are given in Tab. 5.3. A large range spanning multiple orders of magnitude is visible for almost all loss contributions. Copper, matching and decoupling losses are comparatively small and, even taken together, always contribute less than 8 % of the total losses.

Electric Eigenmodes

The Eigendecomposition of the phantom material loss matrix yielded twelve distinct Eigenmodes. The accompanying power balances are detailed in Tab. 5.4. Due to the coil's symmetries, the Eigensystem displays multiple degeneracies. Particularly, there are three triply degenerate Eigenvalues ($\{1; 2; 3\}$, $\{4; 5; 6\}$ and $\{8; 9; 10\}$), one doubly degenerate Eigenvalue ($\{11; 12\}$) and one non-degenerate mode ($\{7\}$). The power balances are visualized in Fig. 5.14.

Losses	Max [%]	Min [%]
Phantom	77.1	0.8
Coupling	53.8	9.7
Copper	4.0	0.5
Tune capacitors	40.0	5.1
Match capacitors	1.0	0.1
Decoupling capacitors	2.9	0.0
Radiated	21.9	0.0
Error	0.011	<0.001

Table 5.3: Maximum and minimum loss contributions for all loss mechanisms. Additionally, the bottom row shows the maximum and minimum possible power imbalance of the simulation.

Losses [%]	Eigenmode No.					
	1	2	3	4	5	6
Phantom	77.1	77.1	77.1	64.4	64.4	64.4
Coupling	15.0	15.0	15.1	9.7	9.7	9.7
Copper	0.5	0.5	0.5	2.1	2.1	2.1
Tune capacitors	5.2	5.1	5.1	21.2	21.2	21.2
Match capacitors	0.3	0.3	0.3	0.7	0.7	0.7
Decoupling capacitors	0.4	0.4	0.4	1.8	1.8	1.8
Radiated	1.5	1.5	1.5	0.1	0.1	0.1
	7	8	9	10	11	12
Phantom	36.8	1.3	1.3	1.3	0.9	0.8
Coupling	37.8	37.2	37.2	37.2	53.8	53.8
Copper	2.0	3.6	3.5	3.5	4.0	4.0
Tune capacitors	20.3	35.3	35.3	35.3	40.0	40.0
Match capacitors	0.1	0.7	0.7	0.7	1.0	1.0
Decoupling capacitors	2.9	0.0	0.0	0.0	0.0	0.0
Radiated	0.0	21.9	21.9	21.9	0.4	0.4

Table 5.4: Power balance for the electric Eigenmodes.

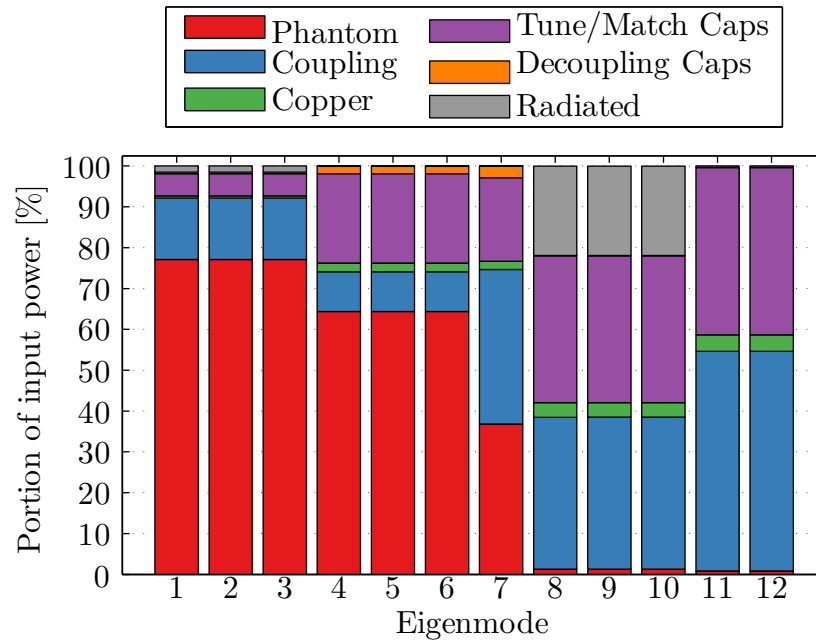


Figure 5.14: Visualization of the electric Eigenmodes' power balance.

Only modes 1-7 show appreciable power deposition in the phantom, and, by proxy, can be expected to contribute significant excitation fields. This is confirmed by the B_1^+ distributions of the modes, shown in Fig. 5.15, with modes 8-12 displaying a negligible transmit sensitivity in all three slice orientations.

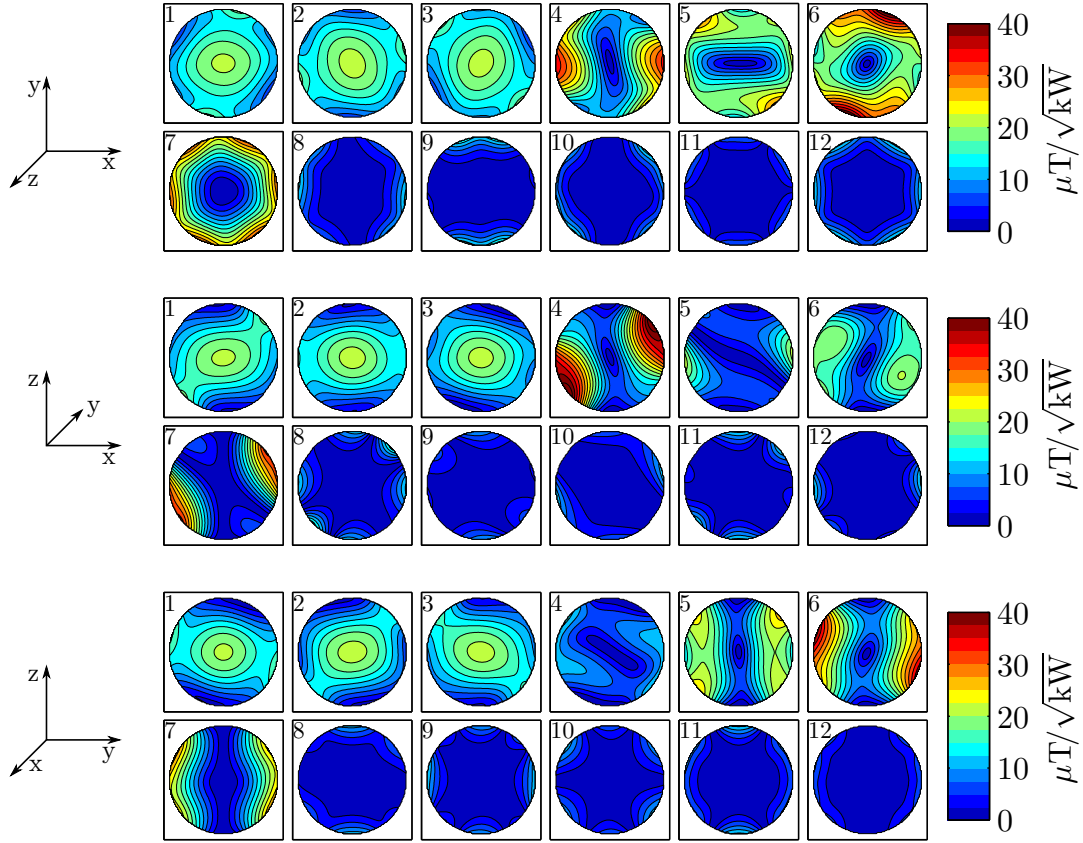


Figure 5.15: B_1^+ distributions of the electric Eigenmodes in the central xy (top), xz (center) and yz (bottom) slice.

The first three modes correspond to linearly polarized fields created by four individual channels each. The three sets are each comprised of the coils lying in the same plane, i.e. the coil sets $\{2; 4; 12; 10\}$, $\{1; 3; 11; 9\}$ and $\{5; 6; 7; 8\}$. Each coil is driven with the same amplitude and phase offsets to resemble the fields of large loop-like currents flowing through the connected coils. Based on the visualized current directions given in Fig. 5.2, this translates to alternating 0° and 180° phase shifts. The nondegenerate mode 7 is generated by driving all coils with equal amplitudes and phases.

Central transmit efficiency, provided by modes 1-3, is very similar between the slice orientations. However, while the peripheral sensitivity distributions of modes 4-7 show a complete circumferential coverage of the xy slice, they display a distinct lack of significant coverage in the $\pm z$ regions of the phantom, which is consistent with the single channel profiles.

Magnetic Eigenmodes

The field distributions for the magnetic Eigenmodes orthogonalized over the individual slices are shown in Fig. 5.16. Again, the lack in $\pm z$ sensitivity in the xz and yz slices is obvious and contrasted by complete azimuthal coverage in the xy slice.

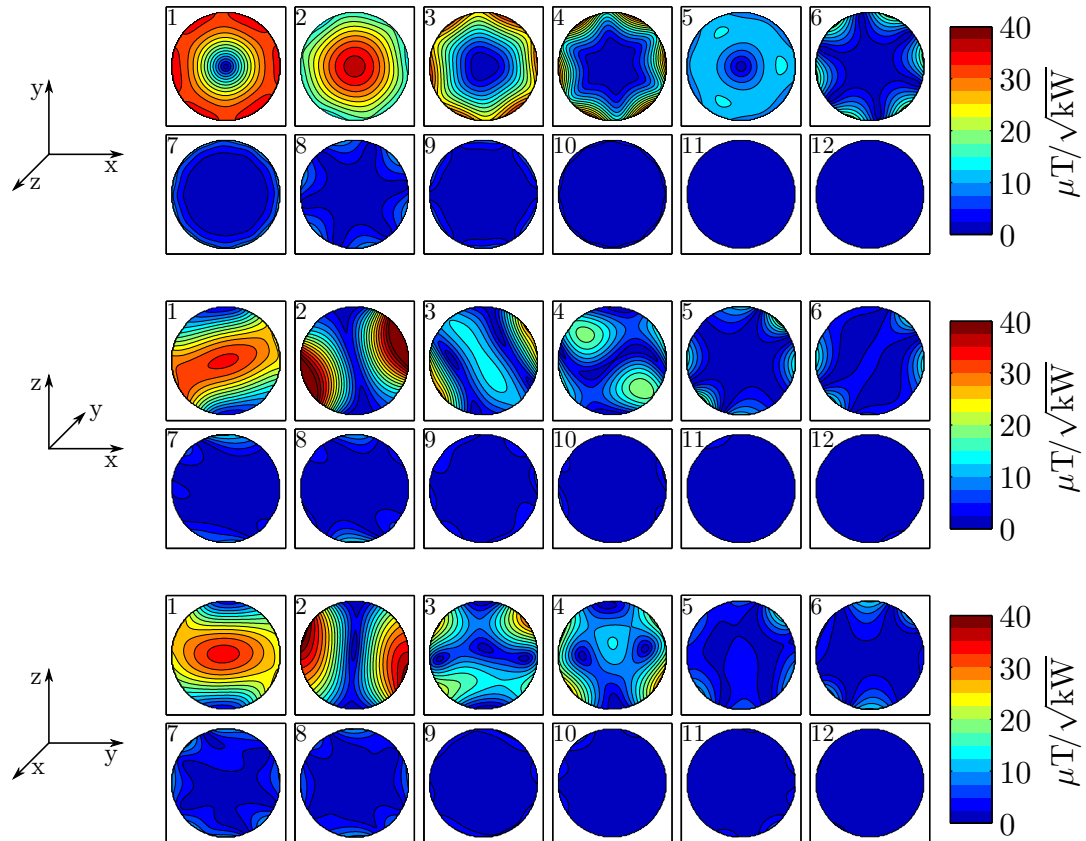


Figure 5.16: B_1^+ distributions of the magnetic Eigenmodes in the central xy (top), xz (center) and yz (bottom) slices. The modes are pairwise orthogonal inside the respective slices, and are sorted by the stored magnetic field energy of the B_1^+ component in descending order.

This sensitivity difference can be quantified by cumulatively summing the Eigenvalues of the correlation matrix \mathbf{T}_{ij} [37, 141], as shown in Fig. 5.17. The cumulative sum for the xz and yz slices is approximately equal, and about 30 % below the sum of the xy slice.

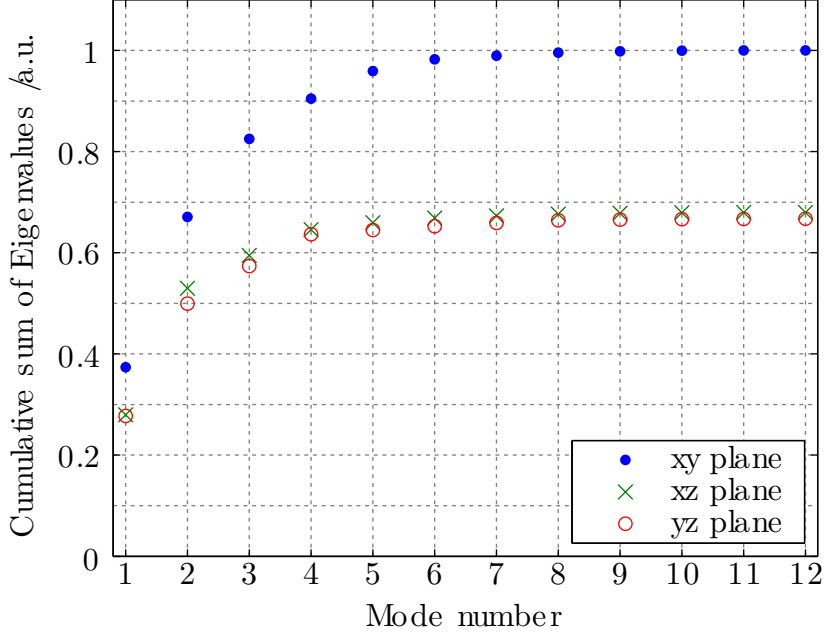


Figure 5.17: Normalized cumulative sums of the Eigenvalues.

While this analysis can be performed over any arbitrary volume of interest in order to characterize the locally orthogonal distributions, it is useful to examine globally orthogonal modes over the complete phantom volume. In this way, they can be put into relation to the previously discussed electric Eigenmodes characterized by orthogonality of the electric fields over the complete phantom. The resulting B_1^+ distributions can be found in Fig. 5.18. The highest energy mode is characterized by a central null and a strong peripheral field strength, and the second-highest mode corresponds to the equivalent of a circular polarized homogeneous birdcage mode, and corresponds to adding the first three electric Eigenmodes from Fig. 5.14 with equal weights. All modes show the aforementioned sensitivity lack in the $\pm z$ phantom regions.

The power balance for these modes, given in Tab. 5.5 and visualized in Fig. 5.19, is especially valuable as it allows to identify losses for the most relevant excitation modes. The homogeneous (2nd) mode is most hampered by coupling losses, whereas the first and higher-order modes suffer mostly from losses in the tuning capacitors. Additionally, the third mode shows very strong coupling losses. Even though the ninth mode shows a negligible contribution to overall transmit sensitivity, it nevertheless strongly couples to the phantom. This indicates the production of a non-usable, e.g. opposite rotating, polarization in this mode.

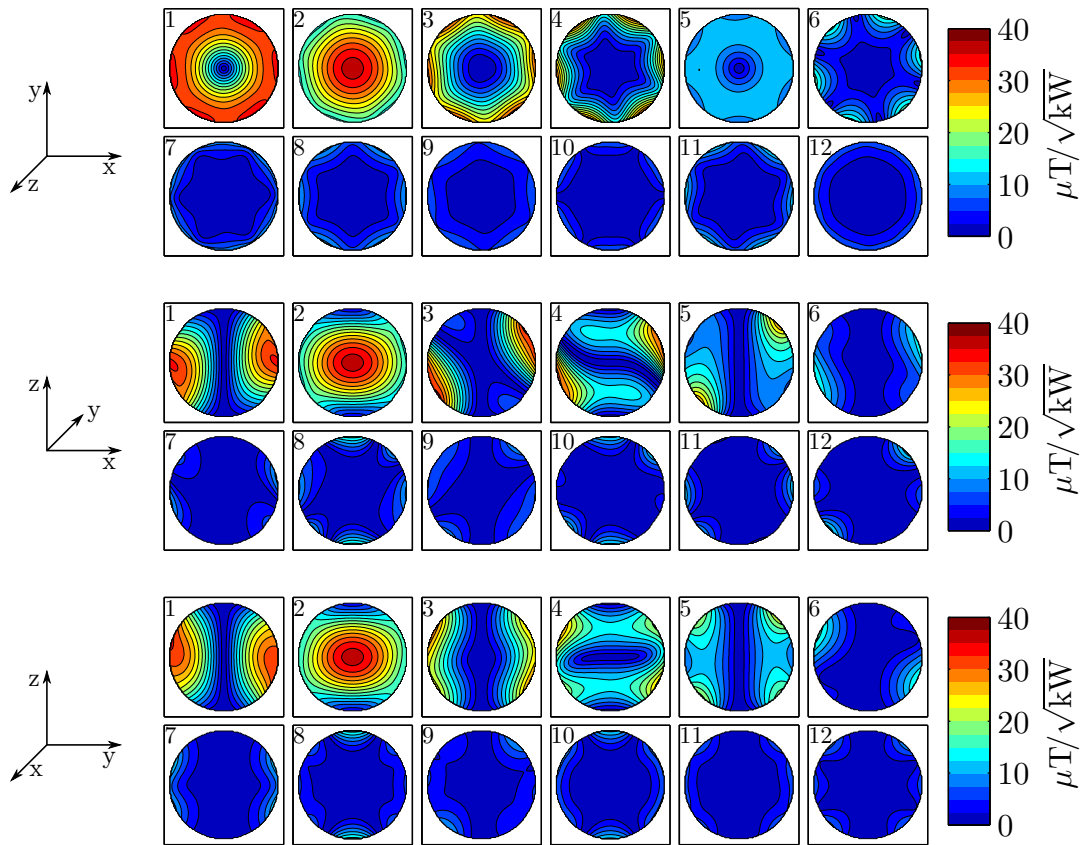


Figure 5.18: B_1^+ distributions of the magnetic Eigenmodes in the central xy (top), xz (center) and yz (bottom) slices when orthogonalized over the full phantom volume. They are again sorted by the stored magnetic field energy of the B_1^+ component in descending order.

Losses [%]	Eigenmode No.					
	1	2	3	4	5	6
Phantom	64.3	77.1	37.7	64.1	64.3	75.0
Coupling	9.7	15.0	37.3	9.8	9.8	16.1
Copper	2.1	0.5	2.0	2.1	2.1	0.6
Tune capacitors	21.2	5.1	20.0	21.3	21.3	6.1
Match capacitors	0.7	0.3	0.1	0.7	0.7	0.3
Decoupling capacitors	1.8	0.4	2.8	1.8	1.8	0.4
Radiated	0.1	1.5	0.0	0.2	0.1	1.5
	7	8	9	10	11	12
Phantom	1.4	1.5	76.2	0.8	2.9	0.8
Coupling	37.2	37.1	15.5	53.8	52.7	53.8
Copper	3.5	3.5	0.6	4.0	3.9	4.0
Tune capacitors	35.3	35.3	5.5	40.0	39.0	40.0
Match capacitors	0.7	0.7	0.3	1.0	1.0	1.0
Decoupling capacitors	0.0	0.0	0.5	0.0	0.0	0.0
Radiated	21.9	21.9	1.4	0.4	0.4	0.4

Table 5.5: Power balance for the magnetic Eigenmodes

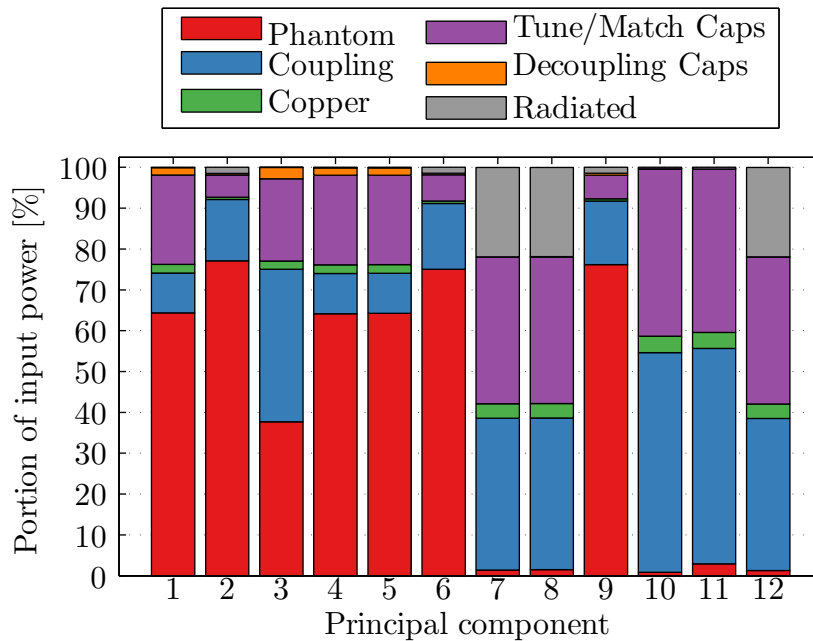


Figure 5.19: Visualization of the power balance for the magnetic Eigenmodes.

Transmit SENSE

The power balance throughout a transmit SENSE pulse for excitation of a homogeneous rectangular region is shown in Fig. 5.21 for xy, xz and yz slice orientations, respectively. To give insight into quantitative power requirements, the total forward power over the pulse is shown in Fig. 5.20.

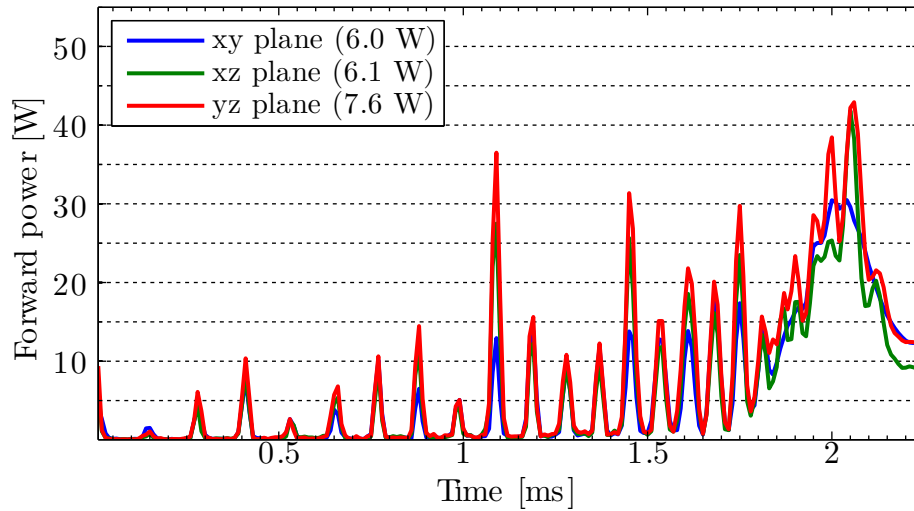


Figure 5.20: Forward power over time for the selective excitations. The average forward power is given in parentheses in the legend.

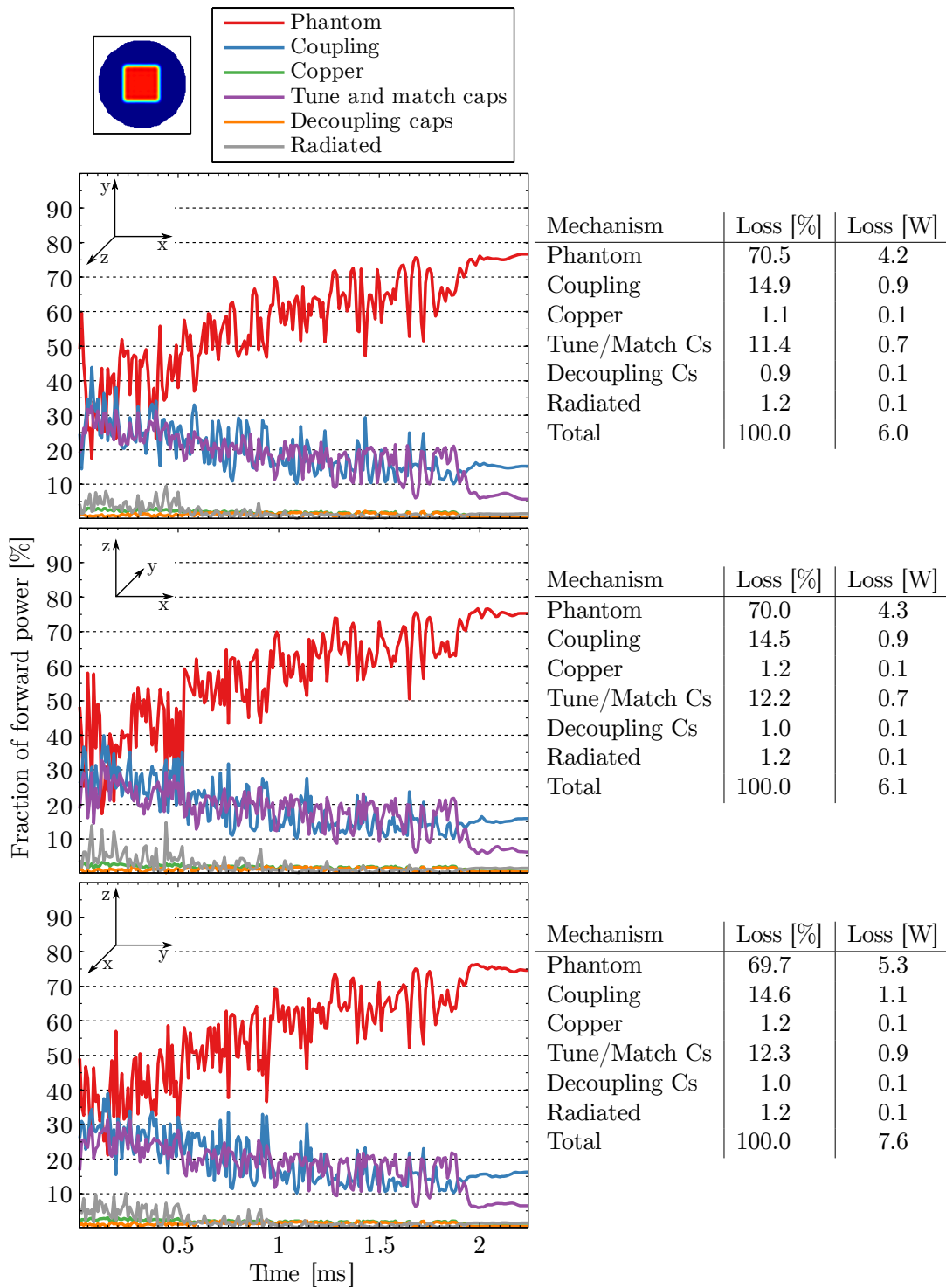


Figure 5.21: Power balance time courses of 2.3 ms-length transmit SENSE pulses for the selective excitation of a rectangular region (shown in the top left) with a 20° flip angle in the central xy (top), xz (center) and yz (bottom) plane. The tables on the right side show the integrated fractional power contributions in percent and total power in Watt.

5.4 Discussion

Power imbalance

The maximum simulation imbalance of 0.01 % as shown in Tab. 5.3 indicates a well executed simulation. The residual imbalance can be mainly attributed to numerical errors introduced by the FDTD method when using graded meshes [142], and is comparable or even lower than previously reported values for other coil geometries [43].

Single coil

A correctly oriented current sheet antenna features a highly favorable, i.e. low, near field impedance, as can be seen in Fig. 5.5. However, it only weakly couples to the sample due to the required upright orientation of the coil resulting in anti-parallel current paths, similar to microstrip elements [23] or other vertical coil configurations [143]. Consequently, the coil element performance is easily hampered by intrinsic ohmic losses, with the tuning capacitor constituting the major loss component and non-sample noise source (Tab. 5.1). Splitting of the tuning capacitor into multiple parallel components could significantly alleviate this drawback, as was shown using an empirical model of the capacitor ESR (Figs. 5.6 and 5.7).

Decoupling

While inductive coupling can be fully compensated with the chosen setup, resistive coupling is strongly increased. This behavior can be explained by the fact, that the loop formed by three CSA elements on the edges of one octahedron face together with the three interconnecting decoupling capacitors shows a significant resistive loading by the phantom. As all three elements are similarly coupled to this loop, its resistance is seen as a mutual resistance in all three elements, limiting the achievable decoupling and increasing noise correlation. In the full array configuration, coupling constitutes the strongest loss factor for single-element excitation, and also is responsible for the majority of power loss in 9 of the 12 magnetic Eigenmodes of the array. However, given sufficiently powerful amplifiers, this loss factor could be overcome. Additionally, receive sensitivity is not influenced by power reflection, as signal and noise are equally attenuated.

Field profile coverage

The single channel sensitivity profiles (Fig. 5.10) as well as electric and magnetic Eigenmode distributions (Figs. 5.15 and 5.18) show a strong central coverage, with a distinct sensitivity lack in the front and back ($\pm z$) phantom regions, visible only

on the xz and yz slice orientations. The receive sensitivity distributions also mirror these characteristics. This is explained by the fact that the array elements do not identically cover the three canonical slice directions, and also feature field components parallel to B_0 , i.e. along z , which do not contribute to MR excitation or signal reception in certain locations. These non-contributing field components however still induce losses in the sample, thus contributing to overall noise. Due to the octahedral geometry, it is unavoidable to generate unusable field components at certain locations, and an arbitrary rotation of the array would merely shift these “cold spots” to different positions. This drawback is in part compensated by allowing the coil elements to be located closer to the phantom, thus increasing their sensitivity in spite of producing partially unusable field components.

Receive sensitivity and noise analysis

The SNR distributions given in Fig. 5.11 agree with general phased-array expectations, with increased sensitivity in the peripheral regions of the phantom [125]. While all individual coil elements are identically loaded by the phantom due to symmetry, they nevertheless produce differing transversal B_1 fields at identical relative positions.

The theoretically optimum SNR distribution considering only induced phantom losses does not exhibit the $\pm z$ signal dropouts seen in the realistic loss case. This indicates, that some modes provide sensitivity in these areas (e.g. electric Eigenmodes 8-11 in Fig. 5.15 or magnetic Eigenmodes 8 and 10 in Fig. 5.18 for yz slices), however, they are only weakly coupled to the phantom and thus strongly dampened by intrinsic coil losses. This can be inferred by looking at the power balance of the respective modes, which all feature a relatively low power deposition inside the phantom. Nevertheless, even the theoretical optima exhibit peripheral regions of relatively low SNR in the xz and syz slices. These regions are not well covered by any of the twelve coils, thus exhibiting a lower SNR. The comparison of realistic and ideal SNR distributions hence allows the distinction between SNR decrease due to coil noise influence and intrinsically low SNR due to a lack of field coverage in the respective regions.

The noise source maps in Fig. 5.12 further strengthen the explanation of the front and back low SNR regions, where the major noise contribution is given by intrinsic coil losses in copper as well as the tuning and matching capacitors. The previously mentioned single coil element performance improvement via parallel splitting of the tuning capacitor would simultaneously lead to a significant SNR increase in these two spots. The decoupling capacitors generate a only very small fraction of less than 5% of the total noise power. However, they appear most strongly at different locations from the other intrinsic coil noise sources, exhibiting a minimum at the two low SNR regions. It thus becomes obvious that different component groups can introduce SNR degradation at different locations.

Parallel transmit- and receive acceleration capabilities

The cumulative Eigenvalue sums in Figure 5.17 allow a prediction of the maximum feasible parallel transmit- and receive acceleration factors, which should in practice be less than the number of true orthogonal modes providing a significant B_1 distribution. Overall sensitivity, as described by the total sum of Eigenvalues, is about 30% lower in the xz and yz slices as compared to the transversal xy slice, which mirrors the observation of generally lower average SNR in the respective orientations. Furthermore, the transversal cumulative sum reaches a plateau at a slightly higher mode number in comparison, potentially allowing for a slightly higher acceleration factor. Overall, an acceleration factor of four should be achievable in all orientations without significant drawbacks in image quality or excitation fidelity.

Radiated power

The contribution of radiated power to transmit power loss and receive noise requires a closer look, as radiation strongly depends on the immediate surroundings of the coil. In order to preserve the coil symmetry in the numerical evaluation, the gradient shield and magnet bore were not included in the simulation, which both strongly influence power radiation in a realistic setup. Energy propagation out of these cylindrical structures is in principle mainly caused by the excitation of transverse waveguide modes [73, 114, 123, 144]. The coupling to these modes depends on a multitude of factors such as coil geometry and positioning, the excitation mode imposed upon the array, but most importantly on the diameter of the surrounding cylindrical waveguide in relation to the coil's operation frequency. If the frequency is lower than the cutoff frequency of the waveguide, no mode can be excited and all fields exponentially decay with increasing distance from the coil. If the gradient shield or bore diameter is smaller than approximately $0.59 \cdot c/f$, no propagating mode can be excited, and only an insignificant percentage of the input power will leave the magnet bore. For the present case with a frequency of $f = 123.2$ MHz, the cutoff diameter evaluates to 1.42 m, which is significantly larger than the physical bore diameter of approximately 90 cm. Hence, no propagating mode is excited and the simulated power radiation will not be observed in a realistic setup. Instead, this power will be redistributed between the remaining loss mechanisms. However, as can be seen from the power balance of the electric and magnetic Eigenmodes, most of the modes offering a significant excitation capability, are not affected by radiated power. The first seven electric Eigenmodes all radiate less than 2% of the input power, similar to the first six magnetic Eigenmodes (see Fig. 5.14 and 5.19). Modes featuring a significant radiative loss in simulation contribute only weakly to the total sensitivity. Nevertheless, the previously mentioned modes providing sensitivity in the anterior and posterior phantom regions partially exhibit a relatively strong radiation loss of 22%, thus leading to an underestimation of the transmit- and receive capability of these modes in simulation. Consequently, SNR and transmit efficiency

in these regions is expected to be slightly improved in a realistic setup as compared to the simulation.

Transmit SENSE

The power balance time courses depicted in Fig. 5.21 show a strong similarity in their qualitative appearance. All loss terms display a fluctuating component overlaid by a monotonous progression. While phantom power deposition increases with time, the remaining loss terms decrease on average. Around 2 ms, the fluctuations decrease and all losses settle around a relatively stable value. This behavior is explained by the excitation gradient trajectory in conjunction with the Eigenmode distributions and their respective power balances.

The excitation k-space trajectory is an inward spiral, meaning that the high frequency components of the spatial pattern are excited in the early pulse stages. Since transmit SENSE utilizes the spatial variability of the field distributions for encoding of the spatial information, strongly spatially varying modes are excited during these early pulse times. These inhomogeneous modes, e.g. electric Eigenmodes above three, come with relatively high losses and a lower power deposition in the phantom. As time progresses, the central k-space is reached, corresponding to the low frequency portions of the excitation pattern. Here, only low spatial variability is needed in the excitation fields, which is provided by largely homogeneous modes such as in the electric Eigenmodes 1-3. These modes come with relatively lower losses and higher power deposition in the phantom.

Quantitatively, the xy and xz excitations appear highly similar, while significantly more power is required in the yz orientation to achieve an identical flip angle. This is also visible in Fig. 5.20, where the xy and xz excitation require approximately the same average forward power, whereas the yz profile requires approximately 25% more forward power. However, both xz and yz slice orientations show significantly higher spikes in the forward power in comparison to the xy excitation, which indicates that power reflection due to imperfect decoupling is more pronounced for these configurations. This again demonstrates the superior performance of the coil in the central xy slice direction.

5.5 Conclusion

The presented numerical analysis provides a comprehensive performance overview of the twelve channel octahedral coil array. Its building block, the current sheet antenna, was found to exhibit a very low near field impedance, as required for well-performing MR coils. However, it shows an intrinsically weak loading by the phantom, making the coil susceptible to performance degradation by internal losses.

The utilized tuning capacitor was identified as the main loss source, and splitting it into multiple parallel capacitors could significantly improve the coil performance.

The capacitive decoupling was shown to compensate nearest-neighbor inductive coil interactions at the expense of significantly increased resistive coupling. It was shown that this behavior is due to the creation of closed current loops by the introduction of the decoupling capacitors, which show a strong resistive loading by the phantom. The strong residual coupling was shown to be a major loss mechanism of the array during transmit operation.

The homogeneous excitation mode shows an efficiency of 77% in spite of the single element and coupling losses. Higher order modes, providing sensitivity in the peripheral phantom regions are more impacted by losses and coupling, and a reduction of these losses would consequently most benefit the peripheral sensitivity. Copper and decoupling capacitor losses were shown to be minimal.

Noise analysis identified a low SNR at the front and back ($\pm z$) phantom locations. There, losses in the tuning capacitor contribute the majority of noise, which could again be alleviated by capacitor splitting. Different loss mechanisms were shown to contribute different spatial noise patterns.

The overall coil performance was comprehensively optimal in the xy slice orientation, with a higher SNR and lower excitation power requirements.

It was shown that the power balance analysis can provide significant insight into the transmit- as well as receive performance of MR coil arrays and allows the identification and explanation of performance bottlenecks, allowing mitigating measures to be taken where they are most promising. As opposed to this post-hoc analysis, these investigations are ideally carried out before the construction of a coil. This allows to identify potential issues beforehand and can thus save a lot of time, and ultimately lead to significantly better performing coils.

6 Summary and Outlook

Parallel transmission in MRI is a prime candidate to tackle issues arising from RF field inhomogeneity at high and ultra-high field strengths. The contributions made to this field during the course of this thesis can be summarized in three main points:

1. Development and application of a scalable multichannel RF signal chain for parallel transmission experiments
2. Derivation of a theoretical framework for power balance and loss mechanism analysis of RF transmit coil arrays
3. Application of the loss analysis framework to a twelve-channel coil array with octahedral symmetry

The first contribution constitutes a novel hardware design for RF signal generation [38–40]. As vendor-supplied parallel transmission signal chains are usually limited in the number of channels or potentially not even available for the system in question, an extensible multi-channel signal generator was developed. Requiring only a reference clock and trigger signal, which is commonly available across system vendors, the system allows the control of up to twenty independent channels from a single standard PC fitting inside a two 19” 4HE enclosures. The signal is generated directly at the Larmor frequency, thus circumventing the need for additional modulators. In this work, a twelve channel setup was realized and applied for parallel transmission phantom experiments on a 3T MRI scanner. Bench measurements showed a good spectral quality of the output signal, and eight-channel measurement demonstrated a similar excitation fidelity as compared to the vendor supplied signal chain. Multiple sequence types were implemented, ranging from B_1 -shimmed gradient echo imaging over B_1 and B_0 mapping to transmit SENSE spatially selective excitation. Subsequently, this setup was extended to twelve channels, using four additional power amplifiers, thus going beyond the current commercially available options. Measurements were done using a twelve-channel coil with octahedral symmetry, demonstrating accelerated excitation in multiple orientations. Based on these results, it can be concluded that the setup presents a cost-effective and powerful building block for large-scale transmission arrays. An important next step to achieve this goal is to improve the integration with the system’s receive architecture to allow the utilization of RF spoiling and B_0 compensation, which crucially depends on shared frequency- and phase shifts between the transmit and receive chain. Future developments could also include increased channel numbers by synchronizing the output across multiple computers, and upgrading to a faster DAC to allow an application at 300 MHz and beyond.

Transmit coil arrays, such as the octahedral array used for the signal generator measurements, exhibit a complex power dissipation behavior based on the excitation mode used to drive them. As the power balance of an MR coil is a good indicator of its performance, a theoretical framework was derived to express Poynting's theorem for transmit coil arrays as a matrix equation in quadratic forms [43]. Based on electromagnetic simulations, it allows to inspect the behavior of a specific loss mechanism, such as capacitor losses, radiation or coupling, on a more fundamental level than analyzing specific excitation modes only. Worst-case losses are identified in a straightforward manner, and a loss analysis of array Eigenmodes can correlate specific losses with regions of poor coil transmit- or receive sensitivity. As a result, components most detrimental to coil performance can be identified, allowing mitigating measures to be taken upon coil construction. Based on theoretical arguments, it was shown that coil coupling is closely related to occurring losses, and that resistive coupling compensation can not be achieved without incurring additional losses. Additionally, the plausibility of complex multi-channel electromagnetic simulations can be inferred by calculating the worst-case power imbalance, thus ensuring that further analysis is based on physically consistent data, which is of importance especially when safety decisions are based on simulations. Based on this wide range of applications, it can be concluded that the derived framework contributes to a better understanding of coil arrays in general, and could thus assist in designing and building more efficient and safe transmit coil arrays for MRI.

For the final point, the theoretical power balance considerations were incorporated into a comprehensive numerical of the twelve-channel transmit coil array to demonstrate their application. The coil is constructed of twelve current-sheet antennas arranged on the edges of an octahedron, with decoupling achieved via interconnecting capacitors. Electromagnetic analysis showed a low field impedance of the single elements, as desired for magnetic resonance applications. Decoupling was found to be significantly hampered by resistive coil interactions arising from loops formed through the decoupling capacitors. The resulting coupling losses were shown to be a major loss contributions in the subsequent loss analysis. The power balance formalism was extended to a receive noise analysis, allowing to construct receive noise source maps. Also, an Eigenmode analysis was used to associate regional sensitivity variations with their corresponding loss contributions. While central sensitivity was found to be almost 80 % of the theoretical maximum, this significantly dropped for peripheral regions, especially two spots in the anterior and posterior phantom regions. Losses for excitation and reception in these locations were found to be dominated by the tuning capacitor losses, which could be mitigated by using multiple parallel capacitances instead. It was found, that even though the array completely circumscribes the phantom, excitation and reception in the transversal xy slices performed superior compared to the other two orthogonal orientations. The power balance analysis of this coil as presented here, together with the two 7T head coils analyzed in the corresponding paper [43], serve as a reference for integrating the

methodology into a standard numerical coil analysis workflow in order to aid future coil array development.

Bibliography

- [1] Lauterbur PC. Image Formation by Induced Local Interactions: Examples Employing Nuclear Magnetic Resonance. *Nature* 1973;242:190–191.
- [2] Hoult D, Lauterbur PC. The sensitivity of the zeugmatographic experiment involving human samples. *J Magn Reson* 1979;34:425–433.
- [3] Edelstein Wa, Glover GH, Hardy CJ, Redington RW. The intrinsic signal-to-noise ratio in NMR imaging. *Magn Reson Med* 1986;3:604–618.
- [4] Hoult D, Richards R. The signal-to-noise ratio of the nuclear magnetic resonance experiment. *J Magn Reson* 1976;24:71–85.
- [5] Bottomley PA, Andrew ER. RF magnetic field penetration, phase shift and power dissipation in biological tissue: implications for NMR imaging. *Phys Med Biol* 1978;23:630–643.
- [6] Bydder G, Steiner R, Young I, Hall A, Thomas D, Marshall J, Pallis C, Legg N. Clinical NMR imaging of the brain: 140 cases. *Magn Reson Imaging* 1982; 1:183.
- [7] Ljunggren S. A simple graphical representation of fourier-based imaging methods. *J Magn Reson* 1983;54:338–343.
- [8] Twieg DB. The k-trajectory formulation of the NMR imaging process with applications in analysis and synthesis of imaging methods. *Med Phys* 1983; 10:610.
- [9] Hayes CE, Edelstein WA, Schenck JF, Mueller OM, Eash M. An efficient, highly homogeneous radiofrequency coil for whole-body NMR imaging at 1.5 T. *J Magn Reson* 1985;63:622–628.
- [10] Hoult DI. Sensitivity and power deposition in a high-field imaging experiment. *J Magn Reson Imaging* 2000;12:46–67.
- [11] Cao Z, Park J, Cho ZH, Collins CM. Numerical evaluation of image homogeneity, signal-to-noise ratio, and specific absorption rate for human brain imaging at 1.5, 3, 7, 10.5, and 14T in an 8-channel transmit/receive array. *J Magn Reson Imaging* 2015;41:1432–9.
- [12] Katscher U, Börnert P. Parallel RF transmission in MRI. *NMR Biomed* 2006; 19:393–400.
- [13] Padormo F, Beqiri A, Hajnal JV, Malik SJ. Parallel transmission for ultrahigh-field imaging. *NMR Biomed* 2015; doi: 10.1002/nbm.3313.

-
- [14] Roemer PB, Edelstein Wa, Hayes CE, Souza SP, Mueller OM. The NMR phased array. *Magn Reson Med* 1990;16:192–225.
- [15] Pruessmann KP, Weiger M, Scheidegger MB, Boesiger P. SENSE: sensitivity encoding for fast MRI. *Magn Reson Med* 1999;42:952–62.
- [16] Mao W, Smith MB, Collins CM. Exploring the limits of RF shimming for high-field MRI of the human head. *Magn Reson Med* 2006;56:918–22.
- [17] Orzada S, Maderwald S, Poser BA, Bitz AK, Quick HH, Ladd ME. RF excitation using time interleaved acquisition of modes (TIAMO) to address B1 inhomogeneity in high-field MRI. *Magn Reson Med* 2010;64:327–33.
- [18] Katscher U, Börnert P, Leussler C, van den Brink JS. Transmit SENSE. *Magn Reson Med* 2003;49:144–50.
- [19] Ullmann P, Junge S, Wick M, Seifert F, Ruhm W, Hennig J. Experimental analysis of parallel excitation using dedicated coil setups and simultaneous RF transmission on multiple channels. *Magn Reson Med* 2005;54:994–1001.
- [20] Homann H, Graesslin I, Eggers H, Nehrke K, Vernickel P, Katscher U, Dössel O, Börnert P. Local SAR management by RF Shimming: a simulation study with multiple human body models. *Magn Reson Mater Physics, Biol Med* 2012;25:193–204.
- [21] Lee J, Gebhardt M, Wald LL, Adalsteinsson E. Local SAR in parallel transmission pulse design. *Magn Reson Med* 2012;67:1566–78.
- [22] Zhu Y, Alon L, Deniz CM, Brown R, Sodickson DK. System and SAR characterization in parallel RF transmission. *Magn Reson Med* 2012;67:1367–78.
- [23] Adriany G, Van de Moortele PF, Wiesinger F, Moeller S, Strupp JP, Andersen P, Snyder C, Zhang X, Chen W, Pruessmann KP, Boesiger P, Vaughan T, Ugurbil K. Transmit and receive transmission line arrays for 7 Tesla parallel imaging. *Magn Reson Med* 2005;53:434–45.
- [24] Adriany G, Auerbach EJ, Snyder CJ, Gözübüyük A, Moeller S, Ritter J, Van de Moortele PF, Vaughan T, Ugurbil K. A 32-channel lattice transmission line array for parallel transmit and receive MRI at 7 tesla. *Magn Reson Med* 2010;63:1478–85.
- [25] Avdievich NI, Oh S, Hetherington HP, Collins CM. Improved homogeneity of the transmit field by simultaneous transmission with phased array and volume coil. *J Magn Reson Imaging* 2010;32:476–81.
- [26] Avdievich NI. Transceiver-Phased Arrays for Human Brain Studies at 7 T. *Appl Magn Reson* 2011;41:483–506.
- [27] Raaijmakers AJE, Ipek O, Klomp DWJ, Possanzini C, Harvey PR, Lagendijk JJW, van den Berg CAT. Design of a radiative surface coil array element at 7 T: the single-side adapted dipole antenna. *Magn Reson Med* 2011;66:1488–97.

- [28] Avdievich NI, Pan JW, Hetherington HP. Resonant inductive decoupling (RID) for transceiver arrays to compensate for both reactive and resistive components of the mutual impedance. *NMR Biomed* 2013;26:1547–54.
- [29] Shajan G, Kozlov M, Hoffmann J, Turner R, Scheffler K, Pohmann R. A 16-channel dual-row transmit array in combination with a 31-element receive array for human brain imaging at 9.4 T. *Magn Reson Med* 2014;71:870–879.
- [30] Gudino N, Heilman Ja, Riffe MJ, Heid O, Vester M, Griswold Ma. On-coil multiple channel transmit system based on class-D amplification and pre-amplification with current amplitude feedback. *Magn Reson Med* 2013;70:276–89.
- [31] Jesmanowicz A, Nencka A, Hyde JS. Direct radiofrequency phase control in MRI by digital waveform playback at the larmor frequency. *Magn Reson Med* 2014;71:846–852.
- [32] Eichfelder G, Gebhardt M. Local specific absorption rate control for parallel transmission by virtual observation points. *Magn Reson Med* 2011;66:1468–76.
- [33] Graesslin I, Homann H, Biederer S, Börnert P, Nehrke K, Vernickel P, Mens G, Harvey P, Katscher U. A specific absorption rate prediction concept for parallel transmission MR. *Magn Reson Med* 2012;68:1664–74.
- [34] Graesslin I, Vernickel P, Börnert P, Nehrke K, Mens G, Harvey P, Katscher U. Comprehensive RF safety concept for parallel transmission MR. *Magn Reson Med* 2015;74:589–598.
- [35] Webb aG, Van de Moortele PF. The technological future of 7 T MRI hardware. *NMR Biomed* 2015; doi: 10.1002/nbm.3315.
- [36] Childs AS, Malik SJ, O’Regan DP, Hajnal JV. Impact of number of channels on RF shimming at 3T. *Magn Reson Mater Physics, Biol Med* 2013;26:401–410.
- [37] Guérin B, Gebhardt M, Serano P, Adalsteinsson E, Hamm M, Pfeuffer J, Nistler J, Wald LL. Comparison of simulated parallel transmit body arrays at 3 T using excitation uniformity, global SAR, local SAR, and power efficiency metrics. *Magn Reson Med* 2015;73:1137–1150.
- [38] Kuehne A, Hoffmann W, Seifert F. A fully digital RF pulse generator designed for multiple transmission channels. In: *Proc. Intl. Soc. Mag. Reson. Med.* Honolulu, U.S.A.; 2009 3017.
- [39] Kuehne A, Waxmann P, Hoffmann W, Pfeiffer H, Seemann R, Seifert F, Ittermann B. Parallel transmission experiments using an extensible RF pulse generator. In: *Proc. Intl. Soc. Mag. Reson. Med.* Salt Lake City, U.S.A.; 2013 4404.
- [40] Kuehne A, Waxmann P, Hoffmann W, Pfeiffer H, Seemann R, Seifert F, Speck O, Ittermann B. It goes to 11: A scalable home-built transmit array beyond eight channels. In: *Proc. Intl. Soc. Mag. Reson. Med.* 2015 3147.

-
- [41] Kirilina E, Riemer T, W D, HE M, Seifert F. The novel 12 channel octahedral transmit / receive array for parallel imaging of human head at 3 T . In: Proc. Intl. Soc. Mag. Reson. Med. 2007 1035.
- [42] Kuehne A, Goluch S, Moser E, Laistler E. Power balance considerations for RF transmit coil arrays. In: Proc. Intl. Soc. Mag. Reson. Med. Milan, Italy; 2014 0551.
- [43] Kuehne A, Goluch S, Waxmann P, Seifert F, Ittermann B, Moser E, Laistler E. Power balance and loss mechanism analysis in RF transmit coil arrays. *Magn Reson Med* 2015;74:1165–1176.
- [44] Bloch F. Nuclear induction. *Phys Rev* 1946;70:460–474.
- [45] Purcell EM, Torrey HC, Pound RV. Resonance absorption by nuclear magnetic moments in a solid. *Phys Rev* 1946;69:37–38.
- [46] Hanson LG. Is quantum mechanics necessary for understanding magnetic resonance? *Concepts Magn Reson Part A* 2008;32A:329–340.
- [47] Hoult DI, Ginsberg NS. The quantum origins of the free induction decay signal and spin noise. *J Magn Reson* 2001;148:182–99.
- [48] Hoult D. The origins and present status of the radio wave controversy in NMR. *Concepts Magn Reson Part A* 2009;34A:193–216.
- [49] Hoult DI, Bhakar B. NMR signal reception: Virtual photons and coherent spontaneous emission. *Concepts Magn Reson* 1997;9:277–297.
- [50] Abragam A. *Principles of Nuclear Magnetism*. 1st edition. Clarendon Press; 1961.
- [51] Slichter CP. *Principles of Magnetic Resonance*. 3rd edition. Springer; 1990.
- [52] Brown RW, Cheng YCN, Haacke EM, Thompson MR, Venkatesan R, editors. *Magnetic Resonance Imaging*. Chichester, UK: John Wiley & Sons Ltd; 2014.
- [53] Chen CN, Hoult D. *Biomedical Magnetic Resonance Technology*. IOP Publishing; 1989.
- [54] Hoult D. The solution of the bloch equations in the presence of a varying B1 field - An approach to selective pulse analysis. *J Magn Reson* 1979;35:69–86.
- [55] Hoult DI. The principle of reciprocity in signal strength calculations - A mathematical guide. *Concepts Magn Reson* 2000;54:324–187.
- [56] Pohmann R, Scheffler K. A theoretical and experimental comparison of different techniques for B1 mapping at very high fields. *NMR Biomed* 2013; 26:265–75.
- [57] Rieke V, Butts Pauly K. MR thermometry. *J Magn Reson Imaging* 2008; 27:376–90.
- [58] Pauly J. A k-space analysis of small-tip-angle excitation. *J Magn Reson* 1969 1989;81:43–56.

- [59] Lupu M, Briguët A, Mispelter J. NMR Probeheads: For Biophysical and Biomedical Experiments. 1st edition. Imperial College; 2006.
- [60] Jin J. Electromagnetic Analysis and Design in Magnetic Resonance Imaging. 1st edition. CRC Press; 1999.
- [61] Wright SM, Magin RL, Kelton JR. Arrays of mutually coupled receiver coils: Theory and application. *Magn Reson Med* 1991;17:252–268.
- [62] Wright S. Receiver Loop Arrays. Chichester, UK: John Wiley & Sons, Ltd; 2007.
- [63] Lee RF, Giaquinto RO, Hardy CJ. Coupling and decoupling theory and its application to the MRI phased array. *Magn Reson Med* 2002;48:203–13.
- [64] Fujita H, Zheng T, Yang X, Finnerty MJ, Handa S. RF Surface Receive Array Coils: The Art of an LC Circuit. *J Magn Reson Imaging* 2013;38:12–25.
- [65] Keil B, Wald LL. Massively parallel MRI detector arrays. *J Magn Reson* 2013; 229:75–89.
- [66] Lee RF, Westgate CR, Weiss RG, Newman DC, Bottomley PA. Planar strip array (PSA) for MRI. *Magn Reson Med* 2001;45:673–83.
- [67] Lee RF, Hardy CJ, Sodickson DK, Bottomley Pa. Lumped-element planar strip array (LPSA) for parallel MRI. *Magn Reson Med* 2004;51:172–83.
- [68] Ohliger Ma, Greenman RL, Giaquinto R, McKenzie Ca, Wiggins G, Sodickson DK. Concentric coil arrays for parallel MRI. *Magn Reson Med* 2005;54:1248–60.
- [69] Alagappan V, Nistler J, Adalsteinsson E, Setsompop K, Fontius U, Zelinski A, Vester M, Wiggins GC, Hebrank F, Renz W, Schmitt F, Wald LL. Degenerate mode band-pass birdcage coil for accelerated parallel excitation. *Magn Reson Med* 2007;57:1148–58.
- [70] Hong SM, Park JH, Woo MK, Kim YB, Cho ZH. New design concept of monopole antenna array for UHF 7T MRI. *Magn Reson Med* 2014;71:1944–1952.
- [71] Li Y, Xie Z, Pang Y, Vigneron D, Zhang X. ICE decoupling technique for RF coil array designs. *Med Phys* 2011;38:4086.
- [72] Constantinides C, Angeli S. Elimination of mutual inductance in NMR phased arrays: The paddle design revisited. *J Magn Reson* 2012;222:59–67.
- [73] Brunner DO, De Zanche N, Fröhlich J, Paska J, Pruessmann KP. Travelling-wave nuclear magnetic resonance. *Nature* 2009;457:994–8.
- [74] Alderman DW, Grant DM. An efficient decoupler coil design which reduces heating in conductive samples in superconducting spectrometers. *J Magn Reson* 1979;36:447–451.

- [75] Hasgall P, Neufeld E, Gosselin M, Klingenböck A, Kuster N. IT'IS Database for thermal and electromagnetic parameters of biological tissues, Version 2.4, www.itis.ethz.ch/database.
- [76] Duensing GR, Brooker HR, Fitzsimmons JR. Maximizing signal-to-noise ratio in the presence of coil coupling. *J Magn Reson B* 1996;111:230–5.
- [77] Ohliger Ma, Ledden P, McKenzie Ca, Sodickson DK. Effects of inductive coupling on parallel MR image reconstructions. *Magn Reson Med* 2004;52:628–39.
- [78] Wu B, Qu P, Wang C, Yuan J, Shen GX. Interconnecting L/C components for decoupling and its application to low-field open MRI array. *Concepts Magn Reson Part B Magn Reson Eng* 2007;31B:116–126.
- [79] Davis WA. *Radio Frequency Circuit Design*. 2nd edition. John Wiley & Sons; 2011, 25–28 .
- [80] Collins CM, Wang Z. Calculation of radiofrequency electromagnetic fields and their effects in MRI of human subjects. *Magn Reson Med* 2011;65:1470–82.
- [81] Yee KS. Numerical solution of initial boundary value problems involving maxwell's equations in isotropic media. *IEEE Trans Antennas Propag* 1966; 14:302–307.
- [82] Taflove A, Hagness SC. *Computational Electrodynamics: The Finite-Difference Time-Domain Method*. 3rd edition. Artech House; 2005.
- [83] Kuehne A, Waiczies H, Rudolf E, Seifert F, Ittermann B. Reliable FDTD Convergence detection and acceleration. In: *Proc. Intl. Soc. Mag. Reson. Med. Melbourne, Australia; 2012* 4757.
- [84] Christ A, Kainz W, Hahn EG, Honegger K, Zefferer M, Neufeld E, Rascher W, Janka R, Bautz W, Chen J, Kiefer B, Schmitt P, Hollenbach HP, Shen J, Oberle M, Szczerba D, Kam A, Guag JW, Kuster N. The Virtual Family—development of surface-based anatomical models of two adults and two children for dosimetric simulations. *Phys Med Biol* 2010;55:N23–38.
- [85] Kozlov M, Turner R. Fast MRI coil analysis based on 3-D electromagnetic and RF circuit co-simulation. *J Magn Reson* 2009;200:147–52.
- [86] Lemdiasov RA, Obi AA, Ludwig R. A numerical postprocessing procedure for analyzing radio frequency MRI coils. *Concepts Magn Reson Part A* 2011; 38A:133–147.
- [87] Beqiri A, Hand JW, Hajnal JV, Malik SJ. Comparison between simulated decoupling regimes for specific absorption rate prediction in parallel transmit MRI. *Magn Reson Med* 2015;74:1423–1434.
- [88] Stollberger R, Wach P. Imaging of the active B1 field in vivo. *Magn Reson Med* 1996;35:246–51.

- [89] Goluch S, Kuehne A, Meyerspeer M, Kriegl R, Schmid AI, Fiedler GB, Herrmann T, Mallow J, Hong SM, Cho ZH, Bernarding J, Moser E, Laistler E. A form-fitted three channel 31 P, two channel 1 H transceiver coil array for calf muscle studies at 7 T. *Magn Reson Med* 2015;73:2376–2389.
- [90] Deniz CM, Brown R, Lattanzi R, Alon L, Sodickson DK, Zhu Y. Maximum efficiency radiofrequency shimming: Theory and initial application for hip imaging at 7 tesla. *Magn Reson Med* 2013;69:1379–88.
- [91] Carluccio G, Collins CM, Erricolo D. A fast, analytically based method to optimize local transmit efficiency for a transmit array. *Magn Reson Med* 2014;71:432–9.
- [92] Hoffmann J, Mirkes C, Shajan G, Scheffler K, Pohmann R. Combination of a multimode antenna and TIAMO for traveling-wave imaging at 9.4 Tesla. *Magn Reson Med* 2016;75:452–462.
- [93] Ullmann P. Parallele Sendetechniken in der Magnetresonanztomographie: Experimentelle Realisierung, Anwendungen und Perspektiven. Ph.D. thesis, 2007.
- [94] Zhu Y. Parallel excitation with an array of transmit coils. *Magn Reson Med* 2004;51:775–84.
- [95] Grissom W, Yip Cy, Zhang Z, Stenger VA, Fessler Ja, Noll DC. Spatial domain method for the design of RF pulses in multicoil parallel excitation. *Magn Reson Med* 2006;56:620–9.
- [96] Brunner DO, Pruessmann KP. Optimal design of multiple-channel RF pulses under strict power and SAR constraints. *Magn Reson Med* 2010;63:1280–91.
- [97] Sbrizzi A, Hoogduin H, Lagendijk JJ, Luijten P, Sleijpen GLG, van den Berg CaT. Time efficient design of multi dimensional RF pulses: application of a multi shift CGLS algorithm. *Magn Reson Med* 2011;66:879–85.
- [98] Sbrizzi A, Hoogduin H, Lagendijk JJ, Luijten P, Sleijpen GLG, van den Berg CAT. Fast design of local N-gram-specific absorption rate-optimized radiofrequency pulses for parallel transmit systems. *Magn Reson Med* 2012;67:824–34.
- [99] Yip CY, Fessler Ja, Noll DC. Iterative RF pulse design for multidimensional, small-tip-angle selective excitation. *Magn Reson Med* 2005;54:908–917.
- [100] Graessl A, Renz W, Hezel F, Dieringer Ma, Winter L, Oezerdem C, Rieger J, Kellman P, Santoro D, Lindel TD, Frauenrath T, Pfeiffer H, Niendorf T. Modular 32-channel transceiver coil array for cardiac MRI at 7.0T. *Magn Reson Med* 2014;72:276–90.
- [101] Kuehne A. Mehrkanal-Anregung in der Hochfeld-Magnetresonanztomografie: Realisierung mit stromgesteuerten HF-Spulen-Arrays. Technical report, 2008.
- [102] Hoult DI. Receiver Design for MR. In: eMagRes. Chichester, UK: John Wiley & Sons, Ltd; 1996 1–21.

-
- [103] Crawley aP, Wood ML, Henkelman RM. Elimination of transverse coherences in FLASH MRI. *Magn Reson Med* 1988;8:248–260.
- [104] Jehenson P, Westphal M, Schuff N. Analytical method for the compensation of eddy-current effects induced by pulsed magnetic field gradients in NMR systems. *J Magn Reson* 1990;90:264–278.
- [105] Jensen DJ, Brey WW, Delayre JL, Narayana Pa. Reduction of pulsed gradient settling time in the superconducting magnet of a magnetic resonance instrument. *Med Phys* 2011;14:859–862.
- [106] Nixon TW, McIntyre S, Rothman DL, de Graaf Ra. Compensation of gradient-induced magnetic field perturbations. *J Magn Reson* 2008;192:209–17.
- [107] Schneider E, Glover G. Rapid in vivo proton shimming. *Magn Reson Med* 1991;18:335–347.
- [108] Seifert F, Wübbeler G, Junge S, Ittermann B, Rinneberg H. Patient safety concept for multichannel transmit coils. *J Magn Reson Imaging* 2007;26:1315–21.
- [109] Chung S, Kim D, Breton E, Axel L. Rapid B1 + mapping using a preconditioning RF pulse with turboFLASH readout. *Magn Reson Med* 2010;64:439–446.
- [110] Kurpad KN, Wright SM, Boskamp EB. RF current element design for independent control of current amplitude and phase in transmit phased arrays. *Concepts Magn Reson Part B Magn Reson Eng* 2006;29B:75–83.
- [111] Kirilina E, Kühne A, Lindel T, Hoffmann W, Rhein KH, Riemer T, Seifert F. Current CONTrolled Transmit And Receive Coil Elements (CONTAR) for Parallel Acquisition and Parallel Excitation Techniques at High-Field MRI. *Appl Magn Reson* 2011;41:507–523.
- [112] Vernickel P, Röschmann P, Findeklee C, Lüdeke KM, Leussler C, Overweg J, Katscher U, Grässlin I, Schünemann K. Eight-channel transmit/receive body MRI coil at 3T. *Magn Reson Med* 2007;58:381–9.
- [113] Hoult DI, Kolansky G, Kripiakevich D, King SB. The NMR multi-transmit phased array: a Cartesian feedback approach. *J Magn Reson* 2004;171:64–70.
- [114] Zhang B, Sodickson DK, Lattanzi R, Duan Q, Stoeckel B, Wiggins GC. Whole body traveling wave magnetic resonance imaging at high field strength: homogeneity, efficiency, and energy deposition as compared with traditional excitation mechanisms. *Magn Reson Med* 2012;67:1183–93.
- [115] Liu W, Kao Cp, Collins CM, Smith MB, Yang QX. On consideration of radiated power in RF field simulations for MRI. *Magn Reson Med* 2013;69:290–4.
- [116] Haase A, Odoj F, Von Kienlin M, Warnking J, Fidler F, Weisser A, Nittka M, Rommel E, Lanz T, Kalusche B, Griswold M. NMR probeheads for in vivo applications. *Concepts Magn Reson* 2000;12:361–388.

- [117] Seifert F, Ittermann B. Uncertainties of local SAR determination in parallel transmission MRI. In: Proc. Intl. Soc. Mag. Reson. Med. Salt Lake City, Utah, USA; 2013 p. 2827.
- [118] Liao ZF, Kong-Liang H, Bai-Po Y, Yuan YF. A transmitting boundary for transient wave analyses. *Sci Sin A* 1984;27:1063–1076.
- [119] Berenger JP. A perfectly matched layer for the absorption of electromagnetic waves. *J Comput Phys* 1994;114:185–200.
- [120] Kozlov M, Turner R. Optimization of geometry for a dual-row MRI array at 400 MHz. In: 2013 IEEE MTT-S Int. Microw. Work. Ser. RF Wirel. Technol. Biomed. Healthc. Appl. Singapore; 2013 1–3.
- [121] Seifert F, Lindel T, Ullmann P. Efficient and comprehensive EM field simulation procedure for pTX experiments. In: Proc. Intl. Soc. Mag. Reson. Med. Melbourne, Victoria, Australia; 2012 2777.
- [122] Deniz CM, Alon L, Brown R, Sodickson DK, Zhu Y. Specific absorption rate benefits of including measured electric field interactions in parallel excitation pulse design. *Magn Reson Med* 2012;67:164–74.
- [123] Balanis CA. *Advanced Engineering Electromagnetics*. 2nd edition. John Wiley & Sons; 2012, 485 .
- [124] Bardati F, Borrani A, Gerardino A, Lovisolo Ga. SAR optimization in a phased array radiofrequency hyperthermia system. *IEEE Trans Biomed Eng* 1995;42:1201–7.
- [125] King SB, Varosi SM, Duensing GR. Eigenmode analysis for understanding phased array coils and their limits. *Concepts Magn Reson Part B Magn Reson Eng* 2006;29B:42–49.
- [126] King SB, Varosi SM, Duensing GR. Optimum SNR data compression in hardware using an Eigencoil array. *Magn Reson Med* 2010;63:1346–56.
- [127] De Moerloose J, De Zutter D. Poynting's theorem for the finite-difference-time-domain method. *Microw Opt Technol Lett* 1995;8:257–260.
- [128] Wedge S, Rutledge D. Noise waves and passive linear multiports. *IEEE Microw Guid Wave Lett* 1991;1:117–119.
- [129] Kuehne A, Laistler E, Henning A, Moser E, Avdievich NI. Analytical Performance Evaluation and Optimization of Resonant Inductive Decoupling (RID). In: Proc. Intl. Soc. Mag. Reson. Med. 2015 3183.
- [130] Junge S, Seifert F, Wuebbeler G, Rinneberg H. Current Sheet Antenna Array - a transmit / receive surface coil array for MRI at high fields. In: Proc. Intl. Soc. Mag. Reson. Med. 2004 41.
- [131] Rinneberg H, Seifert F, Junge S. Apparatus for the production of radio frequency B1 fields for NMR using current sheet antennas, Patent# 7,049,818, 2006.

-
- [132] Kuehne A, Waiczies H, Moser E, Laistler E. Skin effect estimation accuracy in FDTD coil simulations. In: Proc. Intl. Soc. Mag. Reson. Med. Milan, Italy; 2014 1363.
- [133] Giovannetti G, Hartwig V, Landini L, Santarelli MF. Classical and lateral skin effect contributions estimation in strip MR coils. *Concepts Magn Reson Part B Magn Reson Eng* 2012;41B:57–61.
- [134] Belevitch V. The lateral skin effect in a flat conductor. *Philips Tech Rev* 1973; 32:221–231.
- [135] Chamberlin K, Gordon L. Modeling good conductors using the finite-difference, time-domain technique. *IEEE Trans Electromagn Compat* 1995; 37:210–216.
- [136] Kumar A, Edelstein WA, Bottomley PA. Noise figure limits for circular loop MR coils. *Magn Reson Med* 2009;61:1201–9.
- [137] Kamon M, Ttsuk M, White J. FASTHENRY: a multipole-accelerated 3-D inductance extraction program. *IEEE Trans Microw Theory Tech* 1994;42:1750–1758.
- [138] Brown R, Wang Y, Spincemaille P, Lee RF. On the noise correlation matrix for multiple radio frequency coils. *Magn Reson Med* 2007;58:218–24.
- [139] Malzacher M, Vester M, Rehner R, Stumpf C, Korf P. SNR simulations including coupled preamplifier noise. In: Proc. Intl. Soc. Mag. Reson. Med. 2015 2157.
- [140] Vester M, Biber S, Rehner R, Wiggins G, Brown R, Sodickson D. Mitigation of inductive coupling in array coils by wideband port matching. In: Proc. Intl. Soc. Mag. Reson. Med. 2012 2690.
- [141] Breuer F, Blaimer M, Mueller M, Heidemann R, Griswold M, Jakob P. The use of principal component analysis (PCA) for estimation of the maximum reduction factor in 2D parallel imaging. In: Proc. Intl. Soc. Mag. Reson. Med., volume 13. 2005 2668.
- [142] Celuch-Marcysiak M. Extended study of Poynting theorem and reciprocity on nonuniform FDTD meshes. *IEE Proc - Sci Meas Technol* 2004;151:452–455.
- [143] Maunder A, Fallone BG, Daneshmand M, De Zanche N. Experimental verification of SNR and parallel imaging improvements using composite arrays. *NMR Biomed* 2015;28:141–153.
- [144] Zhang B, Sodickson DK, Duan Q, Wiggins G. Contribution of the inherent traveling wave in 7T to large FOV imaging. In: Proc. Intl. Soc. Mag. Reson. Med. Stockholm, Sweden; 2010 1480.

Acknowledgments

This thesis would not have been possible without the guidance, support and encouragement from many people.

First of all, I'd like to thank Dr. Bernd Ittermann for giving me the opportunity to pursue my PhD studies at the Physikalisch-Technische Bundesanstalt in Berlin. Our countless in-depth discussions on multi-coil interaction behavior, often ending in me admitting to be at my wit's end, inspired me to pursue the theoretical considerations of this thesis.

I am very thankful to Prof. Dr. Oliver Speck, head of the Department of Biomedical Magnetic Resonance at Otto-von-Guericke University in Magdeburg, for agreeing to be my supervisor at the OvGU and providing valuable insight and support especially in the final stages of my thesis.

I am also deeply grateful to Dr. Frank Seifert, who, with his inexhaustible pool of knowledge on everything concerning MRI, contributed a great deal to the knowledge I gained during my PTB years.

Furthermore, I am indebted to the engineering team at the PTB. Dr. Werner Hoffmann, Harald Pfeiffer and Reiner Seeman assisted me in all hardware questions, and large parts of this thesis wouldn't have been possible without their help.

Working together with Dr. Helmar Waiczies proved to build the basis for a very enjoyable and productive working relationship, and I am glad that our paths crossed again working at MRI.Tools.

I would like to acknowledge both Tomasz Lindel and Patrick Waxmann, who significantly helped my understanding of parallel transmission techniques. They also supplied their software for pulse calculation, for which I am very thankful. Without their accumulated knowledge on how to tame the beast that was the transmit array, I would have given up in frustration after encountering the umpteenth system bug or lockup.

Special thanks go out to Frank Wojcik, who always found ways to motivate me with kind words and his bottomless cookie jar, that helped nurture me through many unplanned late-night sessions.

Many thanks also go out to Dr. Rüdiger Brühl, who helped me a lot regarding any programming-related questions.

I would again like to thank everyone in the 8.1 group at the PTB for making my time there as great as it was, both on a personal and professional level.

On the Viennese side, my thanks firstly go out to Prof. Dr. Ewald Moser who offered me a position without having completed my dissertation. Working in his highly diverse group proved to be a very rewarding challenge that immensely helped my understanding of MRI coil related concepts. I am hence very grateful to everyone in the group, especially Dr. Elmar Laistler, Dr. Sigrun Goluch, Dr. Roberta Kriegl, Dr. Martin Meyerspeer and Dr. Ingo Schmid for many discussions, interesting questions and after-work pub visits.

A very special thank you goes out to Dr. Ariane Fillmer for her constant encouragement and support, proof-reading, valuable suggestions, conference steak dates and many fondly remembered late night ghost-busting sessions during my final measurement times in Berlin.

Finally, I am very thankful towards my parents and sister, who always supported and encouraged me throughout the course of my studies.

André Kühne

Curriculum Vitae

Achillesstraße 30
13125 Berlin, Germany
☎ +49 176 41 82 30 30
✉ andre.kuehne@gmail.com

Persönliche Daten

Geburtsdatum- und Ort 4. August 1981 in Greifswald
Nationalität deutsch

Praxiserfahrungen

06/2015–heute **Chief Science Officer, Hochfrequenzingenieur, MRI.TOOLS GmbH,**
Berlin, Deutschland.
Entwicklung von MR Hochfrequenzspulen für die Human- und Tierbildgebung

Wissenschaftlicher Werdegang

- 06/2012–05/2015 **Wiss. Mitarbeiter, MR Center of Excellence, Medizinische Universität Wien,**
Wien, Österreich.
Projekt: “Research Studio Austria für Ultrahochfeld MR-Anwendungen”
Kernaufgaben:
- Konzeption und Entwicklung von “SimOpTx”, einem Softwarepaket zur schnellen SAR-Evaluation von Mehrkanalsendespulen
 - Entwicklung einer schnellen und zuverlässigen Simulationsinfrastruktur für Hochfrequenzspulen
 - Hochfrequenzspulenenwicklung für simultane TMS und fMRT-Experimente
 - Hochfrequenzspulenenwicklung für multinukleare Anwendungen
 - Betreuung von Doktoranden
- 10/2008–05/2012 **Wiss. Mitarbeiter, Physikalisch-Technische Bundesanstalt, Berlin.**
Projekt: “Entwicklung und Implementation von Messverfahren zur SAR-Bestimmung an Probenköpfen für die Hochfeld-MRT”, in Kooperation mit Rapid Biomedical
Kernaufgaben:
- SAR analyse neuer MR-Spulendesigns, geometrische Optimierung unter SAR-Beschränkungen
 - Kalibration und Validierung von Simulationen durch Messungen
 - Entwicklung von elektromagnetischen Feldsensoren
- 10/2008–heute **Doktorand, Physikalisch-Technische Bundesanstalt, Berlin.**
“Parallel transmission in MRI: Electromagnetic considerations and advances in signal chain hardware”
Forschungsschwerpunkte:
- Entwicklung und Anwendung einer mehrkanaligen Hochfrequenzsendekette für die Hochfeld-MRT
 - Leistungsbilanzanalysen für mehrkanalige Sendespulen

Ausbildung

- 10/2001–10/2008 **Diplom Physik**, *Ernst-Moritz-Arndt Universität*, Greifswald.
Schwerpunkt: Medizinische Physik
Diplomarbeitsthema: "Mehrkanal-Anregung in der Hochfeld-Magnetresonanz-Tomografie: Realisierung mit stromgesteuerten HF-Spulen-Arrays", angefertigt an der Physikalisch-Technischen Bundesanstalt, Berlin
- 09/2004–05/2005 **Auslandsstudium**, *University of Saskatchewan*, Saskatoon, Kanada.
- 09/1988–07/2000 **Abitur**, *Johann-Gottfried-Herder-Gymnasium*, Greifswald.

Weitere Erfahrungen

Eingeladene Vorträge

- 06/2015 Thema: RF Spulensicherheit, ESMRMB workshop on coil building, Berlin
- 06/2014 Thema: RF Spulensicherheit, ESMRMB workshop on coil building, Berlin
- 06/2013 Thema: RF Spulensicherheit, ESMRMB workshop on coil building, Berlin

Diverse

- 2002–2007 Nachhilfelehrer für Studenten und Schüler in den Fächern Mathematik und Physik
- 10/2006–05/2007 Wiss. Mitarbeiter an der Klinik für Strahlentherapie und Radioonkologie, Greifswald
- 06/2005–09/2005 Praktikum am Institut für Diagnostische Radiologie und Neuroradiologie, Greifswald
- 09/2000–07/2001 Zivildienst, Intensivstation, Universitätsklinikum Greifswald

Professionelle Kenntnisse

- Elektromagnetische Simulationen Anwendung von CST Microwave Studio, Remcom XFDTD, Speag SEMCAD, Agilent ADS
- Numerik MATLAB (Bildanalyse, algorithmische Optimierung, paralleles Rechnen), Python, Mathematica
- Hochfrequenztechnik Benutzung von Vektornetzwerkanalysatoren und Oszilloskopen, Löten, Microcontrollerprogrammierung (Arduino)
- MRT Breites Grundlagenwissen über allgemeine Magnetresonanzkonzepte
Erfahrung mit Siemens und Bruker MRT Hard- und Software
Teilnahme an einem Siemens IDEA-Programmierkurs

Sprachen

- Deutsch Muttersprache
- Englisch fließend
- Französisch Grundkenntnisse

Publikationen

Artikel in Fachzeitschriften

- 2016 1. Waxmann P, Mekle R, Schubert F, Brühl R, Kuehne A, Lindel TD, Seifert F, Speck O, Ittermann B. *A new sequence for shaped voxel spectroscopy in the human brain using 2D spatially selective excitation and parallel transmission* **NMR in Biomed.** 2016; DOI: 10.1002/nbm.3558
- 2015 2. Kuehne A, Goluch S, Waxmann P, Seifert F, Ittermann B, Moser E, Laistler E. *Power Balance and Loss Mechanism Analysis in RF Transmit Coil Arrays* **Magn. Reson. Med.** 2015; 74:1165-76, DOI: 10.1002/mrm.25493
3. Goluch S, Kuehne A, Meyerspeer M, Kriegl R, Schmid AI, Fiedler GB, Herrmann T, Mallow J, Hong SM, Cho ZH, Bernarding J, Moser E, Laistler E. *A form-fitted three channel 31P, two channel 1H transceiver coil array for calf muscle studies at 7 T.* **Magn. Reson. Med.** 2015; 73:2376-2389; DOI: 10.1002/mrm.25339
4. Kriegl R, Ginefri J-C, Poirier-Quinot M, Darrasse L, Goluch S, Kuehne A, Moser E, Laistler E. *Novel inductive decoupling technique for flexible transceiver arrays of monolithic transmission line resonators.* **Magn. Reson. Med.** 2015; 73:1669-1681 DOI: 10.1002/mrm.25260
5. Navarro de Lara LI, Windischberger C, Kuehne A, Sieg J, Bestmann S, Weiskopf N, Strasser B, Moser E, Laistler E. *A novel coil array for combined TMS/fMRI experiments at 3 T.* **Magn. Reson. Med.** 2015; 74:1492-1501, DOI:10.1002/mrm.25535
6. Meyerspeer M, Magill AW, Kuehne A, Gruetter R, Moser E, Schmid AI *Simultaneous and interleaved acquisition of NMR signals from different nuclei with a clinical MRI scanner.* **Magn. Reson. Med.** 2015; DOI: 10.1002/mrm.26056
7. Oezerdem C, Winter L, Graessl A, Paul K, Els A, Weinberger O, Rieger J, Kuehne A, Dieringer M, Hezel F, Voit D, Frahm J, Niendorf T *16-channel bow tie antenna transceiver array for cardiac MR at 7.0 tesla.* **Magn. Reson. Med.** 2015; DOI: 10.1002/mrm.25840
- Vorjahre 8. Waiczies H, Lepore S, Drechsler S, Qadri F, Purfürst B, Sydow K, Dathe M, Kuehne A, Lindel T, Hoffmann W, Pohlmann A, Niendorf T, Waiczies S. *Visualizing brain inflammation with a shingled-leg radio-frequency head probe for 19F/1H MRI.* **Sci. Rep.** 2013;3:1280. DOI: 10.1038/srep01280.
9. Kirilina E, Kuehne A, Lindel T, Hoffmann W, Rhein KH, Riemer T, Seifert F. *Current CONtrolled Transmit And Receive Coil Elements (CONTAR) for Parallel Acquisition and Parallel Excitation Techniques at High-Field MRI.* **Appl. Magn. Reson.** 2011;41:507-523. DOI: 10.1007/s00723-011-0248-y.

Konferenzbeiträge

Vorträge

- 2014 10. Kuehne A, Goluch S, Moser E, Laistler E. *Power balance considerations for RF transmit coil arrays*. In: Proceedings of the **ISMRM**. Milan, Italy; 2014.
- Vorjahre 11. Kuehne A, Seifert F, Ittermann B. *Behaviour of B1+ and SAR under model scaling for the "Virtual Family"*. In: Proceedings of the **ESMRMB**, Lisbon, Portugal; 2012
12. Kuehne A, Seifert F, Ittermann B. *Disagreement of local RF power deposition and SAR in FDTD simulations*. In: Proceedings of the **ESMRMB**, Leipzig, Germany; 2011

Poster

- 2015 13. Kuehne A, Laistler E., Henning A. Moser E., Avdievich NI. *Analytical Performance Evaluation and Optimization of Resonant Inductive Decoupling (RID)*. In: Proceedings of the **ISMRM**. Toronto, Canada; 2015. p. 3183.
14. Kuehne A, Waxmann P., Hoffmann W., Pfeiffer H., Seemann R., Seifert F., Speck, O., Ittermann, B. *It goes to 11: A scalable home-built transmit array beyond eight channels* In: Proceedings of the **ISMRM**. Toronto, Canada; 2015. p. 3147.
15. Goluch S., Kuehne A, Moser E., Laistler E. *A 3 channel ³¹P and 2 channel ¹H coil array for ³¹P NMR in the visual cortex at 7 T* In: Proceedings of the **ISMRM**. Toronto, Canada; 2015. p. 3147.

- 2014
16. Kuehne A, Waiczies H, Moser E, Laistler E. *Skin effect estimation accuracy in FDTD coil simulations*. In: Proceedings of the **ISMRM**. Milan, Italy; 2014. p. 1363.
 17. Kuehne A, Goluch S, Moser E, Laistler E. *Comprehensive analysis of parallel transmission local SAR errors introduced by an assumed uniform density distribution*. In: Proceedings of the **ISMRM**. Milan, Italy; 2014. p. 1380.
 18. Navarro de Lara L, Windischberger C, Sieg J, Moser E, Laistler E, Kuehne A. *Investigating interactions between a TMS system and a novel MR device for concurrent TMS/fMRI experiments*. In: Proceedings of the **ISMRM**. Milan, Italy; 2014. p. 4520.
 19. Goluch S, Kuehne A., Moser E, Laistler E. *Performance Comparison of a Form Fitted Coil Array Vs. a Quadrature Birdcage Coil for ^{31}P MRS Studies in the Human Calf at 7T*. In: Proceedings of the **ISMRM**. Milan, Italy; 2014. p. 1326.
 20. Laistler E, Kuehne A., Goluch S, Dymerska B, Sieg J, Moser E. *Micro-Imaging of Finger Tendons In Vivo Using a Dedicated Solenoidal Finger Coil at 7T*. In: Proceedings of the **ISMRM**. Milan, Italy; 2014. p. 1193.
 21. Kraus O, Winter L, Dieringer M, Graessl A, Rieger J, Oezerdem C, Hezel F, Kuehne A, Waxmann P, Pfeiffer H, Niendorf T. *Local Coil Versus Conventional Body Coil Transmission for Cardiac MR: B1+ Efficiency Improvements and Enhanced Blood Myocardium Contrast for 2D CINE SSFP Imaging at 3T*. In: Proceedings of the **ISMRM**. Milan, Italy; 2014. p. 2364.
 22. Nagy Z, Oliver-Taylor A, Kuehne A, Weiskopf N. *Transmitted Power from a Tx/Rx Birdcage Coil to Nearby Conductors in Air and in Gel*. In: Proceedings of the **ISMRM**. Milan, Italy; 2014. p. 1371.
- 2013
23. Kuehne A, Moser E, Laistler E, *Influence of coil damage on local SAR for an 8-channel head coil at 300 MHz*. In: Proceedings of the **ESMRMB**. Toulouse, France; 2013.
 24. Kuehne A, Moser E, Laistler E. *Numerical optimization of a 3-channel array coil for ^{31}P functional spectroscopy at 7T*. In: Proceedings of the **ISMRM**. Salt Lake City, U.S.A.; 2013. p. 5119.
 25. Kuehne A, Waxmann P, Hoffmann W, Pfeiffer H, Seemann R, Seifert F, Ittermann B. *Parallel transmission experiments using an extensible RF pulse generator*. In: Proceedings of the **ISMRM**. Salt Lake City, U.S.A.; 2013. p. 4404.
 26. Goluch S, Kuehne A, Moser E, Laistler E. *Comparison of Decoupling Schemes for a Three Channel ^{31}P Array for the Human Calf Muscle at 7 T Using 3D Electromagnetic Simulation*. In: Proceedings of the **ISMRM**. Salt Lake City, U.S.A.; 2013. p. 2786.
 27. Laistler E, Goluch S, Kuehne A, Meyerspeer M, Schmid AI, Sieg J, Herrmann T, Mallow J, Bernarding J, Moser E *A Form-Fitted 3 Channel ^{31}P , Two Channel ^1H Transceive Coil for Calf Muscle Studies at 7 T*. In: Proceedings of the **ISMRM**. Salt Lake City, U.S.A.; 2013. p. 2786.

- 2012 28. Kuehne A, Seifert F, Ittermann B. *GPU-accelerated SAR computation with arbitrary averaging shapes*. In: Proceedings of the **ISMRM**. Melbourne, Australia; 2012. p. 4260.
29. Kuehne A, Waiczies H, Rudolf E, Seifert F, Ittermann B. *Reliable FDTD Convergence detection and acceleration*. In: Proceedings of the **ISMRM**. Melbourne, Australia; 2012. p. 4757.
30. Lindel TD, Kuehne A, Waxmann P, Seifert F, Niendorf T, Ittermann B. *Homogeneity Compensation for RF Refocusing Pulses in Spatially Selective Excitation (SSE) at 7T* In: Proceedings of the **ISMRM**. Melbourne, Australia; 2012. p. 2216.
31. Lindel TD, Kuehne A, Waxmann P, Seifert F, Niendorf T, Ittermann B. *Spatially Selective Excitation (SSE) for Brain Imaging at 7 T* In: Proceedings of the **ISMRM**. Melbourne, Australia; 2012. p. 1061.
- Vorjahre 32. Kuehne A, Waiczies H, Raghuraman S, Wichmann T, Lanz T, Seifert F, Ittermann B. *A Comparison of FDTD-Solvers for Simulation of a 31 P Birdcage Coil at 1.5 T*. In: Proceedings of the **ISMRM**. Montreal, Canada; 2011. p. 3865.
33. Kuehne A, Hoffmann W, Seifert F. *A fully digital RF pulse generator designed for multiple transmission channels*. In: Proceedings of the **ISMRM**. Honolulu, U.S.A.; 2009. p. 3017.

André Kühne
Achillesstraße 30
13125 Berlin

Erklärung

Hiermit erkläre ich, dass die von mir eingereichte Dissertation zu dem Thema

„Parallel Transmission in MRI: Electromagnetic Considerations and Advances in Signal Chain Hardware“

selbständig verfasst, nicht schon als Dissertation verwendet habe und die benutzten Hilfsmittel und Quellen vollständig angegeben wurden.

Weiterhin erkläre ich, dass ich weder diese noch eine andere Arbeit zur Erlangung des akademischen Grades doctor rerum naturalium (Dr. rer. nat.) an anderen Einrichtungen eingereicht habe.

Magdeburg,